Detection, Imaging and Characterisation of Fog Fields by Radar

Li, Yunlong

DOI
10.4233/uuid:126c4b76-235e-411b-b5ed-c513b4d59dad

Publication date
2016

Document Version
Final published version

Citation (APA)
Li, Y. (2016). *Detection, Imaging and Characterisation of Fog Fields by Radar*. [Dissertation (TU Delft), Delft University of Technology]. https://doi.org/10.4233/uuid:126c4b76-235e-411b-b5ed-c513b4d59dad

Detection, Imaging and Characterisation of Fog Fields by Radar

Yunlong LI

Detection, Imaging and Characterisation of Fog Fields by Radar

Proefschrift

ter verkrijging van de graad van doctor
aan de Technische Universiteit Delft,
op gezag van de Rector Magnificus prof. ir. K.C.A.M. Luyben,
voorzitter van het College voor Promoties,
in het openbaar te verdedigen op woensdag 14 November 2016 om 10:00 uur

door

Yunlong LI

Master of Engineering in Information and Communication Engineering,
National University of Defense Technology
geboren te Xingtai, Hebei, China.

This dissertation has been approved by the

promotors: Prof. ir. P. Hoogeboom and Prof. dr. ir. H.W.J. Russchenberg

Composition of the doctoral committee:

Rector Magnificus	chairman
Prof. ir. P. Hoogeboom	Delft University of Technology
Prof .dr. ir. H.W.J. Russchenberg	Delft University of Technology

Independent members:

Prof. dr. ir. A.P. Siebesma	Delft University of Technology
Prof. dr .ir. F. Le Chevalier	Delft University of Technology
Prof. dr .ir. A.M.J. van Eijk	Universiteit Nantes, France
Prof. dr. T. Jin	National University of Defense Technology, China
Dr. M. Haeffelin	Ecole Polytechnique, France

Yunglong LI
Detection, Imaging and Characterisation of Fog Fields by Radar

Department of Geoscience and Remote Sensing
Delft University of Technology

Keywords: Fog, Radar, Detection, Visibility estimator, Dual-wavelength technique

ISBN 978-94-028-0406-5

Type set by the author with the LaTeX Documentation System
Printed by IPSKAMP Printing, The Netherlands

An electronic version of this dissertation is available at
http://repository.tudelft.nl/.

To my parents

Contents

List of Figures

List of Tables

Acknowledgement

After so many days and nights working on my thesis, finally comes the time to write this acknowledgment. This thesis would not have been accomplished without the help and support from many people and I would like to express my gratitude to all of them.

First and foremost, I would like to express my gratitude to my daily supervisor, Prof. ir. Peter Hoogeboom, for providing his guidance during my four years of PhD study. He is always patient to answer all my questions in my research work and inspires me to think up more ideas. More importantly, he teaches me the way to be a good researcher, which I think would be very helpful in my future career. What impressed me most is that he once told me that I should not directly use any results from others without sufficient evidence. All in all, I could not have completed my thesis without his support.

I am also grateful to my promoter, Prof. dr. ir. Herman Russchenburg for giving me the chance to commence my PhD study in the ATMOS group. He is a man of great wisdom and broad outlook. After every talk with him, I have a feeling of released from a long-time struggle in my research work. He inspires me to seize every opportunity to communicate with others and absorb the essence and reject the dross. His inspiring suggestions and encouragement provide me the motivation to complete my thesis.

I shall extend my thanks to Henk Klein Baltink and Reinout Boers from KNMI. Thank you for discussing my research topic with me and providing numerous valuable data for me. I would not have fulfilled this work without these data. Many thanks go to Henk for always answering my questions in patience. I would also thank the Energy Research Center of the Netherlands (ECN) for providing the FSSP data. Moreover, I would like to thank Matthias Bauer-Pfundstein from METEK in Germany for providing his valuable data for me.

My great thanks also go to the ATMOS group, which makes me feel as warm as home. Thank you, Christine. Every time I asked you any questions, you stopped your work at hand and answered them for me. Thank you, Yann. I still remember your encouraging look during my first presentation and your confirmation afterwards. I really feel the warmth and passion of the French from you. Thank you, my younger brother Jiapeng. I appreciate your useful suggestions when I was stucked into tangled questions. I still remember every evening when we were working in the big PhD room. I would also thank my colleagues, Igor, Karolina Sarna, Ricardo, Lukas, Albert, Julien. I enjoyed every talk with you and you will be an unforgettable memory for me. I would also give my thanks to Tim Vlemmix, for helping me with the translation work.

I wish to thank China Scholarship Council (CSC) and ATMOS group for providing me with the financial support for my PhD study.

The four years of my life in the Netherlands would not be so colorful without the company of friends. I would like to say thank you to all my Chinese friends I met here. I really miss those moments that we had a drink and shared our complains of life. I hope one day we can still talk about the life together. I cannot list all your names here but I do remember all of you. Qiang, Xi, Xinchao, Yuan, Xialu, Yu, Jian, Xiang, Yue, Shilong,

Jianbing, Ling, Hua, Zhaochuan, Haidong, Yazhou, Jinhu, Jiangjun, Ye, Long, Yunlong, Zhengyu, Yuxuan. Thank you for your appearance in my life. Special thanks go to my best friend Chao. Thank you for your company and encouragement all the way so that I can overcome all the difficulties in these four years. Thank you for polishing my thesis using your precious time. Besides, I must thank Wei for the design of cover page.

Last but not least, I would like to express my gratitude to my parents for their unconditional support and encouragement in countless days and nights. I hope this thesis can be the best present for you.

Yunlong LI
Delft, May 2016

Summary

As a significant phenomenon in meteorology, fog has attracted more and more concern from the scientific community, because of its impacts on visibility in air- and road-transportation. E.g., at airports, the frequency of aircrafts taking off and landing has to be reduced during heavy fogs, because in conditions of low visibility the pilots need to have more space between the aircrafts during landing and taxying. In this context, many approaches have been proposed to detect fog with various types of instruments. Among the active remote sensing instruments, radars are well suited for continuous fog observations, and they can satisfy the need for high spatial resolution and sensitivity. Compared to traditional centimeter-wave radars, millimeter-wave radars are more sensitive to minute fog droplets, whereas the gaseous attenuation from oxygen and water vapor is still very small. The trade-off is that the attenuation from fog droplets at millimeter waves is much larger than at centimeter waves. In this thesis, we study the observation of fog with millimeter-wave radars and investigate the feasibility of developing an advanced fog-visibility radar.

The scattering and extinction properties of fog form the basis for fog-related issues. The dominant backscattering and absorption are related to the characteristic parameters of fog, reflectivity Z, visibility Vis, and attenuation L_a. In **chapter 2**, the backscattering and absorption characteristics of fog are investigated over a large range of radar frequencies, temperatures, and droplet sizes. Mie and Rayleigh scattering regimes are also compared in the study of the backscattering and absorption characteristics of fog. Fog DSD (drop size distribution) is a significant intermediate variable to connect all the characteristics parameters of fog, because Z, Vis, and L_a are related to the 6th, 2nd, and 3rd moments of DSD.

In this work, fog observation data are provided by the Cabauw Experimental Site for Atmospheric Research (CESAR), which is a large, internationally operated, meteorological and remote sensing site with a unique set of sensors, covering nearly every important aspect of atmospheric processes. On this site we have been able to acquire simultaneous datasets of DSD, optical visibility at various heights, temperatures and winds at various heights, millimeter-wave radar reflections as a function of height. The instruments in use are described in **chapter 3**. It is the first time that complete fog cycles (onset and dissipation) have been systematically measured in the Netherlands. Meanwhile, it is also the first time that a millimeter-wave radar has been operated for fog measurements in a so-called "fog mode".

Our longer term aim is remote visibility estimation by radar(s) in fog. This is a new and challenging area, for which we see important applications in transport, e.g. airports, major roads. To achieve this, in **chapter 4** we compare various visibility estimator models. In the end, in **chapter 5** we develop a new visibility estimator model $Vis = f(Z, L_a)$ where Vis can be deduced from radar signal only, i.e. reflectivity Z and attenuation L_a. Our new model $Vis = f(Z, L_a)$ results in a higher accuracy of Vis estimates than the other Vis estimator models, when tested on a large group of simulated DSD datasets.

The robust performance of the model is also tested with simultaneous Vis, Z, and DSD measurements from the previously described instruments at CESAR.

Based on our new model $Vis = f(Z, L_a)$, in **chapter 6** we investigate the feasibility of developing an advanced fog-visibility radar. The operational parameters of the radar are determined with a large group of simulated Z and L_a datasets at a range of frequencies in a scope of Vis levels. The datasets have covered various fog types and evolutionary stages of fog. Moreover, dual-wavelength technique is introduced to provide Vis estimates from Z measurements. In this technique, the Z measurement errors, the temperature errors, and the presence of Mie scattering drizzle and ice particles would lead to errors in the L_a estimates which then propagate to errors in the Vis estimates based on the model $Vis = f(Z, L_a)$. Therefore, an error analysis on Vis estimates in terms of the model $Vis = f(Z, L_a)$ is made in order to determine the optimum radar frequency pair for fog measurements.

Samenvatting

Mist is een belangrijk meteorologisch verschijnsel dat steeds meer aandacht krijgt van wetenschappers vanwege de invloed op zicht in de luchtvaart en het wegverkeer. Op luchthavens bijvoorbeeld, wordt de frequentie van vertrek en aankomst van vliegtuigen verlaagd wanneer er dichte mist is. Onder zulke omstandigheden is het noodzakelijk om de afstand tussen vliegtuigen die landen of taxiën te vergroten.

In deze context zijn vele methoden voorgesteld voor de detectie van mist met uiteenlopende instrumenten. Binnen de categorie van instrumenten voor actieve remote sensing zijn radars zeer geschikt voor continue observatie van mist en ze bieden hoge ruimtelijke resolutie en gevoeligheid. Vergeleken met traditionele radars die opereren bij een golflengte van centimeters, zijn de systemen die opereren bij een millimeter golflengte meer gevoelig voor kleine mistdruppels, terwijl de signaalafzwakking door gassen als zuurstof en waterdamp nog altijd klein is. De afweging die moet worden gemaakt komt voort uit het feit dat de afzwakking door mistdruppels voor millimetergolven aanzienlijk groter is dan voor centimetergolven. In dit proefschrift bestuderen we de detectie van mist met behulp van radars opererend op millimeter golflengtes en onderzoeken we de haalbaarheid van het ontwikkelen van een geavanceerde mist-zicht-radar.

De verstrooings en extinctie eigenschappen van mist vormen de basis van mistgerelateerde problematiek. De dominante terugwaardse verstrooing en absorptie zijn gerelateerd aan de karakteristieke parameters van mist, reflectiviteit Z, zicht Vis en afzwakking L_a. In **hoodstuk 2** worden de terugwaardse verstrooings- en absorptie-eigenschappen van mist onderzocht voor een groot domein van radar frequenties, temperaturen en druppelgroottes. Ook worden Mie en Rayleigh verstrooingsregimes vergeleken in de studie naar de terugwaardse verstooings- en absorptie-eigenschappen van mist. DSD (druppelgrootte verdeling) van mist is een belangrijke tussentijdse variabele die alle karakteristieke parameters van mist verbindt omdat Z, Vis, en L_a gerelateerd zijn aan de 6^e, 2^e en 3^e momenten van DSD.

In dit werk worden mistobservaties geleverd door de Cabauw Experimental Site for Atmospheric Research (CESAR), een groot, internationaal opererend samenwerkingsverband voor meteorologie en remote sensing met een unieke verzameling sensoren voor met detecteren van vrijwel ieder belangrijk aspect van atmosferische processen. Op deze locatie hebben we gelijktijdige datasets kunnen verkrijgen van DSD, optisch zicht op verschillende hoogtes, temperatuur en wind op verschillende hoogtes, millimeter golflengte radarreflecties als funtie van de hoogte. De gebruikte instrumenten zijn beschreven in **hoofdstuk 3**. Voor het eerst is in Nederland een complete mistcyclus (ontstaan en oplossen) systematisch gemeten. Bovendien is het de eerste keer dat een millimeter golflengte radar voor mistmetingen is ingezet in de zogenaamde "mistmodus".

Onze langetermijndoelstelling is het met behulp van radar(s) kunnen schatten van zicht bij mist. Dit is een nieuw en uitdagend terrein waarvoor we belangrijke toepassingen zien in het transport, zoals op luchthavens en hoofdwegen. Om dit te berei-

ken, vergelijken we in **hoofdstuk 4** verschillende modellen om zicht te schatten. Uiteindelijk ontwikkelen we in **hoofstuk 5** een nieuw model voor het schatten van mist $Vis = f(Z, L_a)$ waar Vis kan worden afgeleid van alleen het radarsignaal, met andere woorden van de reflectiviteit Z en afzwakking L_a. One nieuwe model $Vis = f(Z, L_a)$ levert een hogere nauwkeurigheid van Vis schattingen dan andere modellen bij toepassing op een grote groep van gesimuleerde DSD datasets. De robuustheid van het model is eveneens getest met simultane Vis, Z, en DSD metingen van de eerder beschreven instrumenten op CESAR.

In **hoofdstuk 6** onderzoeken we de haalbaaheid van het ontwikkelen van een geavanceerde mist-zicht radar gebaseerd op ons nieuwe model $Vis = f(Z, L_a)$. De operationele parameters van de radar zijn bepaald met een grote groep gesimuleerde Z en L_a datasets voor een domein van frequenties in een bereik van Vis niveaus. De datasets omvatten uiteenlopende misttypes en ontwikkelingsfases van mist. Bovendien is een duale-golflengtetechniek geintroduceerd om L_a schattingen te leveren op basis van Z metingen. Hierbij leiden de meetfouten in Z, de fouten in temperatuur en de aanwezigheid van Mie-verstrooiende miezer- en ijsdeeltjes tot fouten in L_a schattingen die vervolgens resulteren in fouten in de Vis schattingen op basis van het model $Vis = f(Z, L_a)$. Om die redden is een foutenschatting gemaakt voor Vis schattingen in termen van het model $Vis = f(Z, L_a)$ zodat het optimale radarfrequentiepaar voor mist metingen kon worden bepaald.

Nomenclature

List of acronyms

AFGL	Air Force Geophysics Laboratory
AWS	Automatic Weather Station
BSRN	Baseline Surface Radiation Network
CESAR	Cabauw Experimental Site for Atmospheric Research
CWR	Centimeter-Wave radar
DSD	Drop Size Distribution
DWR	Dual-wavelength Ratio
FFT	Fast Fourier Tranform
FMCW	Frequency Modulated Continuous Wave
FRAM	Fog Remote Sensing and Modeling
FSSP	Forward Scattering Spectrometer Probe
IDRA	IRCTR Drizzle Radar
IRCTR	International Research Centre for Telecommunications and Radar
iPort	innnovative airPort
IWV	Integrated Water Vapor
KNMI	Royal Netherlands Meteorological Institute
LiDAR	Light Detection And Ranging
LWC	Liquid Water Content
LWP	Liquid Water Path
MWR	Millimeter-Wave radar
NWP	Numerical Weather Forecast
OPC	Optical Particle Counter
PMS-CSAS	Particle Measurement Systems-Classical Scattering Aerosol Spectrometer
RACE	Radiation and Aerosol Cloud Experiment
Radar	Radio Detection And Ranging
RMSE	Root Mean Squared Root
R-Square	Ratio of SSR and SST
RTC	Radiative Transfer Calculations
RVR	Runway Visual Range
SIRTA	Site Instrumental de Recherche par Télédétection Atmosphérique
SMPS	Scanning Mobility Particle Sizer
SNR	Signal to Noise Ratio
SSE	Sum of Squares due to Error
SSR	Sum of Squares of Regression
SST	Total Sum of Squares
WTF	Weather Test Facility

List of symbols

cm	centimeter
dB	decibel
dBZ	decible of reflectivity
dB/km	decibel per kilometer
km	kilometer
m	meter
mm	millimeter
μm	micrometer
$^\circ$	degree
°C	degree centigrade

D	droplet diameter
r	droplet radius
T	temperature
f	frequency
λ	wavelength
P_t	transmit power
P_r	received power
P_n	noise power of radar
G_t	transmit antenna gain
G_r	received antenna gain
V	range resolution volume
θ	azimuth beamwidth
ϕ	elevation beamwidth
ΔR	range resolution
c	speed of light
R	distance/ rainfall rate
τ	pulse width
B	bandwidth
NF	noise figure
N_{coh}	number of coherent averages
$N_{non-coh}$	number of non-coherent averages
$\beta_e xt$	extinction coefficient
R_{max}	maximum detection range of radar
σ	radar cross section
σ_a	absorption cross section
σ_b	backscattering cross section
σ_e	extinction cross section
σ_s	scattering cross section
Q_a	absorption efficiency
Q_b	backscattering efficiency
Q_e	extinction efficiency
Q_s	scattering efficiency

ε	complex permittivity
ε'	real part of complex permittivity
ε''	imaginary part of complex permittivity
m	complex refractive index
x	size parameter
K	parameter related to complex refractive index
n	refractive index
κ	absorption coefficient
ρ_w	density of water
N	total number concentration
r_m	mean radius
r_e	effective radius
σ	standard deviation of radius about mean radius
$n(D), n(r)$	drop size distribution
$\Gamma(\upsilon)$	Gamma function
υ	shape parameter of Gamma function
R_n	scale parameter of Gamma function
ϵ	threshold of contrast with human eyes in defining visibility
Vis	visibility
Z	radar reflectivity factor
η	volumetric reflectivity
k_a	attenuation coefficient
k_B	Boltzman's constant
l_a	dimensionless attenuation factor
L_a	attenuation factor of fog droplets
L_g	attenuation factor of gases
l_s	dimensionless radar system loss
L_s	radar system loss in dB
ΔDWR	errors in dual-wavelength ratio
ΔZ	errors in reflectivity measurements
ΔLWC	errors in LWC estimates
ΔL_a	errors in L_a estimates
ΔVis	errors in Vis estimates
$W(Vis)$	weight function describing the degree of importance of various Vis levels at highways c

1
Introduction

1.1. Motivation

In recent years, great efforts have been put into fog detection by various types of instruments, in order to reduce the losses caused by fog (Gultepe et al., 2007). With the development of radar technology, millimeter-wave radars have been developed for fog observations. However nowadays, the widely-used millimeter-waves radars are lack of sensitivity to fog due to the small sizes of fog droplets. Based on the fog observations from existing millimeter-wave radar systems, we investigate the feasibility of designing an advanced fog radar which can reach a high sensitivity to fog in a relatively long distance.

Furthermore, the fog radar is required to provide visibility information. To this end, we develop a visibility estimator model whereby all available information from radar signals only, i.e. reflectivity and attenuation can be used to deduce visibility.

1.2. Research background

Nowadays, fog and its related questions have attracted more and more concern by the society, because of its effects on the daily life of human beings. The worst one is the reduced visibility caused by fog. According to statistics, in Canada the total economic loss associated with the impact of reduced visibility on public transportation can be as large as that of storms, or even hurricanes (Gultepe et al., 2009). Because of the highly variability of fog in time and space scales, it is difficult to accurately forecast/nowcast fog, which is still a big obstacle for weather forecasters. Meanwhile, fog is a complex process which involves the interactions among microphysics, chemistry, thermodynamics, radiative cooling, turbulence and surface conditions (Roach et al., 1976; Brown and Roach, 1976). Therefore, fog has always been the concern of meteorologists and physical scientist. Furthermore, fog is always mixed with other polluting particles released by industries and biofuels to form smog, which is harmful to human's health. Biologists and environmentalists are devoted to investigating the causes of smog and reducing its occurrence, especially in industrial cities (Wilkins et al., 1954; Pandis et al., 1990).

Among all the effects associated with fog, the most notable one is the restricted visibility in land transportation, marine operations and low-level aviation. Particularly at airports, the frequency of aircrafts taking off and landing has to be reduced during heavy fogs, because in conditions of low visibility the pilots need to have more space between the aircrafts during landing and taxying. The standard instrumentation for fog detection at airports used to decide about the landing frequency are runway visual range (RVR) instruments installed at 2 m above the runway and ceilometers (Hazen et al., 2002; Werner

et al., 2005). Both types of instruments are not able to provide information about the vertical distribution of fog. The RVRs only provide information at 2-m level and the ceilometers hardly work at all during the fog. Due to this limited information about the spatial distribution of fog, the maximum frequency of landings decided by the airport meteorologists (flight category) often does not agree to the visibility experienced by the pilots, which causes too low through put or dangerous landings. A better knowledge of the spatial distribution of fog may also help to make a short term prediction of fog which would be very helpful for reducing the flying loops while waiting for the allowance for landing.

Active remote sensing instruments provide great potential of fog detection. Many approaches for ground fog detection using weather satellite data have been proposed Stephens et al. (2002); Bendix et al. (2005); Ingmann et al. (2006); Cermak and Bendix (2011). Moreover, the satellite data are often integrated with fog models and surface observations to retrieve fog micro- and macro-physical properties (Wright and Thomas, 1998; Ellrod, 2002; Hutchison et al., 2006; Gultepe and Milbrandt, 2007; Paul Herzegh, 2006; Cermak et al., 2006; Ellrod and Gultepe, 2007). However, the satellite observations can only provide the information of fog horizontal coverage. There is large uncertainty in this detection technique due to the lack of information on the vertical structures of fog layers (Schreiner et al., 1993). It is also difficult to discriminate between ground fog and elevated fog, though several theoretical schemes have been proposed (Bendix, 1995; Cermak, 2006). Another option is to utilize optical remote sensing instruments such as lidar, ceilometer etc. These instruments can function properly when visible extinction is not very large. The problem is that the optical signals cannot penetrate through heavy fogs due to the large attenuation (Collis, 1966; Nowak et al., 2008). In this context, radars are well suited for continuous fog observations, and they can satisfy the need for high spatial resolution and sensitivity (Battan, 1973). Compared to traditional centimeter-wave radars, millimeter-wave radars are more sensitive to minute fog droplets (Kollias et al., 2007), whereas the gaseous attenuation from oxygen and water vapor is still very small (Liebe, 1985, 1989). However, the attenuation from fog droplets at millimeter waves is much larger than at centimeter waves. The trade-off is that the large attenuation from fog droplets would, to some extent, offsets the advantage of millimeter-wave radars in acquiring high sensitivity to fog droplets (Platt, 1970; Mead et al., 1989; Li et al., 2014b).

Centimeter-wave radars are often used to observe rain and storms. For instance, the 3-cm-wavelength IDRA drizzle radar, which is designed by TU Delft and is now mounted on top of the CESAR (Cabauw Experimental Site for Atmospheric Research, the Netherlands) tower, aims for the detailed observation of the spatial and temporal distribution of rainfall and drizzle (Ventura, 2009). The WSR-88D Doppler radar, in use with the U.S. National Weather Service, is principally used for storm warnings (Heiss et al., 1990). Meanwhile, many millimeter-wave radars have been developed for cloud observations and research. The use of 35 GHz radars for cloud observations started in 1980s (Hobbs et al., 1985; Pasqualucci, 1984; Pasqualucci et al., 1983; Kropfli et al., 1995). These radars with Doppler and polarization capabilities were used to investigate cloud microphysical properties and cloud dynamics. Then it was followed by the use of 94 and 95 GHz radars in cloud studies (Lhermitte, 1987; Pazmany et al., 1994; Clothiaux et al., 1995; Babb et al., 1999; Meywerk et al., 2002). Radar sensitivity to thin clouds was improved by the use of higher frequency radars. The dual-wavelength (3 cm and 8 mm, 8 mm and 3 mm) radar

measurements were used to better retrieve the microphysics in rain and clouds (Eccles and Mueller, 1971; NAKAMURA and INOMATA, 1992; Gosset and Sauvageot, 1992; Sekelsky and McIntosh, 1996; Vivekanandan et al., 1999a). Moreover, radars were combined with in situ sensors dedicated to acquire more information about the rain and clouds (Frisch et al., 1995; Meneghini et al., 1997; Frisch and Feingold, 1998; Frisch et al., 2000; Löhnert et al., 2001; Krasnov and Russchenberg, 2002; Nash et al., 2005; O'Connor et al., 2005). More recently, millimeter-wave radars have been used in fog observations. A 1.4 mm wavelength incoherent radar has been developed for remote sensing of fog. Preliminary reflectivity measurements of fog were obtained at ranges between 36 and 1900 m, and these were the first measurements made at such a 1.4 mm wavelength (Mead et al., 1989). A scanning Ka-band cloud radar (MIRA-36) was operated at Munich airport for fog measurements during the fog season 2011/2012 in the frame of iPort project (Rohn et al., 2010). The ParisFog field campaign launched at SIRTA observatory (20 km South of Paris, France) documented an ensemble of radiative and dynamic processes in fog with a suite of state-of-the-art active and passive remote sensing instruments (Elias et al., 2009; Haeffelin et al., 2010; Burnet et al., 2012; Dupont et al., 2012; Hammer et al., 2014). A 95 GHz FMCW cloud radar was also used in the campaign for fog observations. The implementation of FMCW technology is now an efficient and reliable solution thanks to its high performance and drastic cost reduction. Moreover, a 95 GHz cloud profiling FMCW Doppler radar named FALCON-I was designed by Chiba University and was used to observe thin clouds at high altitudes (Takano et al., 2008; Toshiaki et al., 2012). This radar has a high sensitivity of -32 dBZ at 5 km distance and a high resolution of Doppler measurements. Because of its high performance, it is expected to observe fog with this radar. Furthermore, a fog field campaign was also lanched at CESAR during the fog season (October 1, 2011 - March 31, 2012). A 35 GHz cloud radar at CESAR has been used in a so-called "fog mode" for the first time in the campaign (Boers et al., 2013; Li et al., 2014a).

Visibility (Vis) is a significant parameter to describe the fog intensity. Many approaches have been used to determine Vis from simultaneously observed microphysical parameters. Derived from an ample set of data, an inverse proportionality between Vis and liquid water content (LWC) in fog was proposed, and the proportionality coefficients assumed different values for various fog types and evolutionary stages of fog (Eldridge, 1971; Tomasi and Tampieri, 1976; Chylek, 1978). Vis is also a function of droplet number concentration N (Meyer et al., 1980; Gultepe et al., 2006b). It was found that Vis and N pertain to the power-law relation, and the coefficients differ for various fogs. A new Vis parameterization scheme in a forecast model suggested that including LWC and N simultaneously could improve Vis estimates up to 50% (Gultepe et al., 2006a,b). Moreover, radar reflectivity (Z) of return echoes from fog can also describe the fog intensity. Based on the measured drop size distributions (DSD), various power-law relations were found between Z and LWC because of the various shapes of droplet spectra (Atlas, 1954; Sauvageot and Omar, 1987; Fox and Illingworth, 1997; Khain et al., 2008). The $Z - LWC$ relations in natural fogs were also simulated with Radiative Transfer Calculations assuming a prognostic modified Gamma-shaped DSD (Maier et al., 2012).

Although Vis and Z are often used to represent the fog intensity, they were hardly linked to each other in literature. To determine Vis from Z measurements was first men-

tioned in 1953 where Vis and Z were linked in terms of the median volume diameter and two coefficients which are nearly independent of the variations in droplet spectra (Atlas and Bartnoff, 1953). Later, an empirical relationship was proposed between Vis and Z based on the measured DSD data from the FRAM project (Gultepe et al., 2006b). Boers et al. (2013) proposed modeled $Vis-Z$ relations in a radiation fog layer whereby the evolution of fog layer was modeled with a droplet activation model which used aerosol size distributions as input, and Vis, Z were calculated from the modeled DSD using Mie scattering theory. However, there is still uncertainty of the number of aerosols that can be activated into fog droplets, and there is no explicit relationship describing the activation process. In the iPort project, an empirical $Vis-Z$ relation was also found from the fog measurements at Munich airport by a scanning Ka-band cloud radar and optical sensors, and a method was developed to determine Vis from the radar and ceilometer data (Bauer-Pfunstein et al., 2013).

Attenuation is an important parameter to describe the amount of energy that is lost in fog. In general, the attenuation is equivalent to the extinction, which is the sum of scattering and absorption by fog droplets. Attenuation factor (L_a: dB/km) is often used to describe the attenuated reflectivity per range of kilometer. The attenuation factor L_a of rain is found to be related to the rainfall rate R by power-law for a wide range of rainfall rates and rain types (Waldteufel, 1973; Atlas and Ulbrich, 1974, 1977). At wavelengths near 1 cm, the L_a-R relations are nearly linear and are relatively independent of the DSD (Doviak and Zrnic, 2014). Therefore, the attenuation factor L_a of rain can be deduced from the rainfall rate R measured with rain gauges along the propagation path. In addition, various empirical power-law $Z-R$ relations have been found from actual DSD measurements (Austin, 1987; Chandrasekar and Bringi, 1987; Rosenfeld et al., 1993; Vieux and Bedient, 1998). By combing the local L_a-R and $Z-R$ relations, various L_a-Z relations can be derived. In this way, the attenuation factor L_a of rain can be deduced from the Z measurements from radars based on the L_a-Z relations. Many L_a calculation models of clouds and fogs have been proposed in literature (Platt, 1970; Chen, 1975; Falcone Jr et al., 1979; Stewart and Essenwanger, 1982; Altshuler, 1984; Liebe et al., 1989; Zhao and Wu, 2000; Mao et al., 2004; Recommendation, 2009; Awan et al., 2009). However, there were rarely L_a-Z relations with fog. Assuming a homogeneous fog layer, L_a can be calculated by comparing the reflectivity from the same object with a known RCS at two different ranges along the propagation path in fog. More recently, L_a was supposed to be retrieved by the dual-wavelength or multi-wavelength technique. Since the attenuation of centimeter-wavelength radars in fog is very small which can often be neglected, we can compare the reflectivity from fog of centimeter-wavelength radars and millimeter-wavelength radars to compute the attenuation (Eccles and Mueller, 1971; Vivekanandan et al., 1999b; Perez and Zawadski, 2003; Ellis and Vivekanandan, 2010, 2011). Since reflectivity is measured with a limited accuracy, it is expected that the total attenuation should be larger than the accuracy of reflectivity measurements (Eccles and Mueller, 1971). Besides, the antenna beamwidths would need to match between the centimeter-wavelength radars and the millimeter-wavelength radars to minimize errors, meaning that the centimeter-wavelength antennas would need to be excessively large. Alternatively, L_a was proposed to be deduced from LWC based on the linear relation between them in Rayleigh scattering regime, and LWC was retrieved from the differential

attenuation between two millimeter-wave radars (e.g. Ka- and W-band) (Hogan et al., 2005). The likely errors in the LWC retrieval come from the reflectivity measurement errors, the temperature errors, the Mie scattering drizzle droplets, and the presence of ice particles (Hogan et al., 2005).

1.3. Research hypothesis

As mentioned above, Vis and Z are the key characteristic parameters to describe the fog intensity. It is common sense that heavy fogs have low Vis values and high Z values, and light fogs are just the opposite. Therefore, it is hypothesized that inverse $Vis-Z$ relations with fog can be established so that Vis can be deduced from Z measurements. Referring to the $Vis-LWC$, $Vis-N$, $Z-LWC$ relations, various power-law $Vis-Z$ relations can also be found from actual DSD measurements, and the coefficients differ with the various shapes of droplet spectra. Referring to the simulated $Z-LWC$ relations in natural fogs with Radiative Transfer Calculations, $Vis-Z$ relations can also be simulated based on an assumed Gamma-shaped DSD. The Gamma-based $Vis-Z$ relation is dependent on the shape and scale parameters of Gamma distribution in natural fogs. Boers et al. (2013) modeled the $Vis-Z$ relations in a radiation fog layer using a droplet activation model where the fog DSD was calculated as a function of aerosol spectra measured with a SMPS (Scanning Mobility Particle Sizer). Based on the modeled $Vis-Z$ relations, the radar backscatter signals from the radiation fog were converted to visibility. Figure 1.1 illustrates an example of the time-height cross section of Vis converted from Z measurements by means of the modeled $Vis-Z$ relations for a radiation fog event at CESAR on March 23, 2011.

Based on the $Vis-Z$ relations, we can investigate the feasibility of developing a novel radar-based visibility estimator that can be used in traffic management.

Furthermore, it has been found that the accuracy of Vis estimates can be improved up to 50% while adding N into the $Vis-LWC$ relations (Gultepe et al., 2006b). Therefore, it is hypothesized that the accuracy of Vis estimates from Z measurements could also be improved by adding other basic integrated quantities such as N, LWC into the $Vis-Z$ relations. This hypothesis has to be tested on a large group of fog DSD datasets. On one hand, the DSD datasets can be simulated from the parameter sets of an assumed Gamma-shaped fog DSD in literature. On the other hand, we have the fog DSD measured with a FSSP (Forward Scattering Spectrometer Probe) at CESAR during a comprehensive fog observation campaign in the season November 2011 - March 2012. Moreover, this hypothesis has to be tested on actual Vis and Z measurements, which were measured with in situ visibility sensors and a 35 GHz cloud radar at CESAR.

During the fog campaign at CESAR, a 35 GHz cloud radar was operated in a so-called "fog mode" to measure the fog. The "fog mode" is similar to the horizontal mode, where the radar beam is fixed and pointing horizontally in a given direction. In this mode, the radar beam can adequately propagate in the fog and probe the fog in detail. Our model/observation study has shown that the cloud radar at CESAR has the highest sensitivity of -55 dBZ during the onset of fog. Normally, the range of fog reflectivity is between -60 - -25 dBZ. Therefore, starting with the analysis of observation data from the cloud radar at CESAR, we can investigate the feasibility of designing an advanced fog radar which can reach a high sensitivity to fog in a relatively long distance.

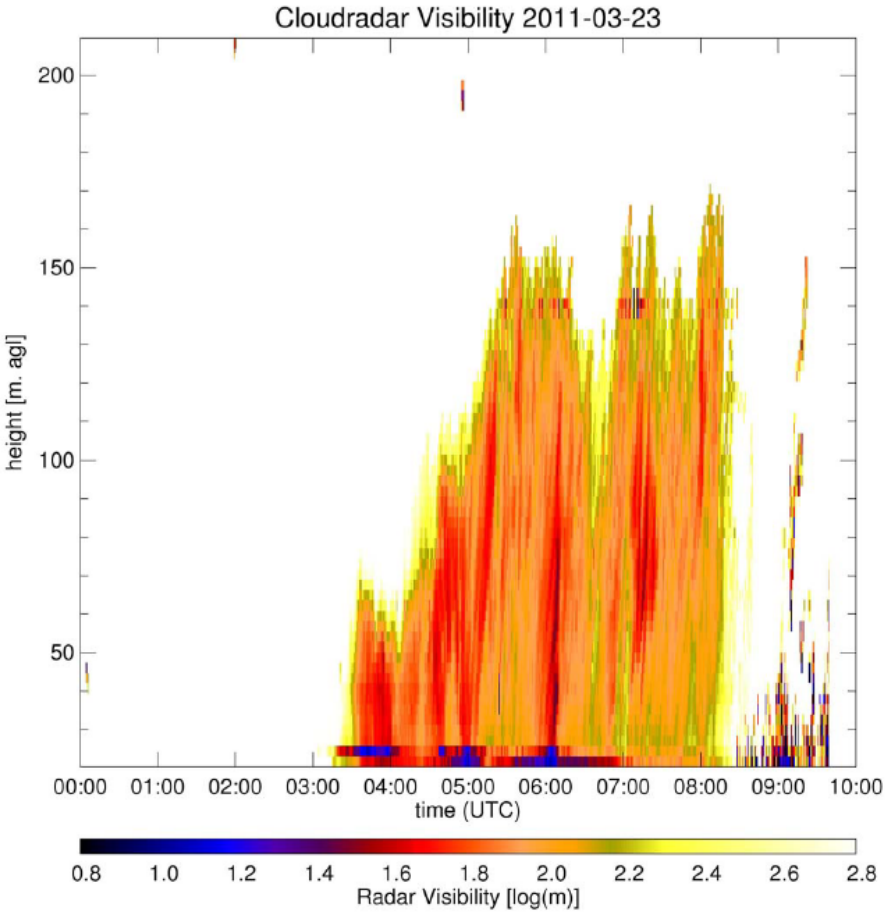

Figure 1.1: Time-height cross section of Vis converted from Z measurements by means of the modeled $Vis-Z$ relations for a radiation fog event at CESAR on March 23, 2011.

1.4. Research questions and methods

In this work, our longer term aim is to develop an advanced fog-visibility radar for reliable remote visibility estimation. This is a new and challenging area, for which we see important applications in transport, e.g. at airports, major roads. The main challenge question is:

How to remotely estimate visibility by radar(s) in fog and how to develop a fog radar that can achieve higher accuracy of visibility estimates?

To address the main issue, several specific research questions have to be considered.

1. How to determine an optimum radar frequency for fog measurements?

   Millimeter-wave radars are superior to centimeter-wave radars because the radar backscatter signals from fog increase with increasing frequency f. However, the

radar extinction signals from fog also increase with increasing frequency f. This means that it is not always advantageous to use very high frequencies to do fog measurements. We have to deal with the trade-off between the radar backscatter and extinction signals from fog with different frequencies.

To address this question, we can investigate the backscatter and extinction properties of fog over a large range of frequencies between 1 GHz - 1 THz, temperatures and fog droplet sizes by means of Mie and Rayleigh scattering calculation. The effects of frequency, temperature, and droplet size on the radar backscatter and extinction signals can be examined. Millimeter-wave radars at very high frequencies such as 140 GHz, 220 GHz should also be considered, though they are more costly and technically more complicated to be realized.

2. How to estimate Vis from Z measurements with higher accuracy?

   We aim to estimate Vis from Z measurements by means of the $Vis-Z$ relation. However, it is difficult to derive a universal relation between Vis and Z because both variables are the functions of droplet spectra, and various fog types and evolutionary stages of fog pertain to different shapes of droplet spectra. Normally, we derive the empirical $Vis-Z$ relations in two ways. One is to use the fog DSD data. In our work, the fog DSD was either simulated from the parameter sets of an assumed Gamma-shaped fog DSD in literature, or measured with a FSSP at CESAR. Both Vis and Z can be calculated from the DSD using Mie scattering theory. The other is to use the direct Vis and Z measurement data. In our work, Vis was measured with the in situ visibility sensors (e.g. Biral SWS-100 sensors) and Z was measured with a 35 GHz cloud radar at CESAR.

   In order to improve the accuracy of Vis estimates further, we can include other DSD-based quantities in the $Vis-Z$ relation. LWC is a key parameter which can be linked to either Vis or Z . To reduce the number of instruments in use, we can replace LWC with the attenuation measurements L_a of radar. The attenuation is related to the 3rd moment of DSD and is proportional to LWC at a given radar frequency (Chylek, 1978). The $Vis-Z-L_a$ relation can be compared with the $Vis-Z$ relation, where Vis, Z, and L_a are all calculated from the DSD. Of course a more realistic approach is to test the $Vis-Z-L_a$ relation with the measurement data from the in situ visibility sensors and the cloud radar at CESAR. Unfortunately we do not have as many radar measurements (which were invoked manually) as we have DSD and Vis measurements, which are continuous, automatic measurements. Furthermore, we currently lack reliable L_a measurements in our datasets, which we can only substitute by DSD-derived values.

3. How to develop an advanced fog-visibility radar?

   We can start with the performance analysis of the 35 GHz cloud radar at CESAR, though the radar was operated in the "fog mode" for only a couple of days and not many radar measurements were obtained. Given the operational parameters of the radar in the "fog mode", the sensitivity calculation can be done. In order to detect fog, the minimum received power from fog by the radar should be higher than the noise power of the radar. The maximum detection range of the radar in

fog can be determined at a threshold of SNR (Signal to Noise Ratio) is equal to 0 dB. In order to improve the sensitivity of the radar further, what we can think is to increase the radar frequency, transmit power, and pulse width. The effects of these factors on the sensitivity of the radar can be examined.

Furthermore, FMCW (Frequency Modulated Continuous Wave) technology can be an efficient and reliable solution to reduce the transmit power (Williams, 2000). However, the transmitter has to be well isolated with the receiver for the FMCW radar systems, in order to prevent the transmit signals leaking into the receiver signal processor. There are always two separate antennas which are used for transmit and receive for the FMCW radar systems (Tamatsu and Kumon, 2005). The transmit power of FMCW radar systems can be compared with that of pulse-Doppler radars while maintaining the other performance parameters are the same. Alternatively, we could use the pulse compression with a solid-state transmitter, especially at long ranges (Farnett and Stevens, 1990). For example, we can use short pulses between ranges 0 - 1 km, and use long pulses between ranges 1 - 3 km with the pulse compression technology, which helps to achieve high range resolution at long ranges. However, more transmit power is required while using the pulse compression technology.

With the specific fog-visibility radar, all available information from radar signals only, i.e. reflectivity and attenuation can be converted to visibility by means of the $Vis - Z - L_a$ relation. L_a cannot be simply retrieved from the radar measurements. Several methods can be adopted to retrieve L_a by radar(s). In case we use a single-frequency radar, L_a can be calculated by comparing the reflectivity from the same object with a known RCS at two different ranges along the propagation path in fog. Alternatively, L_a can be retrieved by the dual-wavelength technique. We can use either an non-attenuated wavelength combined with an attenuated wavelength, e.g. centimeter wavelength and millimeter wavelength, or two attenuated wavelengths. Considering the restriction on the antenna sizes, we are more inclined to use two millimeter wavelengths. As the attenuation is proportional to the LWC in fog at a given radar wavelength, we can first retrieve the LWC from the differential attenuation between the two millimeter wavelengths, and then derive the attenuation from the LWC. In this technique, the reflectivity measurement errors, the temperature errors, and the presence of Mie scattering drizzle droplets and ice particles can lead to errors in the LWC retrieval. The errors in the LWC will propagate to errors in the L_a estimates, which then propagate to errors in the Vis estimates based on the $Vis - Z - L_a$ relation. An error analysis on the Vis estimates has to be done in order to determine the optimum radar frequency pair for fog measurements. We can calculate the errors in the Vis estimates for various radar frequency pairs, and the optimum radar frequency pair will achieve the least errors. This step is very important and instructive for the design of an advanced fog-visibility radar with the dual-wavelength technology.

1.5. Research limitations

The robust performance of the $Vis-Z-L_a$ relation cannot be only validated with the DSD data, but be also validated with the measurement data from the in situ visibility sensors and the 35 GHz cloud radar at CESAR. The radar was operated in the "fog mode" for only a couple of days and we do not have as many radar measurements as we have DSD and Vis measurements. We can only use the limited radar measurements in the $Vis-Z-L_a$ relation. Furthermore, we also lack reliable L_a measurements in our datasets, which we can only substitute by DSD-derived values.

In our datasets, the fog DSD was either simulated from the parameter sets of an assumed Gamma-shaped fog DSD in literature, or measured with a FSSP at CESAR. No matter the simulated DSD or the actually measured DSD, neither of them provided the fog droplet spectra at different heights. In fact, the fog DSD varies greatly with height. Therefore, the DSD-derived $Vis-Z-L_a$ relations can only represent the status of the fog at the height of measured DSD.

During the onset of fog, most aerosols suspended in the air can be activated into fog droplets, leaving few dry and wet aerosols mixed with the fog droplets (Neiburger and Wurtele, 1949; Bott, 1991; Yuskiewicz et al., 1998). The non-activated aerosols may also contribute to the visibility reduction (White and Roberts, 1977; Diederen et al., 1985; Cheng and Tsai, 2000), but they cannot be detected by the FSSP due to their smaller sizes. At CESAR, a SMPS (Scanning Mobility Particle Sizer) was installed to measure the aerosol spectra in a range of 0.0025 - 1 μm in diameter. This consumption can be tested with the SMPS measurements.

1.6. Outline of the thesis

This chapter briefly reviewed the background of our work, and addressed the research questions and methods. The main challenge question in our work was divided into three specific research questions. The outline of this thesis is illustrated in Figure 1.2.

Chapter 2 gives an overview of fog, defining fog on the visibility and introducing four commonly occurring fog types and their dominant mechanisms. As the basis for exploring fog-related questions, the scattering and extinction properties of fog are investigated over a large range of frequency, temperature and droplet sizes. The effects of these factors on the fog properties are examined. Radar reflectivity, visibility, and attenuation factor are correlated to the radar backscattering and absorption of fog. These key parameters of fog are defined and formulated in Rayleigh scattering regime.

Chapter 3 introduces the fog measurement site in the Netherlands. A comprehensive fog observation campaign was carried out at CESAR during the fog season November 2011 - March 2012, and a great many in situ and remote sensing instruments were actively used in the fog measurements, including a 35 GHz cloud radar operated in a so-called "fog mode". The "fog mode" is described in detail. Based on the operational parameters of the radar in the "fog mode", the sensitivity calculation is done, in order to test the detection capability of the radar in fog conditions.

Chapter 4 sums up various empirical Vis and Z parameterizations in terms of the liquid water content LWC, droplet number concentration N, mean radius r_m, effective radius r_e or their combinations. To test the accuracy of the Vis and Z parameterizations,

the parameterized Vis, Z are compared with the DSD-derived Vis, Z and the measured Vis, Z with the in situ visibility sensors and the 35 GHz cloud radar. Various $Vis-Z$ and $Vis-Z-N$ relations are derived by combing the various Vis and Z parameterizations. The derived $Vis-Z$ and $Vis-Z-N$ relations are also compared with the Vis, Z measurements. Furthermore, we derive a Gamma-based $Vis-Z$ relation based on an assumed Gamma-shaped DSD and an exponential $Vis-Z$ relation using the regression analysis to the Vis, Z measurement data.

Chapter 5 proposes a new visibility estimator model $Vis = f(Z, L_a)$, where Vis can be deduced from radar signals only, e.g. reflectivity Z and attenuation L_a. Considering that both Vis and Z can be parameterized in terms of LWC, and LWC is proportional to L_a at a given radar frequency, an exponential $Vis-Z-L_a$ model $Vis = C \cdot L_a^a \cdot Z^b$ is derived by including the L_a in the exponential model $Vis = a \cdot Z^b$. The exponential $Vis-Z-L_a$ model is compared with the Gamma-based $Vis-Z$ model and the exponential $Vis-Z$ model in the aspect of achieving high accuracy of Vis estimates. Three types of datasets are used to validate the robust performance of the exponential $Vis-Z-L_a$ model. First it is tested on a large group of simulated DSD datasets for various fog types and evolutionary stages of fog. Next, the exponential $Vis-Z-L_a$ model is validated with the measured DSD with a FSSP at CESAR. Last, a more realistic approach is used to validate the model with the Vis, Z measurement data from the in situ visibility sensors and the cloud radar at CESAR. As we lack reliable L_a measurements in our datasets, we can only use DSD-derived L_a in the model.

Chapter 6 investigates the feasibility of developing an advanced fog-visibility radar. Starting with the performance analysis of the 35 GHz cloud radar at CESAR, we examine the effects of frequency, transmit power, and pulse width on the sensitivity of the radar. Based on the simulated DSD datasets for various fog types and evolutionary stages of fog, we calculate Z, L_a in a large range of frequency for various Vis levels. The operational parameters of a pulse-Doppler radar and a FMCW radar are respectively defined, and the transmit power P_t are calculated in a large range of frequency. The optimum frequency for each Vis level is chosen with the minimum P_t. To retrieve L_a by radar(s), dual-wavelength technique is introduced to provide L_a estimates, where LWC is retrieved from the differential attenuation between the dual-wavelength radars, and L_a is estimated from LWC based on the linear relationship between them in Rayleigh scattering regime. An error analysis on Vis estimates in terms of the $Vis-Z-L_a$ model is made in order to determine the optimum radar frequency pair for fog measurements.

Chapter 7 gives the conclusions and recommendations for future work.

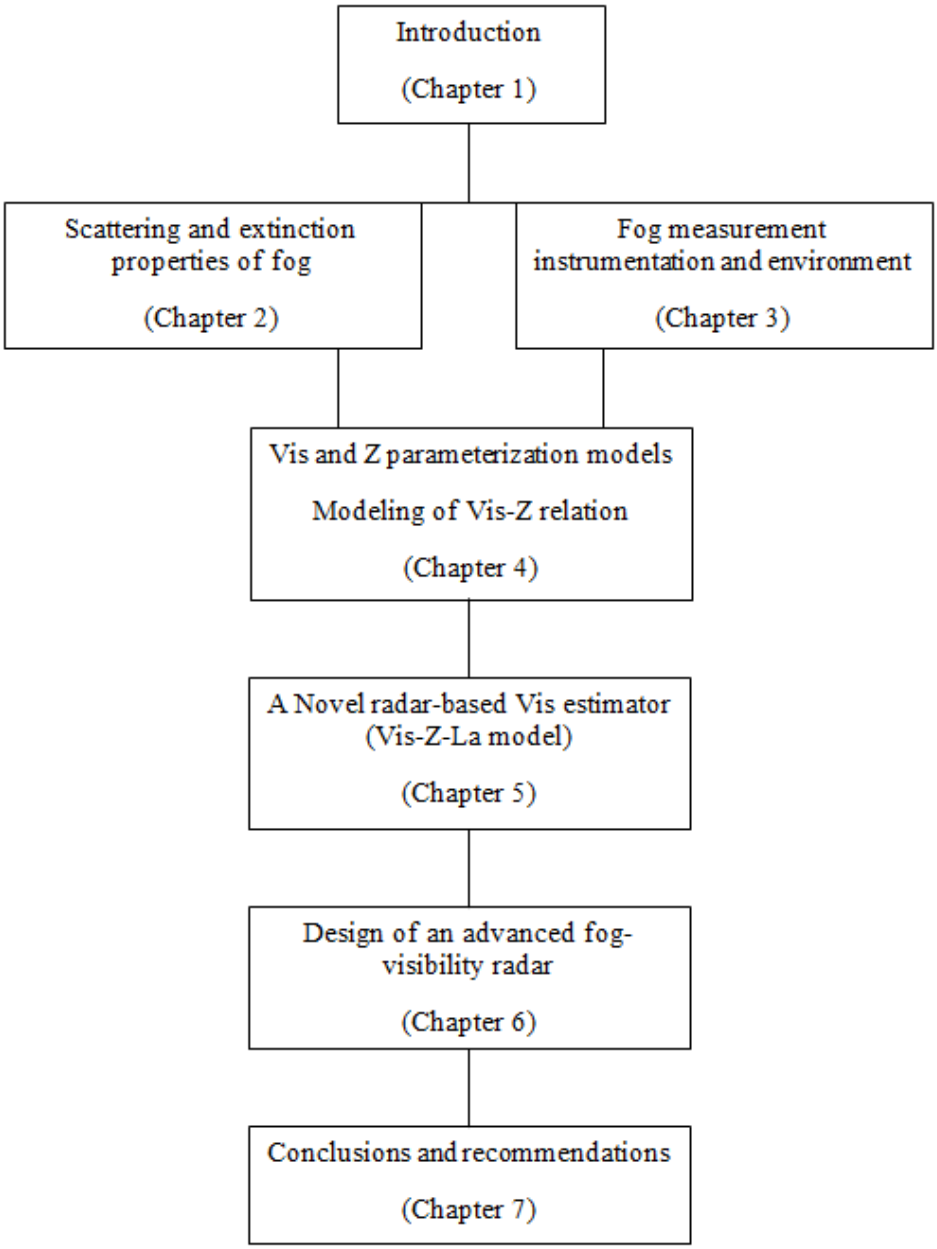

Figure 1.2: Outline of the thesis

2
Fog and its characteristics

2.1. Introduction

Fog is a crucial phenomenon in meteorology for its impacts on the reduction of visibility (Pruppacher et al., 1998). Short visible range can restrict land transportation, marine operations and low-level aviation (Bissonnette, 1992; Gazzi et al., 2001). Each year, the financial and human losses aroused by fog can be comparable to the losses from other catastrophic weather events, such as tornadoes, or even hurricanes (Gultepe et al., 2014). As a consequence, fog forecasting/nowcasting has been always the concern by most weather forecasters (Bergot and Guedalia, 1994; Guedalia and Bergot, 1994; Croft et al., 1997; Wright and Thomas, 1998; Zhou and Du, 2010). So far, many fog forecasting/nowcasting methods have been proposed (Pasini and Potestà, 1995; Reddy et al., 1995; Wantuch, 2001; Pasini et al., 2001; Hansen, 2007; Ruangjun and Exell, 2008; Clark et al., 2008; Haywood et al., 2008; Chmielecki and Raftery, 2011). The accurate forecasting/nowcasting of fog will facilitate the local authorities to make timely policies, reducing the losses from fog to the least (Leipper, 1995; Gultepe, 2008).

However, fog is the end result of complex interplay involving microphysical, thermodynamical, and dynamical processes (Duynkerke, 1991; Niu et al., 2010). To accurately forecast/nowcast fog often requires a better knowledge of the fog processes and its characteristics. The observation and modeling of the microphysical behaviors in fog will help us to understand better the fog processes (Brown, 1980; Bott et al., 1990; Bott and Trautmann, 2002; Gultepe and Milbrandt, 2007).

This chapter gives an overview of fog and its characteristics. It is structured as follows: in Section 2 the definition and classification of fog is discussed in detail; Section 3 describes the scattering and extinction properties of fog; Section 4 is the conclusion of this chapter.

2.2. Definition and classification of fog

2.2.1. Definition

Fog is an assemble of small liquid water droplets suspended near the earth's surface (Amelin, 1967; Zdunkowski and Nielsen, 1969; Zdunkowski and Barr, 1972; Pinnick et al., 1978; Brown, 1980; Hudson, 1980; Musson-Genon, 1987; Duynkerke, 1991). Meteorology definition of fog is based on visibility only. Visibility is defined as the greatest distance at which a black object can be seen and recognized against a white background (Seinfeld and Pandis, 2012). By international definition, fog occurs when the visibility is reduced to less than 1 km. If the visibility is reduced further to less than 200 m, then it is called dense fog. Very dense fog occurs when the visibility is less than 50 m. The only difference

between mist and fog is the visibility. Mist is distinguished from fog with the visibility between 1-5 km (Went, 1955). Haze is different from the fog and mist, and the restriction of visibility is arouse by dry aerosols which are from complex chemical compositions (Sun et al., 2006).

2

2.2.2. Classification of fog

Fog can be classified in terms of various standards. According to the status of fog, it can be divided into three main types at different temperatures: liquid fog at $T > -10^{\circ}$C, mixed phase fog at $-10^{\circ}\text{C} > T > -30^{\circ}$C, and ice fog at $T < -30^{\circ}$C (Petterssen and Petterssen, 1956). It should be noted that the division criteria are not always strict and they can vary in different conditions. Mixed phase fog may also occur at $T = -5^{\circ}$C while the temperature is sharply decreased during the night and plenty of water vapor is accumulated by the ice nuclei.

Defined by the weather conditions for the fog formation, fog can be divided into four main types: radiation fog, frontal fog, advection fog, and other fogs (Willett, 1928; Byers, 1959). Radiation fog includes ground fog, high inversion fog, advection-radiation fog, upslope fog, and mountain-valley fog. Frontal fog, formed together with precipitation, can be further divided into three subcategories: prefrontal, postfrontal and frontal passage fogs. Advection fog, termed as mixing fog, can be divided into sea fog, tropical air fog, land and sea-breeze fog, and steam fog. Other fogs include ice fog and snow fog which occur at very low temperatures. Considering the physical processes responsible for the fog formation and the circumstances under which the fog would probably occur, we mainly discuss several dominant fog types.

Radiation fog is formed by the nocturnal cooling of the surface boundary layer to a temperature at which its content of water vapor condenses (Taylor, 1917; Roach et al., 1976; Brown and Roach, 1976; Gerber, 1981). Normally, the formation of radiation fog requires three basic conditions, excessive aerosols near the ground, high relative humidity, and light winds (Pilié et al., 1975; Findlater, 1985). The radiation fog tends to form in the late night or the early morning, and lasts for a short duration (Turton and Brown, 1987; Fitzjarrald and Lala, 1989). The initial formation of radiation fog acts like a competition for the water vapor between the accumulation through radiative cooling and the driving-away by turbulence (Lala et al., 1975; Roach, 1976). Furthermore, the turbulence plays a complex role in the radiation fog formation (Bergot and Guedalia, 1994; Guedalia and Bergot, 1994; Roach, 1995). Light turbulence can be conductive to the fog formation, since it drives saturated air movements which can stimulate the activation of aerosols and the condensation growth of fog droplets. However, intense turbulence may be destructive to the fog formation due to the intense vertical mixing and quick drying-out of water vapor (Duynkerke, 1999). It was also found that the turbulence inhibited radiation fog formation but promoted fog development after its formation (Zhou and Ferrier, 2008). The complexity of turbulence adds the difficulty in forecasting/nowcasting the radiation fog.

Advection fog is formed by the advection of a warm moist air mass over a colder underlying surface. It can be divided into several subcategories according to the surface properties, which may be cold ground, snow cover, water, or ice (Byers, 1959). The formation of advection fog involves the dynamic and adiabatic processes of boundary layer

which require the advection of moisture and temperature, and the cooling of warm air mass continues until the dew point is reached (Pilié et al., 1979; Telford and Chai, 1993). Unlike radiation fog, advection fog can form and advect into a region at any time of the day with impelling air movements. Hence the turbulence also plays a very important role in the formation and development of advection fog (Lewis et al., 2003, 2004).

Evaporation fog is associated with advection and mixing, which forms by a cold air mass with a low vapor pressure lying over a relatively warm body of water (Saunders, 1964; Økland and Gotaas, 1995; Gultepe et al., 2003). The water evaporates into the cold air, and the overlying layer of air becomes saturated and then condenses into fog. Evaporation fog often forms over lakes and rivers, and it can occur at any time of the year.

Stratus-lowering fog is a significant fog type which results from the cloud base lowering down to the ground. It has been observed that the stratus-lowering fog is the most frequently occurring fog type in the Netherlands. The stratus-lowering process that leads to the formation of fog is caused by complex mechanisms (Peak and Tag, 1989; Duynkerke and Hignett, 1993; Tag and Peak, 1996). Radiative cooling at cloud top and large-scale subsidence are the primary mechanisms for the lowering of clouds (Oliver et al., 1978; Koračin et al., 2001; Dupont et al., 2012). Besides, entrainment is also an important factor that drives the stratus lowering to fog (Telford et al., 1984).

According to the life cycle of fog, fog can be divided into formation, mature, and dissipation stages (Pilié et al., 1975; Bott, 1991; Maier et al., 2013). In each stage, fog evolves with different dominant mechanisms. In the formation stage, most dry aerosols in saturated air are activated into wet aerosols and then condensed into fog droplets; in the mature stage, small fog droplets form into bigger ones due to the condensation growth, and the activation process still continues; in the dissipation stage, aerosols end up forming into fog droplets and the existing droplets are bound to evaporate due to the increasing air temperature and wind speed (Meyer et al., 1986; Noone et al., 1992; Elias et al., 2008; Stolaki et al., 2015).

2.3. Scattering and extinction properties of fog

2.3.1. Spectral models for the complex permittivity of water

Generally, fog is regarded as to be formed of liquid water. Hence it is necessary to calculate the complex permittivity of water in various conditions in order to determine the scattering and extinction properties of fog (Ray, 1972; Liebe and Hufford, 1989; Liebe, 1989). The spectral models for the complex permittivity of water are established over a large range of frequencies and temperatures.

The relative dielectric constant of water is referred to as complex permittivity, which is defined by:

$$\varepsilon = \varepsilon' + i\varepsilon'' \tag{2.1}$$

where ε' and ε'' are the real and loss parts of complex permittivity, and $i = \sqrt{-1}$.

Both the real and loss parts are dependent on the frequency f and temperature T, which can be described by the well-known Debye model (Eisenberg et al., 1969; Hasted, 1973). When f is below 100 GHz, the single Debye model proved to be adequate to describe $\varepsilon(f,T)$. While extending the f range beyond 100 GHz up to 1 THz, the double Debye model has been verified as a correct description of $\varepsilon(f,T)$ (Liebe et al., 1991).

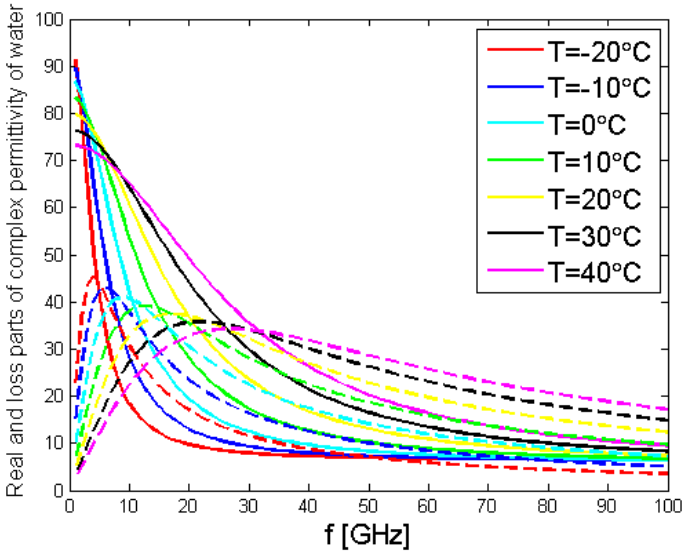

(a)

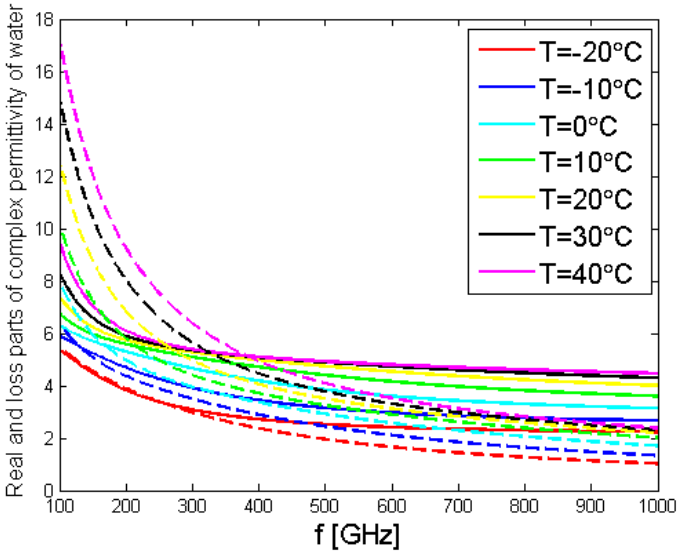

(b)

Figure 2.1: Spectral models for the complex permittivity of water in different frequency ranges $f < 100$ GHz (a) and 100 GHz $< f < 1$ THz (b) at various temperatures from -20°C to 40°C, where the solid lines represent the real parts of complex permittivity of water, and the dashed lines represent the loss parts.

Figure 2.1 shows the spectral models for the complex permittivity of water in different frequency ranges $f < 100$ GHz and 100 GHz $< f < 1$ THz at various temperatures from -20°C to 40°C.

2.3.2. Mie & Rayleigh scattering of fog

When a radar wave propagates into fog, the electromagnetic energy starts to transfer in a certain way (Hulst and Van De Hulst, 1957). All the energy in the process can be divided into backscattering, absorption, scattering and extinction parts (Mishchenko et al., 2002). Backscattering is the part that is reflected back in the direction from which the wave originates. When the travelling wave is intercepted, a certain amount of the energy will be absorbed by the fog, which leads to a heating energy, and that is the absorption. Scattering is the part that scatters in all directions, and backscattering is only one part of it. Extinction is the total energy that is lost through the process. According to the energy conservation theorem, the extinction is the sum of the scattering and absorption. However, for the lossy dielectric water, the scattering is a very small proportion of the lost energy, and most of the energy is absorbed by the fog and transferred into heat. Therefore, in most cases the absorption can be approximated as the extinction.

Typically, the degree to which the fog can scatter or absorb the energy is described by its cross section σ. The cross section is an effective area, used to indicate the amount of energy interacting with the fog. Assuming an incident wave with a power density S_i is intercepted by the fog, the energy is scattered isotropically and received by a receiver with a power density S_r in the direction described by the azimuth and elevation angle θ and ϕ with respect to the original wave. In this way, the cross section σ can be defined as (Skolnik, 1962):

$$\sigma(\theta,\phi) = 4\pi R^2 \frac{S_r(\theta,\phi)}{S_i} \tag{2.2}$$

where R is the distance between the fog and the receiver. It should be noted that in most cases the scattering is not isotropic, the forward scattering can dominate the backscattering when the fog droplets are much smaller than the wavelength and vice versa.

Accordingly, there are backscattering cross section σ_b, scattering cross section σ_s, absorption cross section σ_a, and extinction cross section σ_e. All the cross sections can be formulated through Mie theory as (Bohren and Huffman, 2008; Mätzler, 2002):

$$\sigma_b = \frac{\lambda^2}{4\pi}\left|\sum_{n=1}^{\infty}(2n+1)(-1)^n(a_n - b_n)\right|^2 \tag{2.3}$$

$$\sigma_s = \frac{\lambda^2}{2\pi}\sum_{n=1}^{\infty}(2n+1)(|a_n|^2 + |b_n|^2) \tag{2.4}$$

$$\sigma_e = \frac{\lambda^2}{2\pi}\sum_{n=1}^{\infty}(2n+1)Re(a_n + b_n) \tag{2.5}$$

$$\sigma_a = \sigma_e - \sigma_s \tag{2.6}$$

where the index n is from 1 to ∞, but the infinite series occurring in Mie formulas can be truncated at a maximum $n_{max} = x + 4x^{1/3} + 2$ (Bohren and Huffman, 2008), $x = 2\pi r/\lambda$ is termed as size parameter, r is the droplet radius, λ is the wavelength; the Mie scattering coefficients a_n, b_n, used to describe the amplitudes of the scattered field, are the

functions of x and complex refractive index, representing the magnetic and electric multipoles of order n respectively.

Furthermore, the cross section σ can be normalised to the particle cross section πr^2, and that is defined as efficiency factor $Q = \sigma/\pi r^2$. The efficiencies are expressed as (Hulst and Van De Hulst, 1957):

$$Q_b = \frac{1}{x^2}\left|\sum_{n=1}^{\infty}(2n+1)(-1)^n(a_n - b_n)\right|^2 \tag{2.7}$$

$$Q_s = \frac{2}{x^2}\sum_{n=1}^{\infty}(2n+1)(|a_n|^2 + |b_n|^2) \tag{2.8}$$

$$Q_e = \frac{2}{x^2}\sum_{n=1}^{\infty}(2n+1)Re(a_n + b_n) \tag{2.9}$$

$$Q_a = Q_e - Q_s \tag{2.10}$$

Since the fog droplets are very small compared to the wavelength, Rayleigh scattering regime can be considered to calculate the cross sections in an easier way. In the Rayleigh approximation, only the lowest order contributions in x are considered, and the cross sections can be simplified as (Hulst and Van De Hulst, 1957):

$$\sigma_b = \frac{\pi^5}{\lambda^4}|K|^2 D^6 = \frac{64\pi^5}{\lambda^4}|K|^2 r^6 \tag{2.11}$$

$$\sigma_s = \frac{2}{3}\frac{\pi^2}{\lambda^4}|K|^2 D^6 = \frac{128}{3}\frac{\pi^2}{\lambda^4}|K|^2 r^6 \tag{2.12}$$

$$\sigma_a = \frac{\pi^2}{\lambda}\mathrm{Im}(-K)D^3 = \frac{8\pi^2}{\lambda}\mathrm{Im}(-K)r^3 \tag{2.13}$$

where D is the droplet diameter; r is the droplet radius; K is the parameter related to the complex refractive index, which is given by $K = (m^2-1)/(m^2+2)$, m is the complex refractive index $m = \sqrt{\varepsilon} = n - i\kappa$, n is the refractive index, κ is the absorption coefficient. Like m, K is also dependent on the frequency and temperature.

Accordingly, the efficiencies can be simplified as (Hulst and Van De Hulst, 1957):

$$Q_b = 4x^4|k|^2 \tag{2.14}$$

$$Q_s = \frac{8}{3}x^4|K|^2 \tag{2.15}$$

$$Q_a = 4x\mathrm{Im}(-K) \tag{2.16}$$

It is important to determine the backscattering and extinction energy from fog since they are related to the amount of energy that can be received by the receiver (most are radars) and attenuated by the fog. As regards the fog, the scattering is only a very small part of the extinction compared to the absorption and thus the absorption can be approximated as the extinction.

Therefore, the backscattering and absorption characteristics of fog are investigated over a large range of frequencies and temperatures using Mie and Rayleigh scattering formulas respectively.

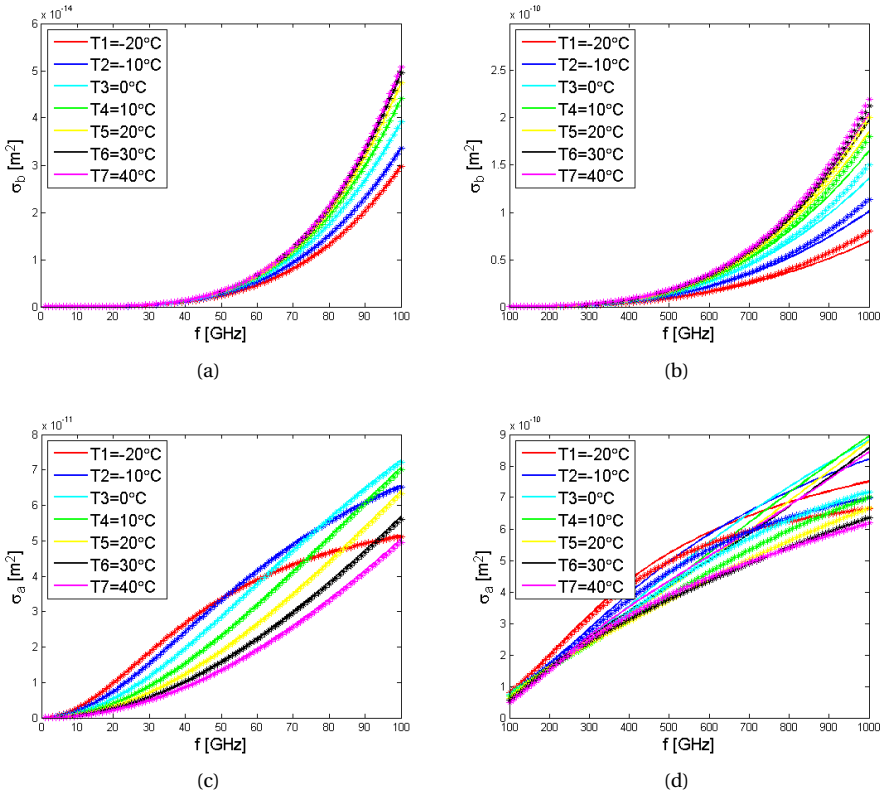

Figure 2.2: The backscattering and absorption cross sections σ_b, σ_a of a single fog droplet with $r = 25\ \mu m$ in different frequency ranges $f < 100$ GHz and 100 GHz $< f < 1$ THz at temperatures from -20°C to 40°C using Mie and Rayleigh scattering formulas respectively. (a), (b) show the backscattering cross sections σ_b in the frequency range $f < 100$ GHz and 100 GHz $< f < 1$ THz at temperatures from -20°C to 40°C, and (c), (d) show the absorption cross sections σ_a in the frequency range $f < 100$ GHz and 100 GHz $< f < 1$ THz at temperatures from -20°C to 40°C. The solid lines in (a), (b), (c), (d) represent the simulation results formulated with the Mie scattering, and the asterisks are formulated with the Rayleigh scattering.

Fog can be regarded as spherical water droplets with the sizes no more than 25 μm in radius (Eldridge, 1961). Since K is dependent on the frequency f, the single and double Debye models have to be used respectively in order to calculate the complex refractive index in a large range of frequencies. The backscattering and absorption cross sections σ_b, σ_a of a single fog droplet with $r = 25\ \mu m$ are simulated in different frequency ranges $f < 100$ GHz and 100 GHz $< f < 1$ THz at temperatures from -20°C to 40°C using Mie and Rayleigh scattering formulas respectively, which is shown in Figure 2.2, where the solid lines and asterisks represent the simulation results formulated with the Mie and Rayleigh scattering respectively.

It can be seen from Figure 2.2 that the frequency f and temperature T have different influences on the backscattering and absorption cross sections σ_b, σ_a. σ_b and σ_a

increase with increasing f in both frequency ranges $f < 100$ GHz and 100 GHz $< f < 1$ THz. Meanwhile, σ_b also increases with increasing T, but σ_a decreases with increasing T when $T > 0$°C.

In the frequency range $f < 100$ GHz, as shown in Figure 2.2(a) and (c), the σ_b, σ_a which are formulated with Mie scattering completely coincide with those formulated with Rayleigh scattering, which indicates that in the frequency range $f < 100$ GHz, the Rayleigh scattering can fully replace the Mie scattering to calculate the σ_b, σ_a of a single fog droplet with the size no more than 50 μm in diameter. However, in the higher frequency range 100 GHz $< f <$ 1 THz, which is shown in Figure 2.2(b) and (d), there are small differences between the Mie and Rayleigh scattering formulated σ_b, σ_a, and the differences tend to enlarge with increasing f. In the frequency range 100 GHz $< f <$ 1 THz, the Rayleigh scattering formulated σ_b are slightly larger than those formulated with the Mie scattering, but the Rayleigh scattering formulated σ_a turn to be smaller than the Mie scattering formulated σ_a.

Furthermore, the increase rates of σ_b, σ_a also vary with f and T. As shown in Figure 2.2(a) and (b), the increase rate of σ_b increases with increasing f in both frequency ranges $f < 100$ GHz and 100 GHz $< f <$ 1 THz. The increase rate of σ_a also increases with increasing f in the frequency range $f < 100$ GHz, but decreases with increasing f in the frequency range 100 GHz $< f <$ 1 THz, which is shown in Figure 2.2(c) and (d). Meanwhile, T also affects the increase rate of σ_a. When T is below 0°C, the increase rate of σ_a decreases with increasing f in both frequency ranges, which is shown in Figure 2.2(c) that the increase rates of σ_a at $T = -20$°C and $T = -10$°C decrease with increasing f. In the frequency range 100 GHz $< f <$ 1 THz, the increase rate of σ_a decreases even worse at $T < 0$°C, which is shown in Figure 2.2(d).

Next, the backscattering and absorption characteristics of fog droplets with a certain range of sizes are discussed. Since fog droplets are no more than 25 μm in radius, we divide the size range to $r = 1, 5, 10, 15, 20, 25$ μm. The backscattering and absorption cross sections σ_b, σ_a of fog droplets with the size range are simulated in different frequency ranges $f < 100$ GHz and 100 GHz $< f <$ 1 THz at $T = 10$°C using Mie and Rayleigh scattering formulas respectively, which is shown in Figure 2.3, where the solid lines and asterisks represent the simulation results formulated with the Mie and Rayleigh scattering respectively.

It can be seen from Figure 2.3 that σ_b and σ_a increase with increasing r in both frequency ranges $f < 100$ GHz and 100 GHz $< f <$ 1 THz. The small differences between the Mie and Rayleigh scattering formulated σ_b, σ_a still exist in the frequency range 100 GHz $< f <$ 1 THz and enlarge with increasing f, which is shown in Figure 2.3(b) and (d). The variations of the increase rates of σ_b, σ_a with increasing f maintain the same trends as shown in Figure 2.2.

In Figure 2.3, the backscattering and absorption cross sections σ_b, σ_a are simulated at a positive temperature $T = 10$°C. In order to see the influences of T on σ_b, σ_a, they are simulated at a negative temperature $T = -10$°C, which is shown in Figure 2.4.

It is shown in Figure 2.4 that σ_b decreases but σ_a increases with decreasing T. The negative temperature $T = -10$°C also leads to the decrease of the increase rate of σ_a with increasing f, but does not affect the increase rate of σ_b. The reason is that both σ_b and σ_a are related to K, which depends on the frequency f and temperature T. Furthermore,

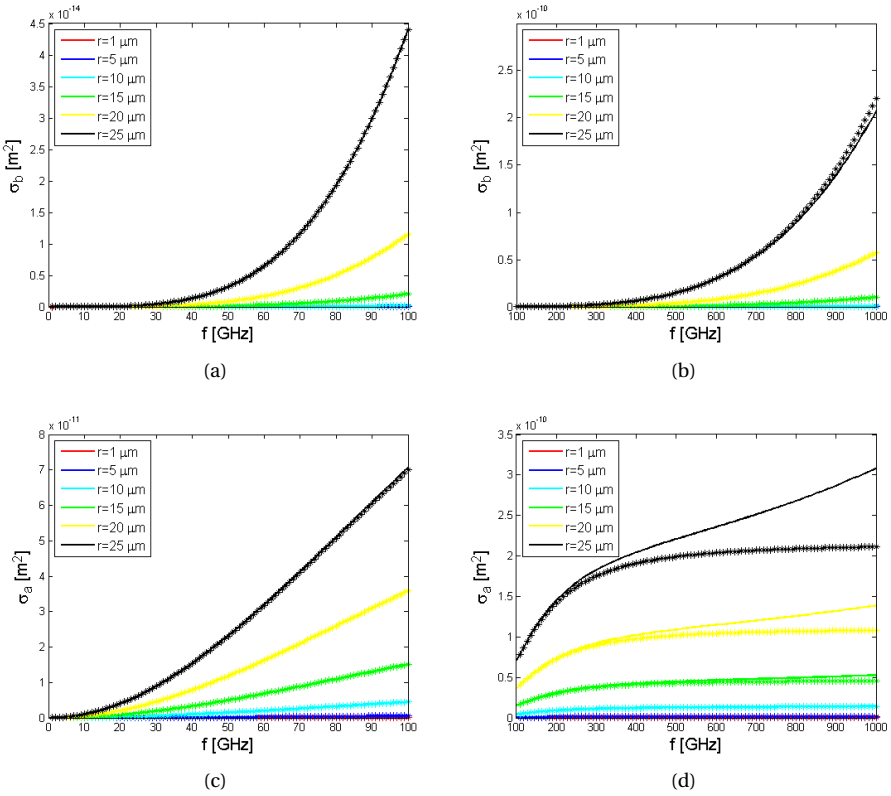

Figure 2.3: The backscattering and absorption cross sections σ_b, σ_a of fog droplets with a certain range of sizes $r = 1, 5, 10, 15, 20, 25\ \mu m$ in different frequency ranges $f < 100$ GHz and 100 GHz $< f < 1$ THz at $T = 10°$C using Mie and Rayleigh scattering formulas respectively. (a), (b) show the backscattering cross sections σ_b with $r = 1, 5, 10, 15, 20, 25\ \mu m$ in the frequency range $f < 100$ GHz and 100 GHz $< f < 1$ THz at $T = 10°$C, and (c), (d) show the absorption cross sections σ_a with $r = 1, 5, 10, 15, 20, 25\ \mu m$ in the frequency range $f < 100$ GHz and 100 GHz $< f < 1$ THz at $T = 10°$C. The solid lines in (a), (b), (c), (d) represent the simulation results formulated with the Mie scattering, and the asterisks are formulated with the Rayleigh scattering.

σ_b depends on the amplitude of K, and σ_a depends on the imaginary part of K. Compared to the amplitude of K, the imaginary part of K is more affected by the temperature T.

All in all, we have simulated the backscattering and absorption cross sections σ_b, σ_a of a single fog droplet with various sizes in a large frequency range 1 GHz $< f <$ 1000 GHz at temperatures from $-20°$C to 40°C. σ_b, σ_a form the basis for computing the reflection and attenuation from fog, which we would use as the input of our proposed model in the following chapters. Meanwhile, the backscattering and absorption characteristics of fog are investigated at very high frequencies because the fog droplets are so small that we would consider using very high frequency radars to measure the fog.

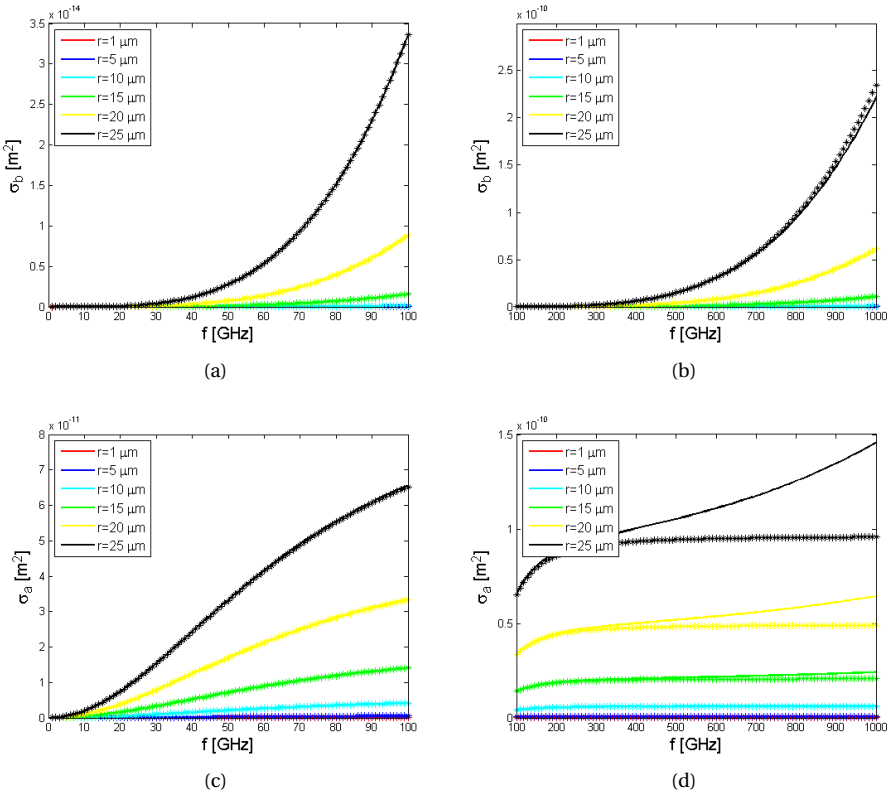

Figure 2.4: The backscattering and absorption cross sections σ_b, σ_a of fog droplets with a certain range of sizes $r = 1,5,10,15,20,25\ \mu m$ in different frequency ranges $f < 100$ GHz and 100 GHz $< f < 1$ THz at $T = -10°$C using Mie and Rayleigh scattering formulas respectively. (a), (b) show the backscattering cross sections σ_b with $r = 1,5,10,15,20,25\ \mu m$ in the frequency range $f < 100$ GHz and 100 GHz $< f < 1$ THz at $T = -10°$C, and (c), (d) show the absorption cross sections σ_a with $r = 1,5,10,15,20,25\ \mu m$ in the frequency range $f < 100$ GHz and 100 GHz $< f < 1$ THz at $T = -10°$C. The solid lines in (a), (b), (c), (d) represent the simulation results formulated with the Mie scattering, and the asterisks are formulated with the Rayleigh scattering.

2.3.3. Characteristic parameters of fog

Following above, the values of the backscattering and absorption cross sections σ_b, σ_a can be described by a series of characteristic parameters related to fog which can be measured by the in-situ and remote sensing instruments. When a radar is utilized to measure fog, radar reflectivity factor is often used to describe the amount of energy reflected by the fog droplets and received by the radar receiver (Sauvageot, 1992). The radar reflectivity factor is meteorologically a more meaningful way of expressing the radar reflectivity and is often just referred to as radar reflectivity. Therefore, radar reflectivity factor is defined as a measure of the amount of energy reflected by particulates in the atmosphere (Probert-Jones, 1962). In Rayleigh approximation, the backscattering cross section σ_b of a single fog droplet is approximated as in Eq. (2.11). The total vol-

umetric backscattering cross section is a combination of all the fog droplets within the volume. To sum up all the droplets in both sides of Eq. (2.11),

$$\sum_{i=1}^{N} \sigma_{b_i} = \frac{\pi^5}{\lambda^4} |K|^2 \sum_{i=1}^{N} D_i^6 \tag{2.17}$$

where $\eta = \sum_{i=1}^{N} \sigma_{b_i}$ is the volumetric reflectivity; $Z = \sum_{i=1}^{N} D_i^6$ is the reflectivity factor.

The radar reflectivity can be expressed in the form of integration,

$$Z = \int_0^\infty n(D) D^6 dD \times 10^{-12} = 64 \int_0^\infty n(r) r^6 dr \times 10^{-12} \tag{2.18}$$

where D is the droplet diameter in μm; r is the droplet radius in μm; $n(D)$, $n(r)$ are the drop size distribution (DSD) in units of $\mu m^{-1} \cdot cm^{-3}$, which indicates the number concentration of droplets per unit volume and per unit of diameter/radius increment; Z is the radar reflectivity in mm^6/m^3, and it is often expressed on a logarithmic scale in units of dBZ.

Moreover, visibility is a simple and direct parameter to describe the fog intensity, since it is intuitive that heavy fogs often have low visibility and light fogs have high visibility. Academically, visibility is defined as the greatest distance at which a black object can be seen and recognized against a white background (Seinfeld and Pandis, 2012), which is expressed as:

$$Vis = \frac{-\ln \epsilon}{\beta_{ext}} \times 10^{-3} \tag{2.19}$$

$$\beta_{ext} = \int_0^\infty Q_{ext} n(r) \pi r^2 dr \times 10^{-6} \tag{2.20}$$

where Vis is the visibility in km; ϵ is the threshold of contrast with human eyes and normally sets to 0.05; β_{ext} is the extinction coefficient in m^{-1}; Q_{ext} is the extinction efficiency. In practice, the visual range is often evaluated at $\lambda = 0.55\ \mu m$ which is the wavelength of green light, where the human eyes have maximum sensitivity.

Q_{ext} is a complex function of r, λ and refractive index m as in Eq. (2.9). The general behavior of Q_{ext} as a function of r at $\lambda = 0.55\ \mu m$ is shown in Figure 2.5.

It is shown in Figure 2.5 that for sufficiently large values of r, Q_{ext} oscillates around its asymptotic value $Q_{ext} = 2$. Considering the continuous sizes of fog droplets between 1-25 μm in radius, the weighted value of Q_{ext} can be approximated as 2, which is the case for fog droplets. In this way, taking Q_{ext} as 2 is convenient for the calculation of Vis (Pinnick et al., 1979).

Additionally, attenuation is an important parameter to describe the amount of energy that is lost in the fog (Vasseur and Gibbins, 1996). The attenuation is equivalent to the extinction, which is the sum of scattering and absorption by the fog droplets. Attenuation factor is the two-way integral of the attenuation coefficient over distance, which is formulated as (Doviak and Zrnic, 2014):

$$l_a = \exp(2 \cdot \int_0^R k_a dR) \tag{2.21}$$

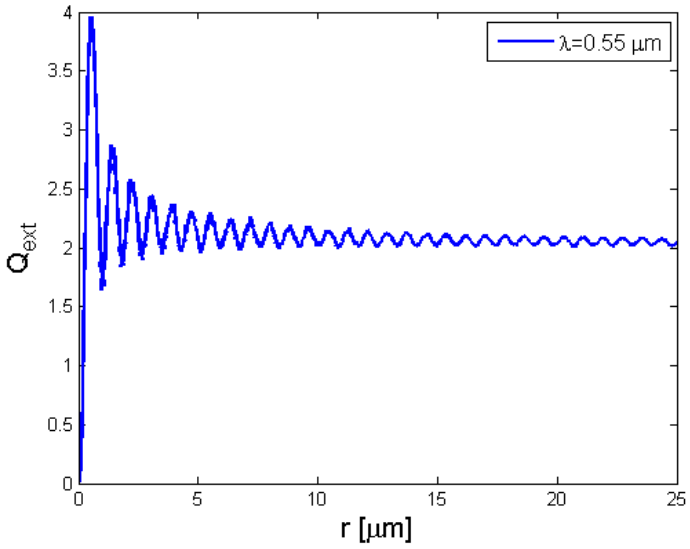

Figure 2.5: Q_{ext} as a function of r with $\lambda = 0.55\ \mu m$.

where l_a is the dimensionless attenuation factor; k_a is the attenuation coefficient in m^{-1}; R is the distance in m.

The attenuation coefficient k_a is the combination of the extinction cross section σ_e for all the droplets in unit volume, which is expressed as:

$$k_a = \int_0^\infty n(r)\sigma_e(r)dr \times 10^6 \tag{2.22}$$

where $\sigma_e = \sigma_a + \sigma_s$ is the extinction cross section in m^2; $n(r)$ is the drop size distribution in $\mu m^{-1} \cdot cm^{-3}$; k_a is in m^{-1}.

Since the scattering cross section σ_s is proportional to the sixth power of the droplet diameter as in Eq. (2.12), it is smaller than the absorption cross section σ_a as in Eq. (2.13) for very small fog droplets. Therefore, the attenuation coefficient can be approximated as:

$$k_a = \int_0^\infty n(r)\sigma_a(r)dr \tag{2.23}$$

In Rayleigh approximation, k_a can be further simplified by substituting Eq. (2.13) into Eq. (2.23),

$$k_a = \frac{8\pi^2}{\lambda}\mathrm{Im}(-k)\int_0^\infty n(r)r^3 dr \times 10^{-12} \tag{2.24}$$

where λ is the radar wavelength in m.

Besides, the liquid water content LWC is a measure of the mass of water in fog in a specified amount of dry air. LWC varies greatly with different fog types and evolutionary

stages of fog (Houghton and Radford, 1938; Gerber, 1984). It is formulated as:

$$LWC = \frac{4\pi}{3}\rho_w \int_0^\infty n(r) r^3 dr \times 10^{-12} \tag{2.25}$$

where LWC is in $g \cdot m^{-3}$; $\rho_w = 10^6\ g \cdot m^{-3}$ is the density of water.

By combining Eq. (2.24) and Eq. (2.25), k_a can be expressed in terms of LWC as:

$$k_a = \frac{6\pi \cdot LWC}{\rho_w \lambda} \mathrm{Im}(-K) \tag{2.26}$$

where k_a is in m^{-1}; LWC is in $g \cdot m^{-3}$; λ is in m.

Substituting Eq. (2.26) into Eq. (2.21), and taking logarithm in both sides, we can express the k_a in units of dB/km as:

$$L_a = 2 \cdot 0.4343 \cdot \frac{6\pi \cdot LWC}{\lambda} \mathrm{Im}(-K) \tag{2.27}$$

where L_a is the attenuation factor in dB/km; λ is the radar wavelength in cm; LWC is the liquid water content in $g \cdot m^{-3}$; the value 2 denotes the two-way integral of attenuation. It can be seen from Eq. (2.27) that L_a in dB/km is proportional to the LWC, which illuminates a way of estimating L_a from the LWC. Besides, L_a is also dependent on the factors that are related to K, such as the frequency f and temperature T.

The attenuation factor of fog droplets L_a is also simulated in different frequency ranges $f < 100$ GHz and 100 GHz $< f <$ 1 THz at temperatures from -20°C to 40°C, which is shown in Figure 2.6. The fog LWC is assumed as 0.02 $g \cdot m^{-3}$, which is usually smaller than the LWC in clouds and rains.

It is shown in Figure 2.6 that the L_a increases with increasing f and decreasing T in both frequency ranges $f < 100$ GHz and 100 GHz $< f <$ 1 THz. In the frequency range 100 GHz $< f <$ 1 THz, the increase rate of L_a decreases with increasing f. When T is below 0°C, the increase rate of L_a decreases with increasing f in both frequency ranges. It can be found that the increase rate of L_a with increasing f has the same variations with the increase rate of σ_a in the same range of frequencies and temperatures.

Besides the attenuation induced by fog droplets, the gaseous attenuation from oxygen and water vapor also has to be considered. A simplified algorithm is used for approximate estimation of gaseous attenuation in the frequency range 1-350 GHz for a limited range of meteorological conditions and a limited variety of geometrical configurations (Gibbins, 1986; Geneva, 1995). Figure 2.7 shows the total attenuation factor of gases L_g in the frequency range 1-350 GHz at temperatures from -20°C to 40°C, where the water vapor density is assumed as 7.5 $g \cdot m^{-3}$. It can be seen from Figure 2.7 that the L_g reaches maximum values at $f = 60, 183, 325$ GHz relative to the adjacent frequencies, indicating that the gaseous attenuation can be quite large near these frequencies. Therefore, the use of radars should avoid these frequencies for atmospheric measurements. Just like as L_a, the L_g also increases with decreasing T, and roughly increases with increasing f if eliminating the 3 strong frequency absorption bands.

The radar reflectivity Z, visibility Vis, and attenuation factor of fog droplets L_a are all functions of the moments of DSD. DSD is an important parameter which specifies the numbers and sizes of droplets in each sampling volume (Best, 1951; Baronti and Elzweig,

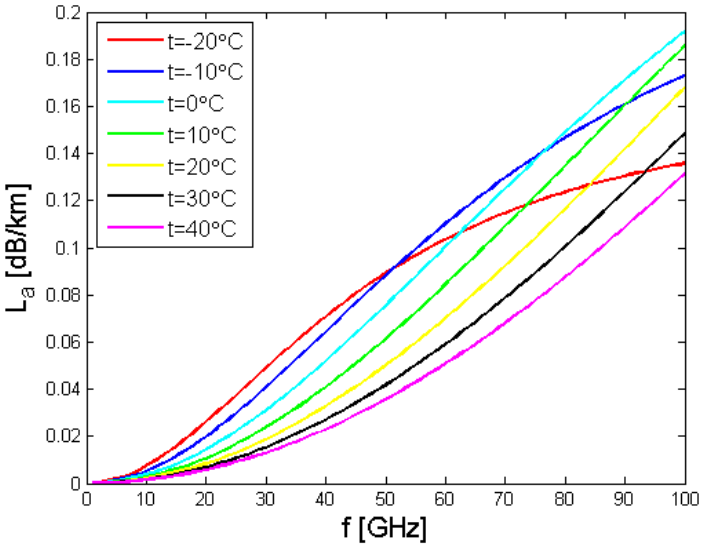

(a)

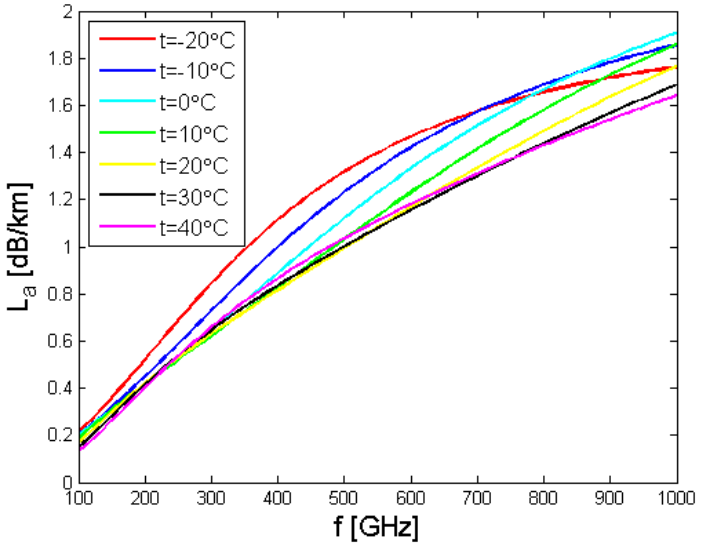

(b)

Figure 2.6: The attenuation factor of fog droplets L_a in different frequency ranges $f < 100$ GHz (a) and 100 GHz $< f < 1$ THz (b) at temperatures from -20°C to 40°C, where the fog LWC is assumed as 0.02 $g \cdot m^{-3}$.

1973; Mallow, 1975). Given the DSD, the characteristic parameters of fog can be deter-

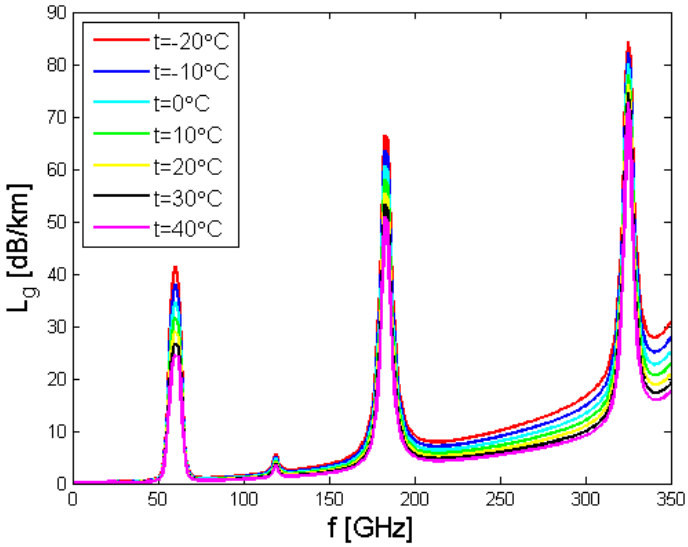

Figure 2.7: The attenuation factor of gases L_g in the frequency range 1 – 350 GHz at temperatures from −20°C to 40°C, where the water vapor density is assumed as 7.5 $g \cdot m^{-3}$.

mined. However, it is difficult to generalize the fog DSD due to the spatial and temporal variations. For different types and life cycle stages of fog, the DSD is also different (Best, 1951; Eldridge, 1961; Baronti and Elzweig, 1973; Mallow, 1975). Many DSD measurement and retrieval techniques have been proposed (Eldridge, 1957; Silverman et al., 1964; Garland, 1971; Kunkel, 1971; Cerni, 1983; Brenguier et al., 1998; Miles et al., 2000; Brandes et al., 2004a,b). Based on statistical analysis, the Gamma distribution is often used to represent the fog DSD (Clark, 1974; Tampieri and Tomasi, 1976; Miles et al., 2000), which is defined by:

$$n(r) = \frac{N}{R_n^{\upsilon} \cdot \Gamma(\upsilon)} \cdot r^{\upsilon-1} \cdot e^{-\frac{r}{R_n}}, r \geq 0 \tag{2.28}$$

where N is the total number concentration in cm^{-3}; $\Gamma(\upsilon)$ is the Gamma function; υ and R_n are the shape and scale parameters of the Gamma distribution.

The basic integrated quantities such as number concentration N, mean and effective radius r_m, r_e, standard deviation of radius about the mean radius σ, and liquid water content LWC can also be determined if the DSD is known.

$$N = \int_0^{\infty} n(r)dr \tag{2.29}$$

$$r_m = \frac{\int_0^{\infty} n(r)rdr}{\int_0^{\infty} n(r)dr} \tag{2.30}$$

$$r_e = \frac{\int_0^{\infty} n(r)r^3dr}{\int_0^{\infty} n(r)r^2dr} \tag{2.31}$$

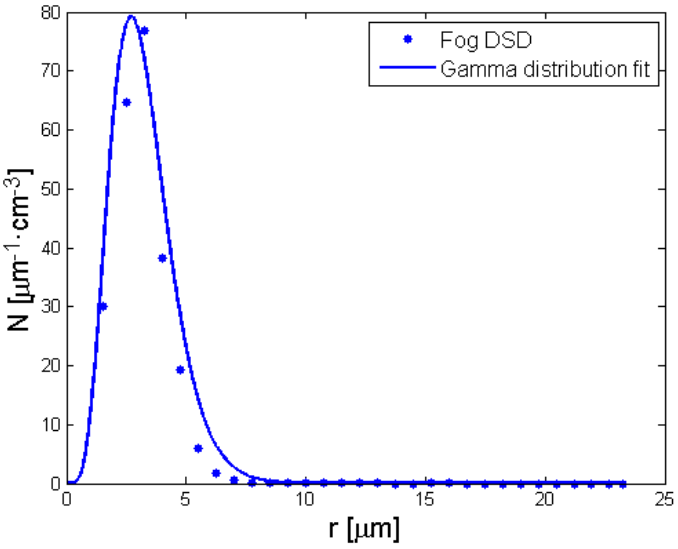

Figure 2.8: The DSD of a radiation fog observed at Cabauw, in the Netherlands on December 21-22, 2011. The Gamma distribution is fit to the fog DSD with the least squares errors.

$$\sigma = \left(\frac{\int_0^\infty n(r) \cdot (r - r_m)^2 dr}{N} \right)^{1/2} \tag{2.32}$$

$$LWC = \frac{4\pi}{3} \rho_w \int_0^\infty n(r) r^3 dr \times 10^{-12} \tag{2.33}$$

where $n(r)$ is the drop size distribution in $\mu m^{-1} \cdot cm^{-3}$; N is the number concentration in cm^{-3}; r_m, r_e are the mean and effective radius in μm; σ is the standard deviation of radius in μm; LWC is the liquid water content in $g \cdot m^{-3}$.

Figure 2.8 shows the DSD of a radiation fog which was observed at CESAR on December 21-22, 2011. CESAR is a large observatory site for atmospheric research in the Netherlands, and it has carried out many research activities in atmospheric observation. The radiation fog was formed in the night before, and disappeared in the next early morning. It lasted for nearly 7 hours. During the fog episode the visibility was reduced to less than 100 m at a minimum.

The least squares method is used to fit the Gamma distribution to the DSD of the radiation fog. It can be seen from Figure 2.8 that the DSD of the radiation fog can be well represented by the Gamma distribution in the first several channels of the DSD. The maximum number concentration is reached at $r = 3.25\ \mu m$, which is termed as peak radius, and there are hardly fog droplets with the sizes larger than 7 μm in radius.

2.4. Conclusion

This chapter mainly introduced the fog and its characteristics. Fog is meteorologically defined on the visibility only. Normally, fog occurs when visibility is reduced to less than

1 km. Dense fog and very dense fog are defined as visibility reduced to less than 200 m and 50 m. Mist is distinguished from fog with visibility between 1-5 km. In terms of the various weather conditions for fog formation, fog can be divided into different types, and each fog type has different dominant mechanisms in the life cycle stage. In this chapter, we mainly introduced the commonly occurring fog types such as the radiation fog, advection fog, evaporation fog, and stratus-lowering fog. The stratus-lowering fog is the most frequently occurring type in the Netherlands, which has been observed and documented at CESAR.

The scattering and extinction properties of fog are the basis for exploring fog-related questions. According to the energy conservation theorem, the scattering can be divided into backscattering and diffuse scattering, and absorption is a large part of the extinction. The backscattering cross section σ_b, scattering cross section σ_s, absorption cross section σ_a, and extinction cross section σ_e were then defined to describe each part of the energy interacting with the fog. Among the characteristic parameters of fog, radar reflectivity Z is correlated to the backscattering, and visibility Vis, attenuation L_a are correlated to the extinction. The extinction can be approximated as the absorption from fog droplets because the scattering is too small compared to the absorption. Therefore, the backscattering and absorption characteristics of fog were investigated over a large range of frequency, temperature and droplet sizes. The simulation results showed that the backscattering is positively correlated with the frequency, temperature and droplet sizes, while the absorption is positively correlated with the frequency and droplet sizes, but is negatively correlated with the temperature. Meanwhile, the frequency and temperature also influence the increase rates of σ_b, σ_a with increasing frequency. The increase rates of σ_b, σ_a increase with increasing frequency in the lower frequency range $f < 100$ GHz, while in the higher frequency range 100 GHz $< f <$ 1 THz, the increase rate of σ_b still increases with increasing frequency but the increase rate of σ_a turns to decrease with increasing frequency. The increase rate of σ_a is also affected by the temperature. When the temperature is below 0°C, the increase rate of σ_a will decrease with increasing frequency in both frequency ranges.

Mie and Rayleigh scattering were compared for the calculation of σ_b, σ_a over a large range of frequency, temperature and droplet sizes. It is found that for the fog droplets with the sizes no more than 25 μm in radius, the differences between the Mie and Rayleigh scattering formulated σ_b, σ_a are very small in the frequency range $f < 300$ GHz. Therefore, the Rayleigh scattering can often replace the Mie scattering for the simple calculation of the radar backscattering and absorption of the fog.

Three characteristic parameters of fog were then defined and formulated in Rayleigh approximation. Radar reflectivity Z and visibility Vis, attenuation factor L_a are respectively correlated to the radar backscattering and absorption of the fog. DSD is a significant parameter that connects all the characteristic parameters. Once the DSD is determined, Z, Vis and L_a can be calculated. Most statistical analysis employs the Gamma distribution as the fog DSD. The DSD of a radiation fog at CESAR was shown and represented by the Gamma distribution.

3

Fog measurements at CESAR in the Netherlands

3.1. Introduction

CESAR is the Cabauw Experimental Site for Atmospheric Research which is affiliated with the Royal Netherlands Meteorological Institute (KNMI) (Russchenberg et al., 2002). The CESAR observatory is located in the western part of the Netherlands (51.97°N, 4.93°E) in a rural spacious grassland. At this site a large number of instruments are operated to study the atmosphere and its interaction with the earth. A large scope of research work has been carried out at CESAR which includes the monitoring of long term tendencies in atmospheric changes, the weather and climate modeling, the validation of space-borne retrievals, and the development and implementation of new measurement techniques (Russchenberg et al., 2005). Meanwhile, a great many universities and research institutes have been attracted to proceed with research activities at CESAR and have built up long-term cooperative relationships with CESAR. Generally speaking, there are three sets of instruments at CESAR deployed for the integrated profiling of atmosphere. They are tower-based in situ, ground-based in situ, and ground-based remote sensing instruments. A synergy of the instruments can measure a wide range of thermodynamical, microphysical, and radiation parameters of the atmosphere (Driedonks et al., 1978; Van Ulden and Wieringa, 1996,?).

A 213-m tower at CESAR is installed with in situ sensors at the 2-, 10-, 20-, 40-, 80-, 140-, and 200-m levels which measure the temperature, humidity, wind speed and direction at these levels. The accuracies of temperature and humidity measurements are 0.1°C and 1%. Meanwhile, the BSRN (Baseline Surface Radiation Network) at CESAR supplies the radiative quantities between the atmosphere and the earth. The other active instruments employed in the fog campaign include a FSSP (Forward Scattering Spectrometer Probe), a SMPS (Scanning Mobility Particle Sizer), a Vaisala FD12P probe, Biral SWS-100 sensors, a cloud radar at 35 GHz, a ceilometer CT75, and a multi-wavelength microwave radiometer (Monna and Van der Vliet, 1987). We are aimed to utilize the synergy of the instruments to measure fog in conjunction, in order to obtain more information about the fog. The observed parameters with the relevant instruments will be illustrated in the following section.

A comprehensive fog observation campaign was carried out at CESAR in the season November 2011 - March 2012. It is the first time that complete fog cycles (formation and dissipation) have been systematically measured in the Netherlands. During the fog campaign, a great many in situ and remote sensing instruments were actively used to measure the thermodynamical and microphysical parameters of fog, and the microphysical

Figure 3.1: The FSSP mounted at 60-m level of the CESAR tower.

processes of fog can be better understood from the analysis on the observed parameters.

In the season 2011 - 2012 there were 35 fog cases observed at CESAR, of which 23 cases are classified as stratus-lowering fog, 10 cases as radiation fog, 1 case as advection fog, and 1 case is unknown. It was a pity that there was only one fog case occurred on February 17-18, 2012 where all the instruments at CESAR were simultaneously working for the measurements. Almost two thirds of the fog cases are developed from low clouds. The reason could be humid subtropical oceanic air associated with warm sector or otherwise with relatively stable high pressure/ridging situations was striking over a cooler surface, a situation that is similar to the occurrence of sea fog.

This chapter introduces the measurement site in the Netherlands and addresses the instruments for fog measurements. It is structured as follows: Section 2 describes the measurement setup during the fog campaign at CESAR in the Netherlands; in Section 3, the meteorological radar equation is deduced with considering the atmospheric attenuation, and the sensitivity of the 35 GHz cloud radar at CESAR is evaluated in fog conditions; Section 4 is the conclusion of this chapter.

3.2. Measurement setup at CESAR

3.2.1. Fog DSD and FSSP

Fog DSD was measured by a FSSP which was installed at 60-m level of the CESAR tower. The FSSP belongs to the class of OPC (Optical Particle Counter) instruments which determine the sizes and numbers of particles by measuring the intensity of light that each particle scatters when passing through a light beam (Dye and Baumgardner, 1984). The range of particles measured by the FSSP at CESAR is between 3 - 46.5 μm in diameter, and the size range is divided into 30 size bins with each 1.5 μm. Figure 3.1 shows the FSSP mounted at 60-m level of the CESAR tower.

In addition, a SMPS was installed in the basement of the CESAR research facility to

(a) (b)

Figure 3.2: The 213-m CESAR tower (a) and the Biral SWS-100 sensors (b) mounted on the tower.

measure the dry aerosol spectra (Boers et al., 2013). There was an aerosol inlet mounted at 60-m level of the CESAR tower taking in the aerosols at this level which were piped down to the SMPS. The range of particles measured by the SMPS is between 0.0025 - 1 μm in diameter.

3.2.2. Fog visibility and Biral SWS-100 sensors

Fog visibility was measured by Biral SWS-100 sensors which were installed at the 2-, 10-, 20-, 40-, 80-, 140-, and 200-m levels of the CESAR tower. The forward scatter measurement principle and unique design of the SWS-100 ensure the visibility measurements are accurate and reliable in all weather conditions and will not be influenced by the local light sources (Li et al., 2015). The visibility resolution of the SWS-100 is 10 m and the accuracy is 10% at the maximum. Meanwhile, the ground visibility has been measured at the AWS (Automated Weather Station) of CESAR with a Vaisala FD12P probe. Figure 3.2 shows the 213-m CESAR tower and the Biral SWS-100 sensors mounted on the tower.

3.2.3. Fog reflectivity and cloud radar at 35 GHZ

Fog reflectivity was measured by a 35 GHz cloud radar at CESAR. The cloud radar is a typical pulse Doppler radar which measured the fog in a so-called “fog mode”. Since the cloud radar normally operates in zenith mode, it would yield no information about the fog, because the first range gate of the cloud radar is still higher than the top of fog, which in the Netherlands is normally lower than 200 m (Duynkerke, 1999). In order to detect the fog, a light-weight aluminum reflector was placed above the antenna of the radar, by which the radar beam is mirrored from vertical direction to 3.5° elevation. In this way, the radar beam can adequately propagate in the fog so that the microphysical structures of fog can be observed in detail. The “fog mode” was only operated when the

Figure 3.3: The 35 GHz cloud radar at CESAR is being prepared for the “fog mode”.

fog conditions were deemed promising in the daily forecast, and the reflector was turned back to its normal position after fog dissipated. In the “fog mode”, the minimum vertical height that the radar can detect is $250 \cdot sin(3.5^\circ - 0.34^\circ/2) + 5 = 19.5$ m, where 250 m is the minimum detection range of the radar, 0.34° is the 3-dB beam width, 5 m is the height of the antenna.

However, there are disadvantages in this mode of operation. One is that the radar signals will be contaminated by the ground clutter due to the antenna side lobes. The radar echoes of fog are too weak to be distinguished from the ground reflections. Therefore, the radar data are further processed by the Doppler technique to eliminate the ground clutter. Normally, the radar data in the first two range gates are preferred not to be used. Another disadvantage is that the radar range gate data are not well collocated with the other in situ data in time and space. The radar measurements are taken over a certain area, which does not fully coincide with the visibility or DSD measurement inlets. The optimum measurement data are those that were taken at close levels in the same time slots if all the source data are to be used in conjunction.

Figure 3.3 shows the 35 GHz cloud radar being prepared to operate in the “fog mode”, and Figure 3.4 shows the layout of radar measurements during fog episodes.

In addition, a ceilometer CT75 was used to measure the backscatter profiles of fog and to retrieve the heights of fog base. The ceilometer can detect up to three fog bases every 30 seconds. Besides, a 14 channel microwave radiometer (HATPRO) was used to measure the sky brightness temperature in the water vapor band (20-30 GHz) and the oxygen band (50-60 GHz), from which the column integrated liquid water (LWP) and the column integrated water vapor (IWV) of fog can be retrieved.

3.3. Sensitivity evaluation of the 35 GHz cloud radar for fog measurements

In order to detect fog with the 35 GHz cloud radar, it is important to evaluate the radar sensitivity in fog conditions (Smith, 1986). Table 3.1 lists the operational parameters of

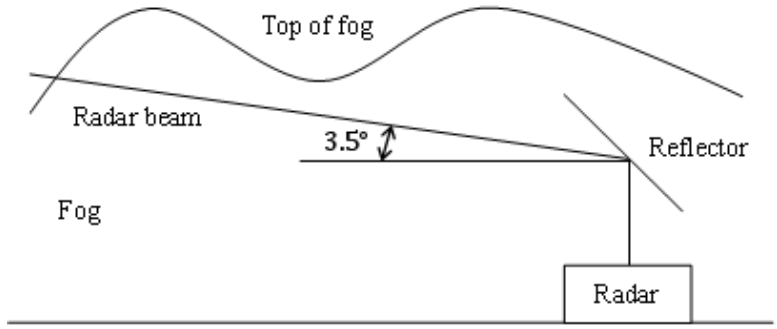

Figure 3.4: The layout of radar measurements during fog episodes.

the 35 GHz cloud radar in the "fog mode".

The radar equation for a point target is expressed as (Skolnik, 1970):

$$P_r = \frac{P_t G_t G_r \lambda^2 \sigma}{(4\pi)^3 R^4} \tag{3.1}$$

where P_r is received power; P_t is transmitted power; G_t is transmitted antenna gain; G_r is received antenna gain; λ is the radar wavelength; σ is the radar cross section of the point target; R is the distance between the radar and the target.

Fog column is regarded as a volume filled with plenty of water droplets. To account for this, the radar cross section in Eq. (3.1) should be replaced with the sum of the radar cross sections of all the distributed particles in the resolution volume.

$$\sigma = \sum_{i=1}^{N} \sigma_i \tag{3.2}$$

where the sum is taken over all N particles in the resolution volume.

The range resolution volume V is given by (Skolnik, 1970):

$$V = \pi \frac{R\theta}{2} \frac{R\phi}{2} \Delta R \tag{3.3}$$

where θ and ϕ are the azimuth and elevation beamwidths; R is the distance between the resolution volume and the radar; $\Delta R = c\tau/2$ is the range resolution, c is the speed of light, τ is the pulse width.

In fact, not all of the transmitted power is contained in the 3-dB beamwidths, and real radar antennas do not have such nicely behaved beam patterns. To account for the power distribution in the mainlobe of antenna beams generated by the circular parabolic reflectors used with most meteorological radars, Probert-Jones assumed a Gaussian shape for the beam pattern, and the range resolution volume is corrected with a reduction factor as (Farina, 1992):

$$V = \frac{\pi R^2 \theta \phi c \tau}{8} \cdot \frac{1}{2\ln 2} \tag{3.4}$$

where $2ln2$ is the correction for the Gaussian-shaped beam.

Table 3.1: The operational parameters of the 35 GHz cloud radar in the "fog mode"

Radar Frequency	35 GHz
Transmit Power	200 W (maximun)
Antenna Gain	52 dBi± 1 dB
3-dB Beamwidth	0.34°
Pulse Width	600 ns
Noise Figure	6.3 dB
Minimum Range	250 m
Maximum Range	3353 m
Radar Beam Elevation	3.5°
Antenna Height	5 m

The radar cross sections in the range resolution volume can be written as the sum of the individual radar cross sections in unit volume,

$$\sigma = \sum_{unit\ volume} \sigma_i \cdot V \tag{3.5}$$

where $\eta = \sum_{uint\ volume} \sigma_i$ is the radar reflectivity in unit volume.

Therefore, the radar equation for the beam-filling meteorological targets can be expressed as:

$$P_r = \frac{P_t G^2 \lambda^2 \theta \phi c \tau \sum_{uint\ volume} \sigma_i}{1024 \ln 2 \cdot \pi^2 R^2} \tag{3.6}$$

where G_t is assumed as equivalent to G_r.

Since fog droplets are too small compared to the radar wavelength, the Rayleigh approximation can be apply as:

$$\sigma_i = \frac{\pi^5 |K|^2 D_i^6}{\lambda^4} \tag{3.7}$$

where D_i is the diameter of the ith fog droplet; $K = (m^2 - 1)/(m^2 + 2)$, m is the complex refractive index. Normally, $|K|^2$ is approximated as 0.93 for the liquid water and 0.197 for the ice at centimeter wavelengths and temperatures between 0°C and 20°C.

Substitute Eq. (3.7) into Eq. (3.6), the radar equation is written as:

$$P_r = \frac{\pi^3 P_t G^2 \theta c \tau |K|^2 \sum_{uint\ volume} D_i^6}{1024 \ln 2 \cdot \lambda^2 R^2} \tag{3.8}$$

Radar reflectivity factor is the sum of 6^{th} moment of the diameter over all the droplets in a unit volume, which is expressed as:

$$Z = \sum_{i=1}^{N} D_i^6 \tag{3.9}$$

Substitute Eq. (3.9) into Eq. (3.1), and include the radar system loss l_s in the radar equation,

$$P_r = \frac{\pi^3 P_t G^2 \theta \phi c \tau |K|^2 Z}{1024 \ln 2 \cdot \lambda^2 R^2 l_s} \tag{3.10}$$

It should be noted that the atmospheric losses have to be considered for millimeter-wave radars. Compared to the attenuation by fog droplets, the gaseous attenuation would be very small which is often neglected in the radar equation. In Rayleigh approximation, the attenuation by fog droplets l_a is a linear function of the distance, radar wavelength and liquid water content of fog, which is expressed in linear units as:

$$l_a = e^{2R \cdot \frac{6\pi \cdot LWC}{\rho_w \lambda} \mathrm{Im}(-K)} \tag{3.11}$$

where λ is the radar wavelength in m; LWC is the liquid water content in $g \cdot m^{-3}$; $\rho_w = 10^6\ g \cdot m^{-3}$ is the density of water; K is related to the complex refractive index; the value 2 denotes the two-way attenuation.

To distinguish the radar- and meteorological targets-dependent parameters, the radar equation can be simplified as:

$$P_r = \frac{C|K|^2 Z}{R^2 \cdot e^{2R \cdot \frac{6\pi \cdot LWC}{\rho_w \lambda} \mathrm{Im}(-K)}} \tag{3.12}$$

where $C = \frac{\pi^3 P_t G^2 \theta \phi c \tau}{1024 \ln 2 \lambda^2 l_s}$ is the intrinsic radar constant; Z is the radar reflectivity which depends on the DSD under Rayleigh approximation.

The noise power of radar P_n is given by:

$$P_n = k_B T B \tag{3.13}$$

where k_B is Boltzman's constant, $1.38 \times 10^{-23}\ W/(Hz \cdot K)$; T is the receiver noise temperature in K; B is the receiver noise bandwidth in Hz. For a pulse radar, the receiver filter is always matched to the pulse width as $B \approx 1/\tau$, where τ is the pulse width.

Signal to Noise Ratio (SNR or S/N) is the standard measure of a radar's ability to detect a given target at a given range from the radar, which is defined as the ratio of the received power to the noise power.

The SNR for distributed meteorological targets is expressed as:

$$SNR = \frac{P_r}{P_n} = \frac{C' \tau^2 |K|^2 Z}{R^2 \cdot e^{2R \cdot \frac{6\pi \cdot LWC}{\rho_w \lambda} \mathrm{Im}(-K)} \cdot k_B T} \tag{3.14}$$

where $C' = \frac{\pi^3 P_t G^2 \theta \phi c}{1024 \ln 2 \lambda^2 l_s}$ is the radar constant excluding τ. It can be seen from Eq. (3.14) that the matter of improving the SNR is to increase the τ. The dependence of SNR on τ^2 for distributed targets is different from the point target with the linear dependence on τ ($2E/N_0 = 2P_t \tau / N_0$) (Skolnik, 1970).

Coherent and non-coherent integration techniques are used in the post signal processing to improve the SNR. Typically, the SNR will be improved by a factor of $N_{coh} \cdot$

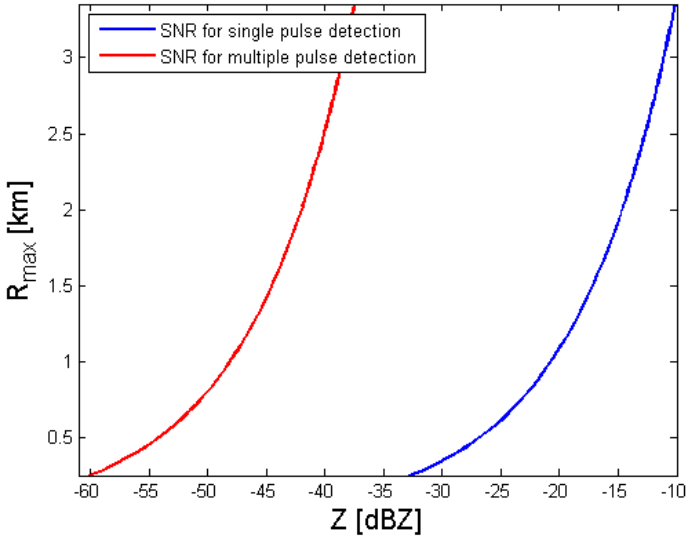

Figure 3.5: Evaluation of the radar sensitivity in fog conditions: the maximum detection range of the radar R_{max} versus the corresponding radar reflectivity Z, where the blue and red lines represent the results of sensitivity calculation for the single and multiple pulse detection respectively.

$\sqrt{N_{non-coh}}$, where N_{coh} and $N_{non-coh}$ are the number of coherent and non-coherent averages respectively (Richards, 2005). The SNR for multiple pulse detection is:

$$SNR^{'} = SNR \cdot N_{coh} \cdot \sqrt{N_{non-coh}} \tag{3.15}$$

where SNR is for single pulse detection in Eq. (3.14).

With the operational parameters provided in Table 3.1, the sensitivity of the 35 GHZ cloud radar is evaluated in fog conditions. In the sensitivity calculation, the radar system loss is set as 7 dB; the fog LWC is assumed as 0.025 $g \cdot m^{-3}$ for all the attenuation correction, which is the average LWC derived from the DSD data at CESAR and it corresponds to a reflectivity value $Z = -46.3$ dBZ; K is calculated based on the single Debye model at $f = 35$ GHz and $T = 5$°C. For the multiple pulse integration, $N_{coh} = 128$ points FFT is used in the coherent spectral analysis, $N_{non-coh} = 18$ is the number of non-coherent averaged spectra.

The maximum detection range of the radar R_{max} is determined at SNR = 0 dB where the received power of the radar is just equal to the noise power. Figure 3.5 shows the R_{max} versus the corresponding radar reflectivity Z, where the blue and red lines represent the results of sensitivity calculation for the single and multiple pulse detection respectively.

It can be seen from Figure 3.5 that the SNR is largely improved by over 27 dB with the multiple pulse detection. At maximum range $R = 3.353$ km, the radar can measure the fog with a reflectivity as low as -37 dBZ. Normally, the fog reflectivity will not exceed -25 dBZ even with visibility less than 100 m, and will not be lower than -60 dBZ with

visibility close to 1 km, which will be shown with the fog cases at CESAR in the following chapters. In turn, the fog with a reflectivity lower than -37 dBZ would not be detectable by the radar beyond the maximum range R = 3.353 km. Therefore, the radar sensitivity needs to be further improved in order to guarantee that most fogs can be detected by the 35 GHz cloud radar at required maximum range.

3.4. Conclusion

This chapter first introduced the fog measurement site in the Netherlands. CESAR has been playing an important role in executing a large scope of research activities in the atmosphere. A fog field campaign was carried out in the season 2011 - 2012, and a number of in situ and remote sensing instruments were actively used in the fog measurements. It is the first time that the 35 GHz cloud radar at CESAR has been used for fog measurements in the Netherlands, though the radar was operated in the "fog mode" for only a couple of days. There were 35 fog cases measured at CESAR, but not all the instruments were simultaneously working on the same days, which has increased the difficulties in probing the fog with limited instruments.

Next, the active in situ and remote sensing instruments deployed in the fog campaign were introduced, especially the 35 GHz cloud radar operated in the "fog mode". A reflector was put above the antenna of the radar, by which the radar beam is deflected from vertical direction to 3.5° elevation. In this way, the radar beam can sufficiently propagate in the fog and probe the fog in detail.

In order to test the detection capability of the radar in fog conditions, the radar sensitivity was evaluated. The maximum detection range of the radar was calculated against the radar reflectivity based on the "fog mode" parameters. The results of sensitivity calculation show that the "fog mode" radar can measure the fog at maximum range R = 3.353 km with the corresponding reflectivity as low as -37 dBZ. However, the radar sensitivity still needs to be further improved with considering the fact that the fog may have even lower reflectivity at required maximum range.

4

Vis, Z parameterization models

4.1. Introduction

Visibility (Vis) and radar reflectivity (Z) are the key parameters to describe the fog intensity. It is typical that dense fogs have low visibility and high reflectivity, and vice versa for light fogs. At CESAR, Vis is measured by the tower-based in situ visibility sensors at 2-, 10-, 20-, 40-, 80-, 140-, and 200-m levels. The Vis at ground has been measured at the AWS (Automated Weather Station) of CESAR since 2007. The Z of water clouds is measured by the vertical pointing cloud radar at 35 GHz, and the vertical velocities and spectral width are also obtained in full Doppler mode. During the fog measurements at CESAR, the radar beam was mirrored by a reflector from vertical direction to 3.5° elevation so that the lower fog layers can be detected by the radar. The fog intensity can be reflected by the Z values, which will not exceed -25 dBZ with visibility less than 100 m, and will not be lower than -60 dBZ with visibility close to 1 km (Hamazu et al., 2003). The terminal velocities of fog droplets are too small to be detected by the radar and they often flow with the winds.

Since Vis and Z are related to the 2^{nd} and 6^{th} moments of DSD, they can be parameterized in terms of other basic integrated quantities such as the number concentration N, the mean and effective radius r_m, r_e, and the liquid water content LWC. In this way, Vis and Z can be retrieved from N, r_m, r_e, LWC or their combinations. In literature, there are a number of empirical Vis and Z parameterizations which are based on limited measurements. The empirical parameterized Vis and Z can be compared with the measured and DSD-derived Vis and Z. On one hand, the accuracies of the Vis, Z parameterizations can be testified from the comparisons (Zhang et al., 2014). On the other hand, the correct operation of the instruments such as the in situ visibility sensors, cloud radar, and FSSP can be verified.

Vis and Z can also be linked via the combinations of various Vis, Z parameterizations. However, the modeling of $Vis-Z$ relations are each based on limited, rather homogeneous measurement conditions, but between them various fog types and evolutionary stages vary. To account for this, the $Vis-Z$ relation can be modeled based on an assumed DSD. Since the Gamma distribution is often used to represent the fog DSD, we can derive a Gamma-based $Vis-Z$ relation. The Gamma-based $Vis-Z$ relation depends on the shape and scale parameters of the Gamma distribution.

In order to compare the various empirical Vis, Z parameterizations and the various $Vis-Z$ relations, the dataset of one fog case from CESAR is used and this is the only one fog case where all the instruments including the in situ visibility sensors, 35 GHz cloud radar, and FSSP were simultaneously working on that day.

This chapter applies the various Vis, Z parameterizations and $Vis-Z$ models to the dataset of one fog case from CESAR. It is structured as follows: Section 4.2 sums up the various empirical Vis, Z parameterizations, and compares them based on the fog case data from CESAR; Section 4.3 follows up with the various $Vis-Z$ relations resulting from the combinations of empirical Vis, Z parameterizations, and a Gamma-based $Vis-Z$ relation is modeled based on an assumed Gamma-shaped DSD. The various $Vis-Z$ relations are also applied to the fog case data from CESAR; Section 4.4 is the conclusion of this chapter.

4.2. Empirical Vis, Z parameterization models

4.2.1. Empirical Vis parameterizations

Since Vis is usually connected with the extinction (Nebuloni, 2005), the relation between LWC and the extinction of fog needs to be first considered. Then the derived relation can be formally converted into the form of $Vis-LWC$ using Koschmieder's visibility law (Koschmieder, 1925).

Eldridge (1966) suggested an empirical relation of the form as:

$$\beta_{ext} = aLWC^b \tag{4.1}$$

where β_{ext} is extinction coefficient in km^{-1}; LWC is in $g \cdot m^{-3}$. The constants a, b are supposed to be determined from the experimental measurements of extinction and LWC.

Eldridge (1966) derived the best-fit parameter values $a = 163$, $b = 0.65$ for "stable and evolving" fogs based on the fog DSD measurements with droplet size ranging from 0.6 - 16 μm diameter. Later, they modified the relation with $a = 91$, $b = 0.65$ by extending the upper limit of the fog DSD measurements (Eldridge, 1971). Pinnick et al. (1979) collected fog DSD data at different heights of fog using a PMS-CSAS (Particle Measurement Systems-Classical Scattering Aerosol Spectrometer) mounted on a tethered balloon and arrived at values $a = 145$, $b = 0.63$. Tomasi and Tampieri (1976), using modified gamma size distribution models derived from empirical size spectra of fog droplets, arrived at the similar relation for two types of fog with different a, b values, where $a = 65$, $b = 2/3$ for "wet and warm" fogs, and $a = 115$, $b = 2/3$ for "dry and cold" fogs.

Considering all of the relationships were derived from either incomplete distributions or limited datasets, Kunkel (1984) re-examined the $\beta_{ext} - LWC$ relation using over 1400 fog droplet spectra measurements from 11 fog cases measured with the AFGL's Weather Test Facility (WTF) at Otis Air National Guard Base, Massachusetts. Taking all the data at 5-m and 30-m levels from each case and correlating them, a mean $\beta_{ext} - LWC$ relation was derived as:

$$\beta_{ext} = 144.7LWC^{0.88} \tag{4.2}$$

where β_{ext} is extinction coefficient in km^{-1}; LWC is in $g \cdot m^{-3}$. Kunkel's $\beta_{ext} - LWC$ relation in Eq. (4.2) has been applied in many fog microphysical parameterizations for numerical weather prediction (NWP) models (Gultepe et al., 2006b).

Various empirical $Vis-LWC$ relations can be derived from the $\beta_{ext} - LWC$ relations using Koschmieder's visibility law. In such a way, Gultepe et al. (2006b) arrived at a $Vis-$

LWC relation which results from Kunkel's $\beta_{ext} - LWC$ relation,

$$Vis = 0.027 LWC^{-0.88} \tag{4.3}$$

where Vis is in km; LWC is in $g \cdot m^{-3}$. Kunkel & Gultepe's $Vis - LWC$ relation is commonly used for Vis parameterization in many operational forecast models.

Early studies also suggested that Vis is indirectly related to droplet number concentration N. Meyer et al. (1980) showed that Vis is a function of N and it varies with fog intensity, which is given by:

$$Vis = aN^b \tag{4.4}$$

where Vis is in km; N is in cm^{-3}. $a = 120$, $b = -0.77$ for light fogs, and $a = 80$, $b = -1.1$ for heavy fogs. Light fogs were defined as Vis less than 1 km, and dense fogs were defined as Vis between 1 - 5 km.

Gultepe et al. (2006b) derived a similar relation with $a = 44.989$, $b = -1.1592$ using the DSD measurements. The variations in a, b indicate that Vis is not a function of N only, and more parameters should be involved to improve the accuracy of Vis parameterization.

The early studies on $LWC - N$ relations showed that there is usually a large variability on N for a given LWC (Gultepe et al., 1996; Gultepe and Isaac, 2004). Gultepe et al. (2006b) also found that N can vary from a few droplets per volume to several hundred for a fixed LWC, which suggests that Vis should be a function of both LWC and N. In fact, increasing LWC or N will lead to the decrease of Vis. Using the fog DSD measurements from the FSSP during the RACE (Radiation and Aerosol Cloud Experiment) project, Gultepe et al. (2006b) derived a best-fit $Vis - LWC - N$ relation,

$$Vis = \frac{1.002}{(LWC \cdot N)^{0.6473}} \tag{4.5}$$

where Vis is in km; LWC is in $g \cdot m^{-3}$; N is in cm^{-3}. The Vis parameterization in Eq. (4.5) has been proved to improve the Vis accuracy up to 50% in forecast models.

Moreover, effective radius r_e is a weighted mean of the size distribution of droplets, which is defined as the ratio of the 3^{rd} to the 2^{nd} moment of DSD.

$$r_e = \frac{\int_0^\infty n(r) r^3 dr}{\int_0^\infty n(r) r^2 dr} \tag{4.6}$$

By definition, LWC and Vis are related to the 3^{rd} and 2^{nd} moments of DSD, and therefore the numerator and denominator in Eq. (4.6) can be replaced with LWC and Vis respectively. In this way, a theoretical $Vis - LWC - r_e$ relation can be deduced as:

$$Vis = \frac{-2\ln(0.05) \cdot r_e}{3 \cdot LWC} \cdot 10^{-3} \tag{4.7}$$

where Vis is in km; LWC is in $g \cdot m^{-3}$; r_e is in μm.

4.2.2. Empirical Z parameterizations

Since Z and LWC are functions of the 6th and 3rd moments of DSD, in principle, it is possible to link Z to LWC, and to derive Z from LWC. Early studies derived $Z-LWC$ relations from DSD measurements, though droplet spectra are usually incomplete or limited. Atlas (1954) proposed a $Z-LWC$ relation in clouds in the form of

$$Z = aLWC^b \tag{4.8}$$

where $a = 0.048$, $b = 2$. Z is in mm^6/m^3; LWC is in $g \cdot m^{-3}$.

Later on, Sauvageot and Omar (1987) found a similar relation in cumulus and stratocumulus clouds with $a = 0.03$, $b = 1.31$ based on the DSD measurements from airborne particle probes. Their $Z-LWC$ relation is only valid up to a reflectivity of -15 dBZ, above which drizzle will be present and may dominate the radar reflectivity. Fox and Illingworth (1997) derived a similar relation in stratocumulus clouds with $a = 0.012$, $b = 1.16$ based on the DSD measurements, which was not fully represented by the Gamma distribution in consideration of the coexistence of drizzle in clouds.

The different values of a, b are due to the variations of droplet spectra. It is not easy to establish a unique relationship between Z and LWC, since the DSD cannot be accurately parameterized without additional information about the specific regimes within the clouds/fogs. Different fog types or evolutionary stages of fog would have different relationships between Z and LWC.

However, the $Z-LWC$ relation can still be simulated with an assumed DSD. Maier et al. (2012) deduced a $Z-LWC$ relation in natural fogs assuming a prognostic modified Gamma distribution, which is given by:

$$Z = \frac{3}{4\pi\rho_w}\frac{\Gamma(\frac{\alpha+7}{\gamma})}{\Gamma(\frac{\alpha+4}{\gamma})}b^{-\frac{3}{\gamma}} \times 10^6 \cdot LWC \tag{4.9}$$

where Z is in mm^6/m^3; LWC is in $g \cdot m^{-3}$; $\rho_w = 10^6\ g \cdot m^{-3}$ is the water density. The modified Gamma distribution is parameterized as $n(r) = ar^\alpha \exp(-br^\gamma)$, a is an integer and the intercept of the distribution, α, b, γ are the parameters controlling the shape and slope of the distribution. This $Z-LWC$ relation strongly depends on the DSD which is hardly known for natural fog types. Furthermore, the sensitivity of the influence of DSD parameters on the $Z-LWC$ relation has to be considered for different fog types and evolutionary stages of fog.

In analogy with the Vis parameterization, Z should not be a function of LWC only. Using the DSD measurements of a marine fog event during the FRAM project, Gultepe et al. (2009) derived an empirical $Z-LWC-r_e$ relation as:

$$Z = -176.7314 \cdot (LWC \cdot r_e^2)^{-0.026344} + 135.6197 \tag{4.10}$$

where Z is in dBZ; LWC is in $g \cdot m^{-3}$; r_e is in μm.

4.2.3. Comparison of various Vis, Z parameterizations

In this part, various Vis and Z parameterizations are compared based on the dataset of one fog case that was collected by the in situ and remote sensing instruments synergy at

CESAR. The fog event occurred during February 17-18, 2012 which originated from low stratus clouds consistently lowering to the ground. Visibility first reduced below 1 km at 22:20:00 UTC 17-02-2012 until 03:43:00 UTC 18-02-2012 when the clouds lifted and visibility increased to 1 km. All the instruments including the 35 GHz cloud radar, in situ visibility sensors, and FSSP were simultaneously operated for fog measurements during this period.

Figure 4.1 plots the temporal evolution of Vis during fog episodes on February 17-18, 2012. Vis was measured by the tower-based in situ visibility sensors at 2-, 10-, 20-, 40-, 80-, 140-, and 200-m levels. Fog DSD was measured by the FSSP mounted at 60-m level of the CESAR tower. In order to reduce the sampling deviations at different levels, the Vis measured by the 40-m visibility sensor is compared with the DSD-derived Vis at 60 m, and they coincide well during fog episodes, which is shown in Figure 4.1. The red line represents the Vis measured by the 40-m visibility sensor, and the blue line represents the Vis derived from the DSD measurements of the FSSP. Their fairly good match indicates that the in situ visibility sensor and the FSSP were operated well and that the fog droplets are small enough to be considered in the Rayleigh region. However, we can also see that the measured Vis (red line) began to increase faster than the DSD-derived Vis (blue line) at 02:07:00 UTC 02-18-2012, which is due to the fact that the lifting clouds first passed through the visibility sensor at 40 m and then passed through the 60-m level FSSP in the dissipation stage of fog.

Meanwhile, the empirical Vis parameterizations in terms of LWC, N are also plotted in Figure 4.1 based on the same measurement data, where LWC, N are derived from the DSD. It can be seen from Figure 4.1 that Gultepe's Vis parameterization in Eq. (4.5), which is represented by the green line, fits better to the Vis measurements than Kunkel & Gultepe's Vis parameterization in Eq. (4.3) represented by the black line. In theory, Vis and LWC are related to the 2nd and 3rd moments of DSD, and N is the total droplet concentration in unit volume. Therefore, involving N in the Vis parameterization can increase the accuracy of Vis estimate, which is shown by Gultepe's Vis parameterization in Figure 4.1.

Analogically, the temporal evolution of Z during fog episodes on February 17-18, 2012 is plotted in Figure 4.2. In order to derive $Vis-Z$ relation from the measurement data, we have to use the Vis and Z measured at close height. Therefore, the Z in the 8th range gate (about 40 m in height) measured by the 35 GHz cloud radar is compared with the DSD-derived Z at 60 m, and they coincide well during fog episodes. The red line represents the measured Z in the vicinity of 40 m level, and the blue line represents the DSD-derived Z. Their fairly good match indicates that the radar was calibrated properly for the fog measurements. As fog droplets have a very small backscatter cross section, sometimes they might not be detected by the radar, and some of them are "lost" due to the cloud-masking processing of the radar, so the measured Z are not continuous as shown by the red line in Figure 4.2. Due to the limitation of radar sensitivity, the measured Z can only get to as low as about -48 dBZ which is higher than most of the DSD-derived Z. In addition, FSSP can only measure the fog droplets over the size range from 3 - 46.5 μm in diameter, however the fact is there are many fog droplets distributed below 3 μm that cannot be measured but might play an important role in the Vis reduction and Z increase (Elias et al., 2009). This results in the phenomenon that the DSD-derived

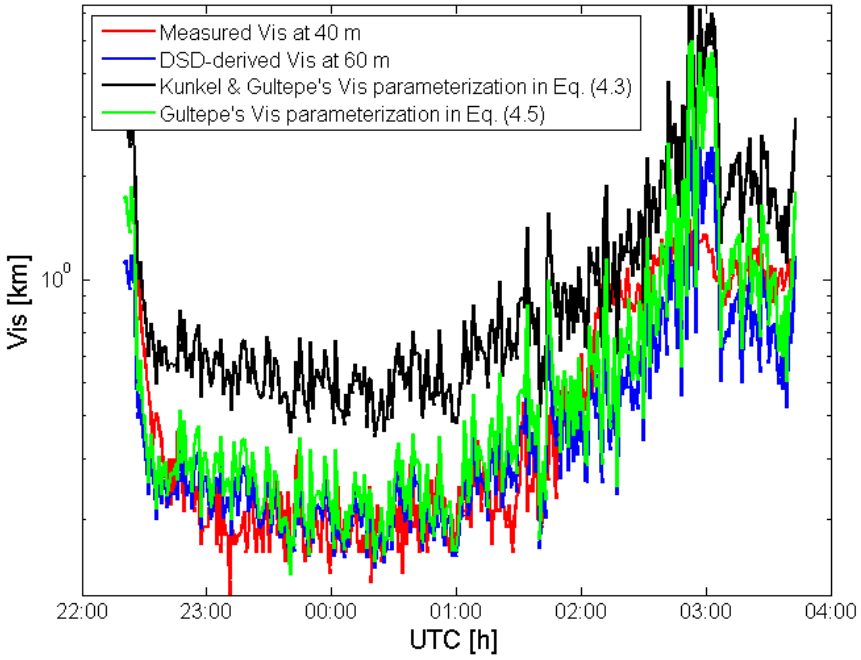

Figure 4.1: Temporal evolution of Vis during fog episodes on February 17-18, 2012. The measured Vis at 40 m (red) coincides well with the DSD-derived Vis at 60 m (blue). Gultepe's Vis parameterization $Vis = 1.002/(LWC \cdot N)^{0.6473}$ (green) fits better to the Vis measurements than Kunkel & Gultepe's $Vis = 0.027 LWC^{-0.88}$ (black).

Vis is always higher than the measured Vis while the DSD-derived Z is lower than the measured Z, which is shown in Figure 4.1 and Figure 4.2.

The empirical Z parameterizations in terms of LWC, r_e are also plotted in Figure 4.2 based on the same measurement data, where LWC, r_e are derived from the DSD. It can be seen from Figure 4.2 that Atlas's Z parameterization in Eq. (4.8) with $a = 0.048$, $b = 2$ and Gultepe's Z parameterization in Eq. (4.10), which are represented by the green and cyan line, fit better to the Z measurements than Sauvageot & Omar's and Fox & Illingworth's Z parameterizations which are represented by the black and magenta line. In theory, Z and LWC are related to the 6^{th} and 3^{rd} moments of DSD, and therefore the second power of LWC would better parametrize the Z, which conforms to Atlas's Z parameterization. Furthermore, involving r_e in the Z parameterization can increase the accuracy of Z estimate, which is shown by Gultepe's Z parameterization in Figure 4.2.

4.3. Modeling of Vis-Z relation

Various empirical $Vis-Z$ relations can be derived by combining the $Vis-LWC$ relations with the $Z-LWC$ relations above. Kunkel & Gultepe's $Vis-LWC$ relation is combined

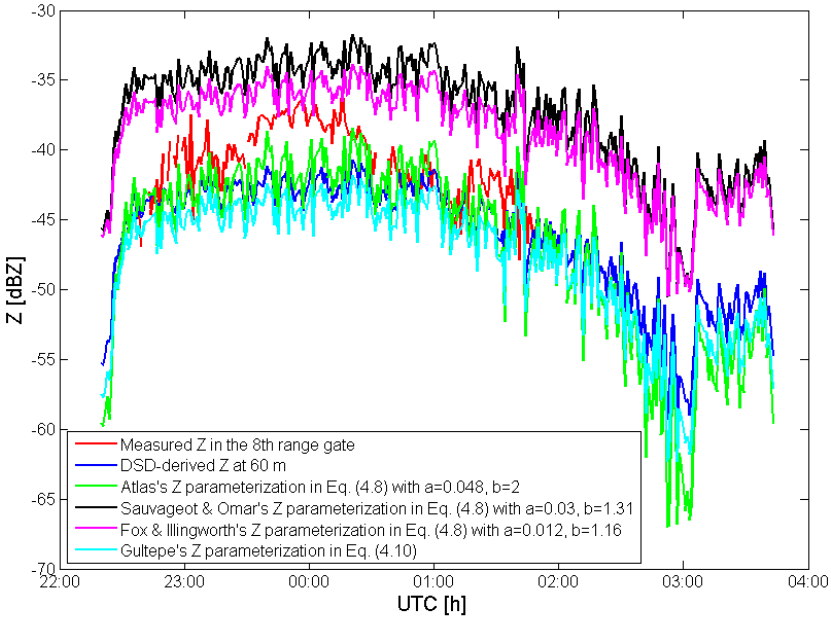

Figure 4.2: Temporal evolution of Z during fog episodes on February 17-18, 2012. The measured Z in the 8^{th} range gate (red) coincides well with the DSD-derived Z at 60 m (blue). Atlas's Z parameterization $Z = 0.048LWC^2$ (green) and Gultepe's Z parameterization $Z = -176.7314 \cdot (LWC \cdot r_e^2)^{-0.026344} + 135.6197$ (cyan) fit better to the Z measurements than Sauvageot & Omar's $Z = 0.03LWC^{1.31}$ and Fox & Illingworth's $Z = 0.012LWC^{1.16}$ (magenta). It should be noted that some of the measured Z are "lost" due to the cloud-masking processing of the radar, so the measured Z are not continuous as shown by the red line.

with Atlas's, Sauvageot & Omar's, Fox & Illingworth's $Z - LWC$ relations respectively, removing LWC in each combination,

$$Vis = 0.0071Z^{-0.44} \tag{4.11}$$

$$Vis = 0.0026Z^{-0.6718} \tag{4.12}$$

$$Vis = 9.423 \cdot 10^{-4} Z^{-0.7586} \tag{4.13}$$

where Vis is in km; Z is in mm^6/m^3.

Various empirical $Vis - Z - N$ relations are derived by combining Gultepe's $Vis - LWC - N$ relation with Atlas's, Sauvageot & Omar's, Fox & Illingworth's $Z - LWC$ relations respectively, and removing LWC in each combination,

$$Vis = \frac{0.375}{Z^{0.3265} N^{0.6473}} \tag{4.14}$$

$$Vis = \frac{0.1772}{Z^{0.4941} N^{0.6473}} \tag{4.15}$$

Table 4.1: Derivation of various Vis-Z and Vis-Z-N relations by combining Vis-LWC and Vis-LWC-N relations (top row) with Z-LWC relations respectively (left column)

Z \ Vis	$Vis = 0.027 LWC^{-0.88}$ (Kunkel & Gultepe)	$Vis = \frac{1.002}{(LWC \cdot N)^{0.6473}}$ (Gultepe)
$Z = 0.048 LWC^{2}$ (Atlas)	$Vis = 0.0071 Z^{-0.44}$ (magenta solid line)	$Vis = \frac{0.375}{Z^{0.32365} N^{0.6473}}$ (magenta dash line)
$Z = 0.03 LWC^{1.31}$ (Sauvageot & Omar)	$Vis = 0.0026 Z^{-0.6718}$ (cyan solid line)	$Vis = \frac{0.1772}{Z^{0.4941} N^{0.6473}}$ (cyan dash line)
$Z = 0.012 LWC^{1.16}$ (Fox & Illingworth)	$Vis = 9.423 \cdot 10^{-4} Z^{-0.7586}$ (green solid line)	$Vis = \frac{0.0849}{Z^{0.558} N^{0.6473}}$ (green dash line)

$$Vis = \frac{0.0849}{Z^{0.558} N^{0.6473}} \tag{4.16}$$

where Vis is in km; Z is in mm^6/m^3; N is in cm^{-3}.

The empirical $Vis-Z$ and $Vis-Z-N$ relations above are applied to the measurement data during the fog event on February 17-18, 2012, which is show in Figure 4.3. It should be noted that the Z in the $Vis-Z$ and $Vis-Z-N$ relations have a large range of linear values, which is therefore expressed in units of dBZ in figures for compactness. In Figure 4.3, the red dots denote Vis measured by the 40-m visibility sensor versus Z measured by the radar, and the blue dots denote Vis versus Z both derived from the measured DSD. The magenta, cyan, green solid lines represent the derived empirical $Vis-Z$ relations in Eq. (4.11) - Eq. (4.13), and the magenta, cyan, green dash lines represent the derived empirical relations in Eq. (4.14) - Eq. (4.16) with a constant $N = 200 \cdot cm^{-3}$ which is the average number concentration during the fog period acquired from the FSSP. It can be seen from Figure 4.3 that the magenta dash line, representing the combination of Gultepe's Vis and Atlas's Z parameterizations, achieves the best fitting results to the measurement data, because Gultepe's Vis and Atlas's Z parameterizations have closer approximation to the Vis and Z measurements than the others' as shown in Figure 4.1 and Figure 4.2. The various empirical $Vis-Z$ and $Vis-Z-N$ relations in Eq. (4.11) - Eq. (4.16) are listed in Table 4.1.

However, the modeling of $Vis-Z$ and $Vis-Z-N$ relations above are each based on limited, rather homogeneous measurement conditions, but between them various fog types and evolutionary stages vary. To account for this, the $Vis-Z$ relation can be modeled based on an assumed DSD, since Vis and Z are related to the 2nd and 6th moments

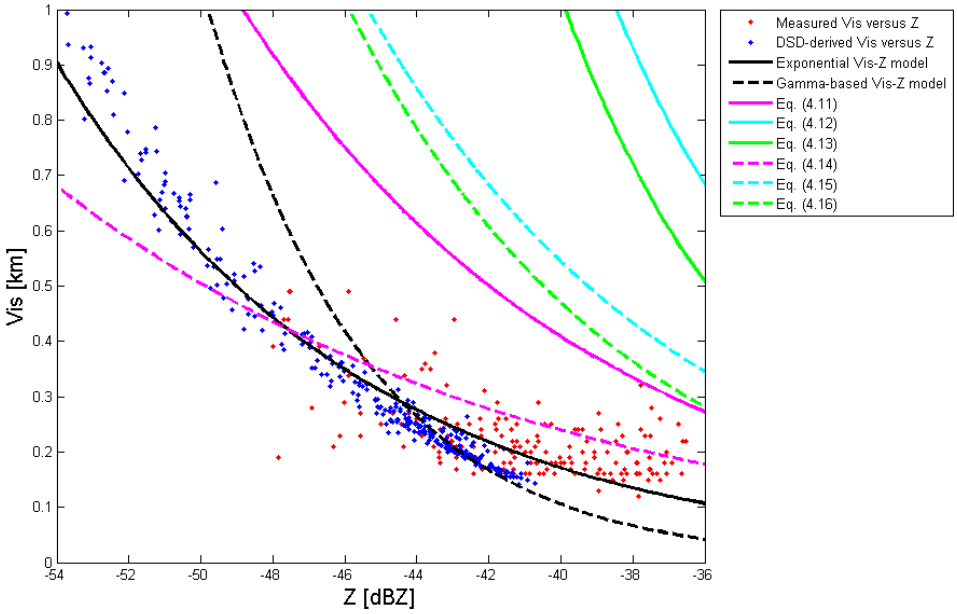

Figure 4.3: Comparison of various $Vis-Z$ and $Vis-Z-N$ relations based on the measurement data during the fog event on February 17-18, 2012. The red dots denote Vis measured by the 40-m visibility sensor versus Z measured by the radar, and the blue dots denote Vis versus Z both derived from the measured DSD. The magenta, cyan, green solid lines represent the empirical $Vis-Z$ relations in Eq. (4.11) - Eq. (4.13) by combining Kunkel & Gultepe's $Vis-LWC$ relation with Atlas's, Sauvageot & Omar's, Fox & Illingworth's $Z-LWC$ relations respectively, and the magenta, cyan, green dash lines represent the empirical $Vis-Z-N$ relations in Eq. (4.14) - Eq. (4.16) by combining Gultepe's $Vis-LWC-N$ relation with Atlas's, Sauvageot & Omar's, Fox & Illingworth's $Z-LWC$ relations respectively with a constant $N=200\ cm^{-3}$. The black dash line represents the Gamma-based $Vis-Z$ model $Vis\cdot Z=-64\ln\varepsilon/2\pi\cdot R_n^4\cdot\Gamma(\upsilon+6)/\Gamma(\upsilon+2)\cdot 10^{-9}$ best-fitting to the measurements with the best-fit parameter values $\upsilon=2$, $R_n=0.8$, and the black solid line represents the exponential $Vis-Z$ model best-fitting to the measurements with the best-fit parameter values $a=0.0015$, $b=-0.5157$.

of DSD. The Gamma distribution is often used to represent the fog DSD as (Tampieri and Tomasi, 1976):

$$n(r)=\frac{N}{R_n^{\upsilon}\cdot\Gamma(\upsilon)}\cdot r^{\upsilon-1}\cdot e^{-\frac{r}{R_n}},\ r\geq 0 \tag{4.17}$$

where N is the total number concentration; $\Gamma(\upsilon)$ is the Gamma function; υ and R_n are the shape and scale parameters of the Gamma distribution.

Substituting Eq. (4.17) into the Vis, Z definition formulas and combining, a Gamma-based $Vis-Z$ relation can be modeled as:

$$Vis\cdot Z=\frac{-64\ln\epsilon}{2\pi}\cdot R_n^4\cdot\frac{\Gamma(\upsilon+6)}{\Gamma(\upsilon+2)}\cdot 10^{-9} \tag{4.18}$$

where ϵ is the threshold of contrast with human eyes and normally sets to 0.05; Vis is

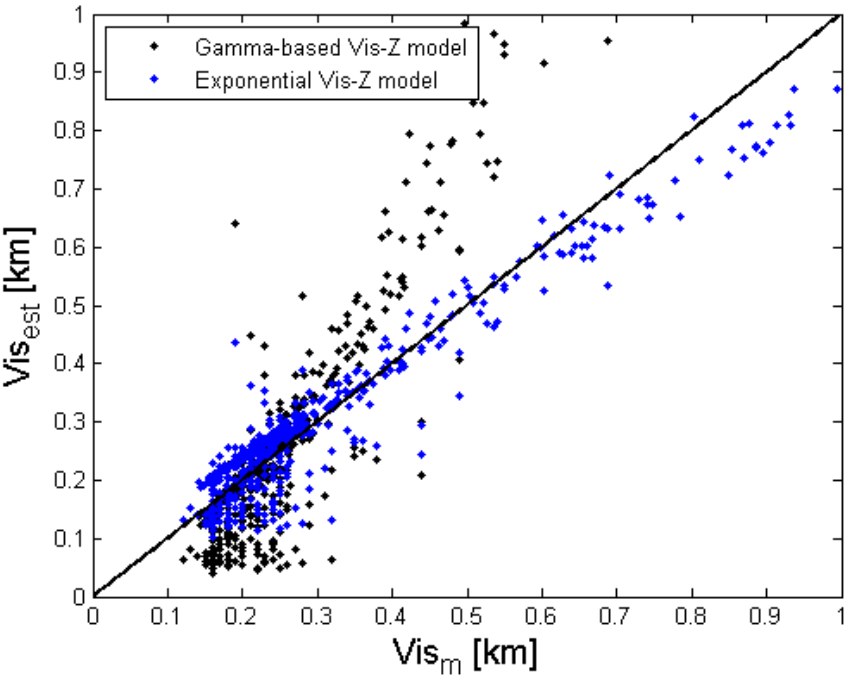

Figure 4.4: The estimated from the Gamma-based $Vis-Z$ model (black dots) and the exponential $Vis-Z$ model (blue dots) are plotted against the Vis measurements during the fog event on February 17-18, 2012, where the measured Vis, Z and the DSD-derived Vis, Z are simultaneously used in both models.

in km; Z is in mm^6/m^3. As shown in Eq. (4.18), the Gamma-based $Vis-Z$ model is dependent on the shape and scale parameters of the Gamma distribution υ and R_n.

The Gamma-based $Vis-Z$ model is also applied to the measurement data during the fog event on February 17-18, 2012. Using the least squares method, the best-fit parameter values in Eq. (4.18) can be estimated as $\upsilon = 2$, $R_n = 0.8$, which is plotted as the black dash line in Figure 4.3. It is shown that the Gamma-based $Vis-Z$ model fits not well with the measurements due to the limitation of the Gamma distribution.

An exponential $Vis-Z$ model can be deduced by using the regression analysis to the measurement data, which is shown as the black solid line in Figure 4.3,

$$Vis = a \cdot Z^b \tag{4.19}$$

where Vis is in km; Z is in mm^6/m^3. $a = 0.0015$, $b = -0.5157$ are the best-fit parameter values which are estimated from the measurement data during the fog event on February 17-18, 2012.

It is shown in Figure 4.3 that the exponential $Vis-Z$ model as in Eq. (4.19) with $a = 0.0015$, $b = -0.5157$ fits better to the measurements than the other models for the fog event on February 17-18, 2012, though a, b will vary for different fog events.

The empirical $Vis-Z-N$ relation in Eq. (4.14) is derived by combining individual and limited measurements which were taken in different conditions, so we only compare the Gamma-based $Vis-Z$ model and the exponential $Vis-Z$ model in terms of the estimated accuracy of Vis. In Figure 4.4 the Vis estimated from these two models are plotted against the Vis measurements during the fog event on February 17-18, 2012, where the measured Vis, Z and the DSD-derived Vis, Z are simultaneously used in both models. The Vis estimates are based on available Z measurements. It is shown in Figure 4.4 that the Vis estimated from the exponential $Vis-Z$ model is much closer to the Vis measurements than that estimated from the Gamma-based $Vis-Z$ model, which indicates that the exponential $Vis-Z$ model results in a higher accuracy of Vis estimate than the Gamma-based $Vis-Z$ model.

It can be seen from Figure 4.4 that although the exponential $Vis-Z$ model can better estimate Vis from Z measurements than the Gamma-based $Vis-Z$ model, the estimate errors are still large because of the instability of the model using single parameter for estimation. By referring to the Vis and Z parameterizations in terms of N, r_m, r_e, LWC or their combinations, the estimated accuracy of Vis in the $Vis-Z$ models should also be improved with more microphysical parameters such as N or LWC adding into the current models. Based on this, we are able to develop a new Vis estimate model and it will compare with the Gamma-based $Vis-Z$ model and the exponential $Vis-Z$ model based on various types of datasets, which will be elaborated in the following chapter.

4.4. Conclusion

This chapter indicated Vis and Z as the key parameters to describe the fog intensity. Various empirical Vis, Z parameterizations in terms of N, r_m, r_e, LWC or their combinations were first summed up, then the parameterized Vis, Z were compared with the measured and DSD-derived Vis, Z based on the dataset of a stratus-lowering fog case from CESAR. This is the only one fog case where all the instruments including the in situ visibility sensors, 35 GHz cloud radar, and FSSP were simultaneously working on that day. Although there is inevitable spatial variability between the in situ visibility sensors and FSSP, the Vis measured by the 40-m visibility sensor agreed fairly well with the DSD-derived Vis at 60 m, which indicates the correct operation of the instruments and the applicability of Rayleigh scattering regime for the fog droplets. Identically, the good agreement of the Z in the 8^{th} range gate (40 m in height) measured by the 35 GHz cloud radar with the DSD-derived Z at 60 m indicates that the radar was calibrated well for the fog measurements. Meanwhile, it has been verified that Gultepe's $Vis-LWC-N$ relation results in a higher accuracy of Vis estimate than Kunkel & Gultepe's $Vis-LWC$ relation which parametrized Vis in terms of LWC only, and Atlas's $Z-LWC$ relation and Gultepe's $Z-LWC-r_e$ relation result in better Z estimates.

Various $Vis-Z$ and $Vis-Z-N$ relations can be derived by combining the various Vis and Z parameterizations. The derived $Vis-Z$ and $Vis-Z-N$ relations were applied to the same dataset as in the Vis and Z parameterizations. Meanwhile, a Gamma-based $Vis-Z$ model was derived based on an assumed Gamma-shaped DSD. An exponential $Vis-Z$ model was deduced by using the regression analysis to the dataset. All the $Vis-Z$ models were plotted in the same figure, and it has been shown that the exponential $Vis-Z$ model $Vis=a\cdot Z^b$ with the best-fit parameter values $a=0.0015$, $b=-0.5157$ fits

better to the measurements than the other models for the fog event on February 17-18, 2012. It should be noted that a, b will vary for different fog events.

In the end, we pointed out that a new Vis estimate model can be developed with more microphysical parameters such as N or LWC adding into the current exponential $Vis-Z$ model. The new Vis estimate model will compare with the Gamma-based $Vis-Z$ model and the exponential $Vis-Z$ model based on various types of datasets, which will be discussed in detail in the following chapter.

5

A novel radar-based visibility estimator

5.1. Introduction

As indicated in chapter 4, the exponential $Vis-Z$ model $Vis = a \cdot Z^b$ can result in a higher accuracy of Vis estimate than the other models, though a, b are not uniform for various fog cases. However, the estimate errors are still large because of the instability of the exponential $Vis-Z$ model using only Z for Vis estimate. By referring to the Vis and Z parameterizations in terms of N, r_e, LWC or their combinations, Gultepe's $Vis-LWC-N$ relation can derive better Vis estimates than the $Vis-LWC$ relation, and Gultepe's $Z-LWC-r_e$ relation can derive better Z estimates than the simple $Z-LWC$ relation. Therefore, the estimated accuracy of Vis can be improved by adding more microphysical parameters such as N, LWC or r_e into the exponential $Vis-Z$ model. Meanwhile, it should be noted that the complexity of the model will be also increased with more parameters involved.

Since both Vis and Z can be parameterized in terms of LWC, a further development of the exponential $Vis-Z$ can be investigated with the inclusion of LWC. As LWC is proportional to the attenuation factor of radar L_a at a given frequency, it can be substituted by the L_a in the new Vis estimator model. In this way, the new $Vis-Z-L_a$ model can estimate Vis from radar reflection and attenuation only.

In order to test the robust performance of the new $Vis-Z-L_a$ model, various types of datasets are used. The datasets are partly from literature and partly from CESAR. Meanwhile, the new $Vis-Z-L_a$ model is compared with the Gamma-based $Vis-Z$ model and the exponential $Vis-Z$ model based on the datasets. The goodness of fit for the three models are summarized.

This chapter introduces a new Vis estimator model and validates it with various types of datasets. It is structured as follows: Section 5.2 describes the new estimator model $Vis = f(Z, L_a)$; Section 5.3 validates the high accuracy of Vis estimate in the model with simulated DSD in literature and measured DSD from CESAR; Section 5.4 validates the model with measured Vis, Z and DSD from the in situ visibility sensor, 35 GHz cloud radar, and FSSP at CESAR; Section 5.5 is the conclusion of this chapter.

5.2. A robust Vis estimator model

Both Vis and Z can be derived from LWC in terms of the various $Vis-LWC$ and $Z-LWC$ relations, but either Vis or Z is not only a function of LWC, which has been shown in Figure 4.1 and Figure 4.2. Clearly, a more precise Vis estimator model needs more terms, not only LWC or only Z, but a combination. Therefore, a further development of

the exponential $Vis - Z$ model is investigated with the inclusion of LWC,

$$Vis = c \cdot LWC^a \cdot Z^b \tag{5.1}$$

where Vis is in km; Z is in mm^6/m^3; LWC is in $g \cdot m^{-3}$.

The attenuation factor of radar L_a is related to the 3rd moment of DSD and in Rayleigh scattering regime it is proportional to the LWC at a given radar frequency, which is expressed as (Doviak and Zrnic, 2014):

$$L_a = 2 \cdot 0.4343 \cdot \frac{6\pi \cdot LWC}{\lambda} \mathrm{Im}(-K) \tag{5.2}$$

where L_a is the attenuation factor in dB/km; λ is the radar wavelength in cm; K is the parameter related to the complex index of refraction; the value 2 denotes the two-way attenuation.

The LWC in Eq. (5.1) can be replaced with the L_a. This introduces a radar measurement parameter directly into the microphysical Vis relation.

$$Vis = C \cdot L_a^a \cdot Z^b \tag{5.3}$$

where $L_a = d \cdot LWC$ in dB/km is denoted as the attenuation factor in unit resolution volume of radar, $d = 2 \cdot 0.4343 \cdot \frac{6\pi}{\lambda} \mathrm{Im}(-K)$ is a constant at a given radar wavelength λ, $C = c/d^a$; Vis is in km; Z is in mm^6/m^3.

5.3. Model validation with simulated DSD and measured DSD at CESAR

5.3.1. Generation of simulated DSD

In order to test the robust performance of the exponential $Vis - Z - L_a$ model, a large group of DSD datasets for various fog types and evolutionary stages of fog are used. Tomasi and Tampieri (1976) have summarized the parameter sets of modified Gamma size distribution of fog droplets for different types and various evolutionary stages of fog. Based on a general form of the modified Gamma size distribution $n(r) = ar^\alpha \exp\left[-\frac{\alpha}{\gamma}\left(\frac{r}{r_c}\right)^\gamma\right]$, $0 \le r < \infty$, all the a, α, γ, r_c values are listed for 4 main fog types (radiation fog, evaporation fog, advection fog, arctic marine advection fog) and 4 evolutionary stages of fog (ground fog, formation stage, mature fog, dissipation fog). r_c is the mode radius indicating the radius of maximum frequency. The three parameters α, γ and r_c fully determine the shape of the distribution, and a is the total concentration of droplets per unit volume. Given the parameter sets, the DSD datasets can be simulated in this way:

1. For each type of fog and each stage of fog, visibility is set in a couple of levels: 10, 20, 50, 100, 200, 500 and 1000 m;
2. Using the given parameter sets, for each visibility level the number concentration can be calculated within each size bin of an assumed size range (0.5 - 49.5 μm in radii with each size bin 1 μm for the simulation);
3. Vis, Z, L_a can be calculated from the simulated DSD datasets.

Table 5.1: Goodness of fit for the Gamma-based $Vis-Z$ mode, the exponential $Vis-Z$ model, and the exponential $Vis-Z-L_a$ model based on the simulated DSD datasets

(SSE: Sum of Squares due to Error, denotes the total deviations of the estimated values from the measured values; R-Square, is the ratio of the sum of squares of the regression (SSR) and the total sum of squares (SST), which measures how successful the fit is in explaining the variation of the data; Adjusted R-Square, is the R-Square adjusted based on the residual degrees of freedom; RMSE: Root Mean Squared Error, is an estimate of the standard deviation of the random component in the data.)

Goodness of fit / Model	SSE	R-Square	Adjusted R-Square	RMSE
Gamma-based Vis-Z model	29.13	0.2927	0.2993	0.3875
Exponential Vis-Z model	14.93	0.3374	0.3334	0.2774
Exponential Vis-Z-La model	0.2842	0.9968	0.9968	0.03837

5.3.2. Model validation with simulated DSD

Thereupon we can compare the Gamma-based $Vis-Z$ model, the exponential $Vis-Z$ model and the exponential $Vis-Z-L_a$ model based on the simulated DSD datasets. Using the least squares method, the best-fit parameter values in the three models can be estimated. For the Gamma-based $Vis-Z$ model $Vis\cdot Z=\frac{-64\ln\epsilon}{2\pi}\cdot R_n^4\cdot\frac{\Gamma(\upsilon+6)}{\Gamma(\upsilon+2)}\cdot 10^{-9}$, the values are: $\upsilon=2$, $R_n=1.1$; for the exponential $Vis-Z$ model $Vis=a\cdot Z^b$, the values are: $a=0.0078$, $b=-0.4956$; and for the exponential $Vis-Z-L_a$ model $Vis=C\cdot L_a^a\cdot Z^b$, the values are: $a=-1.366$, $b=0.3695$, $C=0.1826$. Table 6.1 lists the goodness of fit for the three models, where SSE is the Sum of Squares due to Error, which denotes the total deviations of the estimated values from the measured values; R-Square is the ratio of the sum of squares of the regression (SSR) and the total sum of squares (SST), which measures how successful the fit is in explaining the variation of the data; Adjusted R-Square is the R-Square adjusted based on the residual degrees of freedom; RMSE is the Root Mean Squared Error, which is an estimate of the standard deviation of the random component in the data. The goodness-of-fit statistics are illustrated in Appendix B.

Figure 5.1 shows the comparison between the DSD-derived Vis and the Vis estimated from the Gamma-based $Vis-Z$ model, the exponential $Vis-Z$ model, and the exponential $Vis-Z-L_a$ model based on the simulated DSD datasets, where Vis, Z, L_a in the three models are all calculated from the simulated DSD. It is shown in Figure 5.1 that the Vis estimated from the exponential $Vis-Z-L_a$ model is much closer to the DSD-derived Vis than those estimated from the other two models. Meanwhile, in Table 5.1 the SSE and RMSE of the exponential $Vis-Z-L_a$ model are far smaller than those of the other two models, indicating that the exponential $Vis-Z-L_a$ model has a

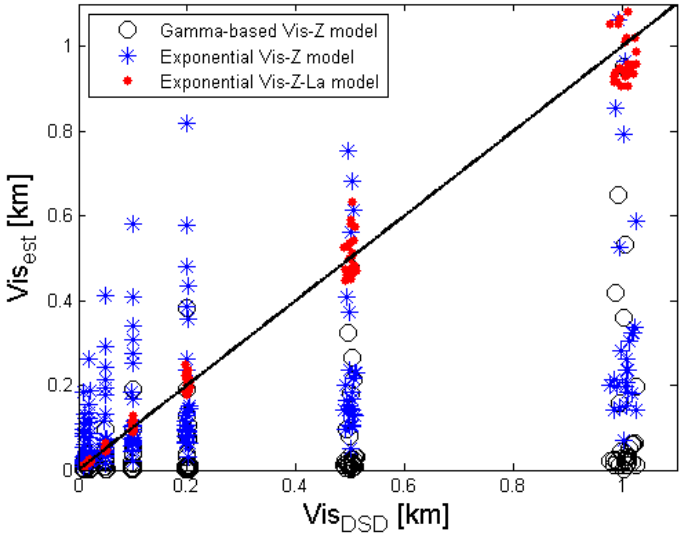

Figure 5.1: Comparison between the DSD-derived Vis and the Vis estimated from the Gamma-based $Vis-Z$ model (black circles), the exponential $Vis-Z$ model (blue asterisks), and the exponential $Vis-Z-L_a$ model (red dots) based on the simulated DSD datasets, where Vis, Z, L_a in the three models are all calculated from the simulated DSD.

smaller random error component, and it will arrive at a higher accuracy of estimate. The R-Square and Adjusted R-Square of the exponential $Vis-Z-L_a$ model are very close to 1, much larger than those of the other two models, indicating that a greater proportion of the variance can be accounted for by the exponential $Vis-Z-L_a$ model. Based on these results, we can conclude that the exponential $Vis-Z-L_a$ model can estimate Vis from DSD-derived Z, L_a with a much higher accuracy than the Gamma-based $Vis-Z$ model and the exponential $Vis-Z$ model.

5.3.3. Model validation with measured DSD at CESAR

In addition, the exponential $Vis-Z-L_a$ model can be also validated with the DSD datasets that were collected by the FSSP at CESAR. In the fog field campaign carried out at CESAR during December 2011 – March 2012, we selected 7 typical fog events including 5 stratus-lowering fog events and 2 radiation fog events. The fog observation periods (FOP) and the visibility range of the 7 fog events are listed in Table 5.2.

In Figure 5.2, the DSD-derived Vis is compared with the measured Vis at 40/80-m level during the fog observation periods of the 7 typical fog events at CESAR. Fog DSD was measured at 60-m level by the FSSP, and Vis was measured at 2-, 10-, 20-, 40-, 80-, 140-, and 200-m levels by the in situ visibility sensors. Therefore, we compare the measured Vis in the vicinity of 60 m with the DSD-derived Vis, and use the measured Vis at 40- or 80-m level which is much closer to the DSD-derived Vis. It is shown that the DSD-derived Vis coincides well with the measured Vis at 40/80 m level in each fog

Table 5.2: Fog observation periods and visibility range of 7 typical fog events observed at CESAR

Fog event	Fog type	Formation time	Dissipation time	Duration	DSD-derived visibility range (m)	Measured visibility range (m)
2011.12.21-2011.12.22	Radiation	20:20:00 UTC 2011.12.21	03:06:00 UTC 2011.12.22	6h47min	54.6 – 997.3	130 – 1340 (80 m level)
2012.01.18-2012.01.19	Stratus-lowering	21:43:00 UTC 2012.01.18	04:56:00 UTC 2012.01.19	7h14min	119.5 – 1463.7	139 – 1460 (80 m level)
2012.02.12-2012.02.13	Stratus-lowering	22:50:00 UTC 2012.02.12	04:45:00 UTC 2012.02.13	5h56min	107 – 1099.8	90 – 1500 (80 m level)
2012.02.16	Stratus-lowering	03:36:00 UTC	07:37:00 UTC	4h2min	194.2 – 1487.7	180 – 1590 (80 m level)
2012.02.17-2012.02.18	Stratus-lowering	22:20:00 UTC 2012.02.17	03:43:00 UTC 2012.02.18	5h24min	141.4 – 1502.2	120 – 1520 (40 m level)
2012.02.23-2012.02.24	Stratus-lowering	21:27:00 UTC 2012.02.23	09:57:00 UTC 2012.02.24	12h31min	126.6 – 1156.3	130 – 1580 (40 m level)
2012.03.01-2012.03.02	Radiation	22:49:00 UTC 2012.03.01	03:46:00 UTC 2012.03.02	4h58min	153.9 – 1383.2	70 – 1410 (40 m level)

Table 5.3: Goodness of fit for the Gamma-based $Vis-Z$ mode, the exponential $Vis-Z$ model, and the exponential $Vis-Z-L_a$ model based on the measured DSD datasets of the 7 typical fog events at CESAR

(SSE: Sum of Squares Due to Error, denotes the total deviations of the estimated values from the measured values; R-Square, is the ratio of the sum of squares of the regression (SSR) and the total sum of squares (SST), which measures how successful the fit is in explaining the variation of the data; Adjusted R-Square, is the R-Square adjusted based on the residual degrees of freedom; RMSE: Root Mean Squared Error, is an estimate of the standard deviation of the random component in the data.)

Goodness of fit / Model	SSE	R-Square	Adjusted R-Square	RMSE
Gamma-based Vis-Z model	138.1	0.1942	0.1947	0.2301
Exponential Vis-Z model	72.48	0.3731	0.3729	0.1667
Exponential Vis-Z-La model	2.193	0.9847	0.9847	0.029

event, except during some divergent periods such as in the fog event during 2012.02.23 - 2012.02.24, the DSD-derived Vis is much higher than the measured Vis at 40 m in almost two hours. As we have indicated before, only the DSD datasets that derive the Vis close to the measured Vis are used, so the divergent periods are filtered. In the 7 fog events there are total 2611 DSD data with 1-min time resolution that are used to validate the models.

Vis, Z, L_a are calculated from the 2611 measured DSD data with 1-min time resolution. Using the least squares method, the best-fit parameter values for the Gamma-based $Vis-Z$ model, the exponential $Vis-Z$ model, and the exponential $Vis-Z-L_a$ model can be estimated as: $\upsilon = 2$, $R_n = 0.7$ (Gamma-based $Vis-Z$ model); $a = 0.04$, $b = -0.2028$ (exponential $Vis-Z$ model); $a = -1.099$, $b = 0.1726$, $C = 0.0621$ (exponential $Vis-Z-L_a$ model). The goodness of fit for the three models based on the measured DSD datasets of the 7 typical fog events at CESAR are listed in Table 5.3.

It is shown in Table 5.3 that for the measured DSD datasets of the 7 typical fog events at CESAR, the exponential $Vis-Z-L_a$ model achieves the lowest values of SSE and RMSE, and the highest values of R-Square and Adjusted R-Square, compared to the other two models. Meanwhile, the DSD-derived Vis is also compared with the Vis estimated from the Gamma-based $Vis-Z$ model, the exponential $Vis-Z$ model, and the exponential $Vis-Z-L_a$ model, which is shown in Figure 5.3. It can be seen from Figure 5.3 that the Vis estimated from the exponential $Vis-Z-L_a$ model almost coincides with the DSD-derived Vis, which indicates the robust performance of the exponential $Vis-Z-L_a$ model for large variations in actual DSD datasets.

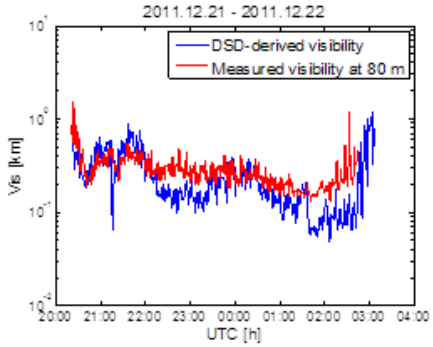

(a)

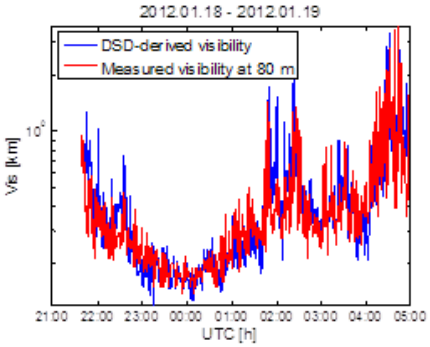

(b)

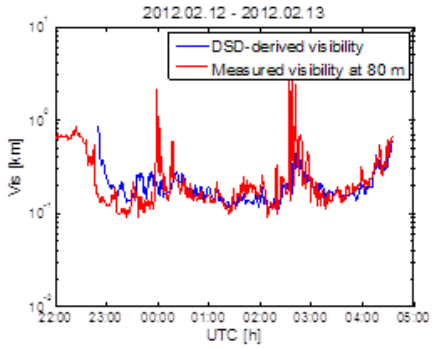

(c)

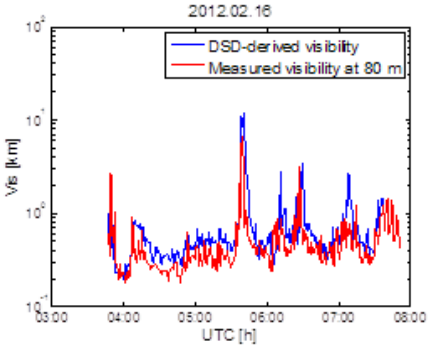

(d)

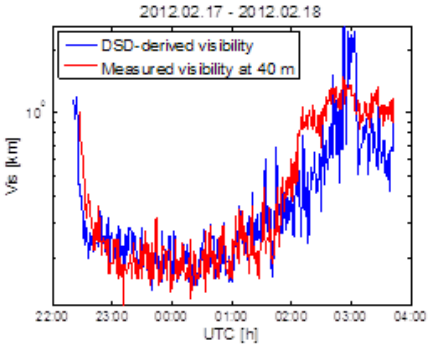

(e)

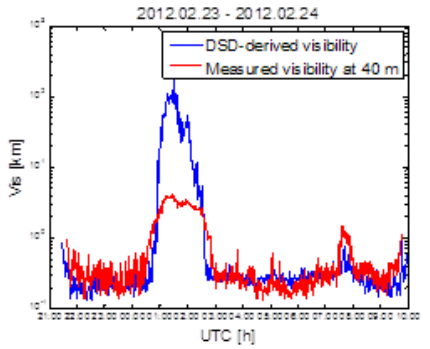

(f)

5.4. Model validation with measured Vis, Z and DSD at CESAR

5.4.1. Model validation with measured Vis and DSD-derived Z, La

The investigation of the least square errors has validated the robustness of the exponential $Vis - Z - L_a$ model over a wide range of fog conditions with the simulated DSD

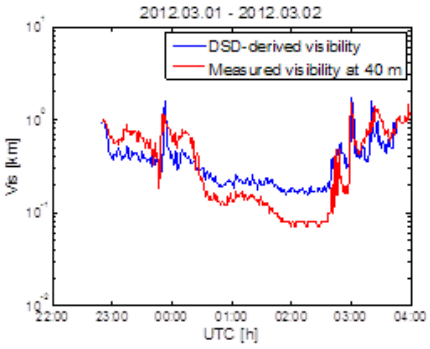

(g)

Figure 5.2: Comparison between the DSD-derived Vis and the measured Vis at 40/80-m level during the fog observation periods of the 7 typical fog events at CESAR.

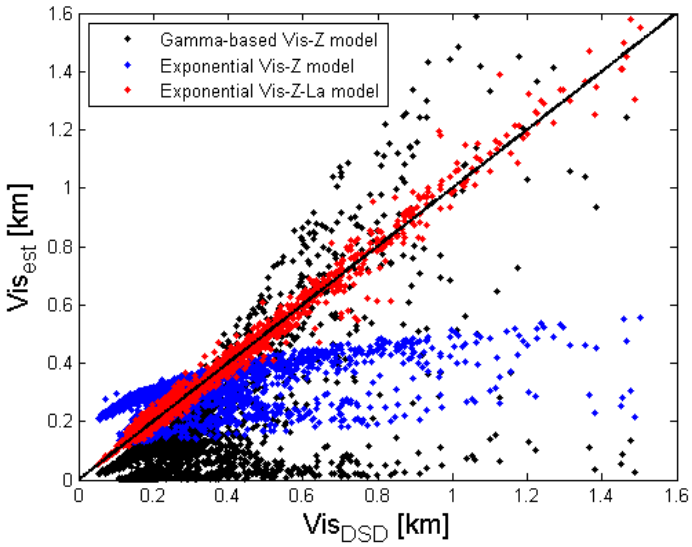

Figure 5.3: Comparison between the DSD-derived Vis and the Vis estimated from the Gamma-based $Vis-Z$ model (black dots), the exponential $Vis-Z$ model (blue dots), and the exponential $Vis-Z-L_a$ model (red dots) based on the measured DSD datasets of the 7 typical fog events at CESAR, where Vis, Z, L_a in the three models are all calculated from the measured DSD.

datasets and the measured DSD datasets at CESAR. In the model comparisons however, Vis, Z and L_a were calculated from the DSD. Of course a more realistic approach is to validate the model with the measurement data from the in situ visibility sensors and the cloud radar at CESAR. Unfortunately we do not have as many radar measurements (which were invoked manually) as we have Vis and DSD measurements, which are continuous, automatic measurements. Furthermore, we currently lack reliable L_a measure-

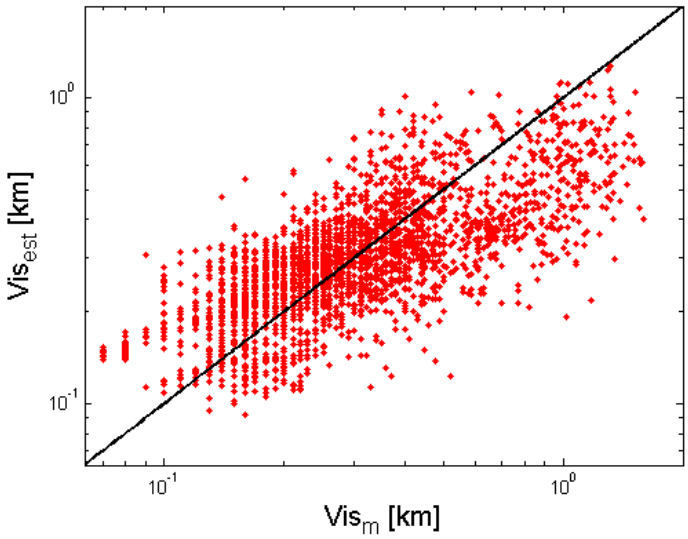

Figure 5.4: Comparison between the measured Vis from the in situ visibility sensors and the Vis estimated from the exponential $Vis-Z-L_a$ model based on the measurement data of the 7 typical fog events at CESAR, where the measured Vis and the DSD-derived Z, L_a are used in the exponential $Vis-Z-L_a$ model.

ments in our datasets, which we can only substitute by DSD-derived values.

In this work, we first substitute the DSD-derived Vis by actual measured Vis from the in situ visibility sensors and test the relation:

$$Vis_m = C \cdot L_{a_{DSD}}^{a} \cdot Z_{DSD}^{b} \tag{5.4}$$

where Vis_m is the measured visibility from the in situ visibility sensors in km; $L_{a_{DSD}}$ is the DSD-derived attenuation factor in dB/km; Z_{DSD} is the DSD-derived radar reflectivity in mm^6/m^3.

In the 7 typical fog events at CESAR, there are also 2611 Vis_m data with 1-min time resolution which have a one-to-one correspondence with the measured DSD data. First we use this dataset to tune a, b and C in Eq. (5.4). Next, the right hand side of Eq. (5.4), which results in Vis_{est} values can be plotted against the Vis_{est} values.

In Figure 5.4, the measured Vis from the in situ visibility sensors is compared with the Vis estimated from the exponential model based on the measurement data of the 7 typical fog events at CESAR, where the measured Vis and the DSD-derived Z, L_a are used in the exponential $Vis-Z-L_a$ model. The best-fit parameter values in Eq. (5.4) are estimated by the least squares method as $a=-0.6784$, $b=-0.01231$, $C=0.0372$. However, in Figure 5.4 the deviations of the estimated Vis from the measured Vis are larger than those of the estimated Vis from the DSD-derived Vis in Figure 5.3. This could have been expected and is thought to be the result of fog field variations in time and space. The DSD sampling is a 1-min time average at a certain spot, whereas the visibility measurements are taken over a certain area, which do not fully coincide with

Table 5.4: Goodness of fit with the 5 mins, 10 mins, 15 mins time-averaging applied to the measurement data of the 7 typical fog events at CESAR

(SSE: Sum of Squares Due to Error, denotes the total deviations of the estimated values from the measured values; R-Square, is the ratio of the sum of squares of the regression (SSR) and the total sum of squares (SST), which measures how successful the fit is in explaining the variation of the data; Adjusted R-Square, is the R-Square adjusted based on the residual degrees of freedom; RMSE: Root Mean Squared Error, is an estimate of the standard deviation of the random component in the data.)

Goodness of fit / Data	SSE	R-Square	Adjusted R-Square	RMSE
Original (2611 data)	90.31	0.5205	0.5201	0.1861
5 mins (525 data)	13.08	0.6232	0.6217	0.1583
10 mins (265 data)	6.177	0.6469	0.6442	0.1535
15 mins (177 data)	4.015	0.6421	0.6380	0.1519

the DSD measurement inlet. In order to reduce the deviation, time averaging can be applied to the original data with 1-min time resolution. The measured Vis and the DSD-derived Z, L_a data are simultaneously time-averaged with 5 mins, 10 mins and 15 mins.

Figure 5.5 shows the 5 min, 10 mins and 15 mins time-averaging applied to the measurement data of the 7 typical fog events at CESAR, where the measured Vis and the DSD-derived Z, L_a are used in the exponential $Vis-Z-L_a$ model.

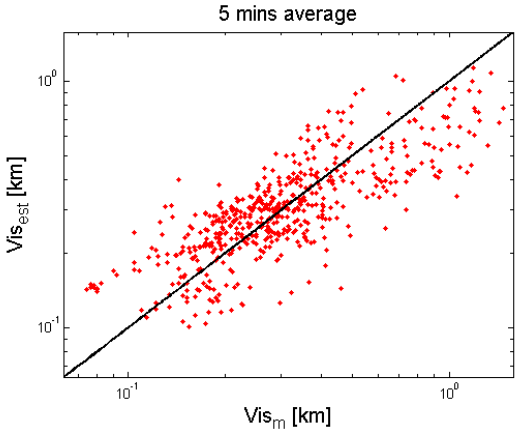

(a)

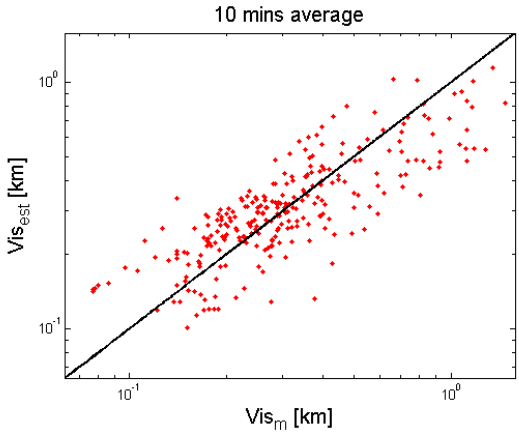

(b)

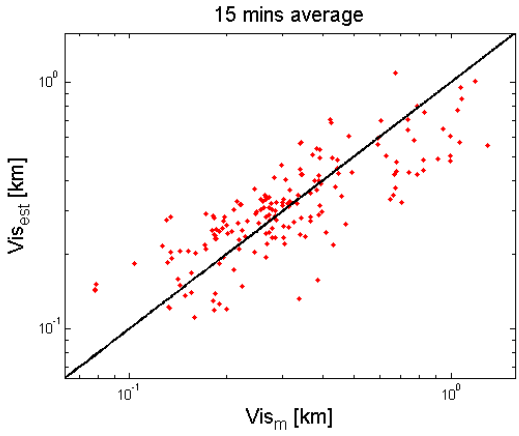

(c)

Figure 5.5: 5 mins, 10 mins and 15 mins time averaging are applied to the measurement data of the 7 typical fog events at CESAR, where the measured Vis and the DSD-derived Z, L_a are used in the exponential $Vis-Z-L_a$ model.

It can be seen from Figure 5.5 that the deviations of the estimated Vis from the measured Vis become smaller with increasing averaging time. This observation supports the idea that the immediate measurements from various sensors may deviate from each other, because they are taken from different time/space segments. The best-fit parameter values in the exponential $Vis-Z-L_a$ model for the three circumstances are $a=-0.7764$, $b=0.001944$, $C=0.0335$ (5 mins average); $a=-0.8097$, $b=0.00613$, $C=0.0322$ (10 mins average); $a=-0.8226$, $b=0.009376$, $C=0.0324$ (15 mins average). Table 5.4 shows the goodness of fit with the 5 mins, 10 mins and 15 mins time-averaging applied to the measurement data of the 7 typical fog events at CESAR.

It is shown in Table 5.4 that the 10 mins time-averaging data attain the highest degree

of goodness of fit with the largest values of R-Square and Adjusted R-Square, and the smallest values of SSE and RMSE, though the 5 mins and 15 mins time-averaging data also show improved goodness of fit than the original data. The results show the reliability of the exponential $Vis-Z-L_a$ with the actual visibility measurements, and indicate that the goodness of fit in the exponential $Vis-Z-L_a$ model can be improved with the time-averaging method by reducing the deviations from different time/space samplings.

5.4.2. Model validation with measured Vis, Z and DSD-derived La

Next, we substitute the DSD-derived Z in Eq. (5.4) by the measured Z from the cloud radar, which is expressed as:

$$Vis_m = C \cdot L_{a_{DSD}}^{a} \cdot Z_m^{b} \tag{5.5}$$

where Vis_m is the measured visibility from the in situ visibility sensor in km; $L_{a_{DSD}}$ is the DSD-derived attenuation factor in dB/km; Z_m is the measured radar reflectivity from the cloud radar in mm^6/m^3. At this stage only the L_a is derived from the DSD. As indicated we do not have L_a measurements available in our datasets.

Among the 7 typical fog events at CESAR, there is only one that has acquired simultaneous Vis, Z and DSD measurements. It occurred on February 17-18, 2012. We have depicted this fog event in Chapter 4. It is formed from low stratus clouds in a weather situation of stationary front over the Netherlands in a developing west circulation. This fog event lasted for almost five and a half hours with visibility stays below 1 km.

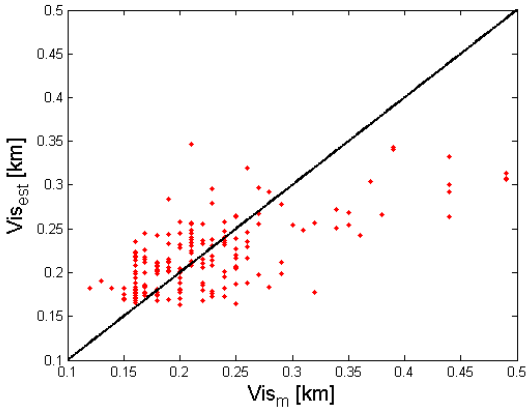

Figure 5.6: Comparison between the measured Vis from the in situ visibility sensors and the Vis estimated from the exponential $Vis-Z-L_a$ model based on the measurement data during the fog event on February 17-18, 2012, where the measured Vis, Z and the DSD-derived L_a are used in the exponential $Vis-Z-L_a$ model.

In Figure 5.6, the measured Vis from the in situ visibility sensor is compared with the Vis estimated from the exponential $Vis-Z-L_a$ model based on the measurement data during the fog event on February 17-18, 2012, where the measured Vis, Z and the DSD-derived L_a are used in the exponential $Vis-Z-L_a$ model. It has been shown in Chapter 4 that the measured Vis, Z from the in situ visibility sensors and the cloud

radar coincide well with the DSD-derived values during the fog episode, so the estimated Vis from the exponential $Vis-Z-L_a$ model based on the measured Vis, Z and the DSD-derived L_a can be very close to the measured Vis. The best-fit parameter values are estimated by the least squares method as $a=-0.2189$, $b=-0.2029$, $C=0.0172$. If we continue to apply the time-averaging method to the data, the goodness of fit will be largely improved. There are total of 313 Z measurement data with 1-min time resolution during the fog episode, but 134 of them are "lost" due to the cloud-masking processing of the radar, leaving only 179 valid Z measurement data we can use. We apply a 5 mins time-averaging to the 179 valid data, or else they are not sufficient to validate the mode if 10 mins or 15 mins time-averaging are taken.

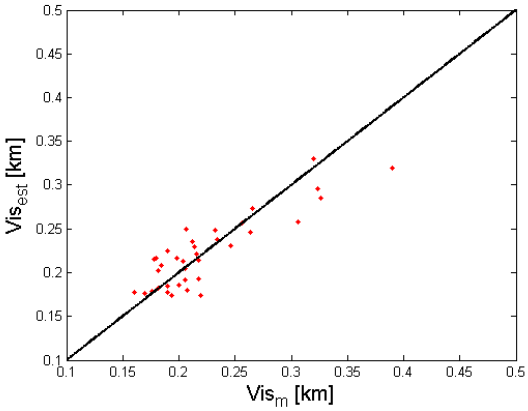

Figure 5.7: 5 mins time-averaging is applied to the measurement data during the fog event on February 17-18, 2012, where the measured Vis, Z and the DSD-derived L_a are used in the exponential $Vis-Z-L_a$ model.

Figure 5.7 shows the 5 mins time-averaging applied to the measurement data during the fog event on February 17-18, 2012, where the measured Vis, Z and the DSD-derived L_a are used in the exponential $Vis-Z-L_a$ model. The best-fit parameter values for the 5 mins time-average data are estimated as $a=-0.3138$, $b=-0.1894$, $C=0.0154$. Table 5.5 shows the goodness of fit with the 5 mins time-averaging applied to the measurement data during the fog event on February 17-18, 2012.

It is shown in Figure 5.7 that the estimated Vis gets closer to the measured Vis after applying the 5 mins time-averaging to the original data. It is expected that the goodness of fit would be further improved by applying the 10 min or 15 mins time-averaging if there are sufficient data in the datasets. In Table 5.5, R-Square is increased from 0.4154 to 0.7198, Adjusted R-Square is increased from 0.4088 to 0.7029, and SSE and RMSE are almost decreased by half, which indicates that the time-averaging method can efficiently improve the estimated accuracy of Vis in the exponential $Vis-Z-L_a$ model by reducing the deviations from different time/space samplings. The results show that the exponential $Vis-Z-L_a$ is also applicable to the simultaneous measured Vis and Z.

Table 5.5: Goodness of fit with the 5 mins time-averaging applied to the measurement data during the fog event on February 17-18, 2012

(SSE: Sum of Squares Due to Error, denotes the total deviations of the estimated values from the measured values; R-Square, is the ratio of the sum of squares of the regression (SSR) and the total sum of squares (SST), which measures how successful the fit is in explaining the variation of the data; Adjusted R-Square, is the R-Square adjusted based on the residual degrees of freedom; RMSE: Root Mean Squared Error, is an estimate of the standard deviation of the random component in the data.)

Goodness of fit / Data	SSE	R-Square	Adjusted R-Square	RMSE
Original (179 data)	1.463	0.4154	0.4088	0.09116
5 mins (36 data)	0.08052	0.7198	0.7029	0.0494

5.5. Conclusion

In this chapter we put forward a new visibility estimator model $Vis = f(Z, L_a)$, where Vis can be deduced from radar signals only, i.e. reflectivity Z and attenuation L_a. An exponential $Vis-Z-L_a$ model $Vis = C \cdot L_a^a \cdot Z^b$ was derived by adding L_a into the exponential $Vis-Z$ model $Vis = a \cdot Z^b$, considering that both Vis and Z can be parameterized in terms of LWC, and LWC is proportional to L_a at a given radar frequency.

The exponential $Vis-Z-L_a$ model resulted in a higher estimated accuracy of Vis than the Gamma-based $Vis-Z$ model and the exponential $Vis-Z$ model, when tested on a large group of simulated DSD datasets. The simulated DSD datasets were generated from the parameter sets of modified Gamma size distribution of fog droplets for various fog types and evolutionary stages of fog given by Tomasi and Tampieri. Next, the exponential $Vis-Z-L_a$ model was also validated with the DSD datasets that were measured by the FSSP at CESAR.

In addition, a more realistic approach was used to validate the model with the measurement data from the in situ visibility sensors and the cloud radar at CESAR. As we lacked reliable L_a measurements in our datasets, we can only use DSD-derived L_a in the model. We first substituted the DSD-derived Vis by actual measured Vis, and then substituted the DSD-derived Z by the measured Z, to test the exponential $Vis-Z-L_a$ model. The measured Vis was compared with the estimated Vis from the exponential $Vis-Z-L_a$ model, and the results showed that the deviations of the estimated Vis from the measured Vis are larger than those of the estimated Vis from the DSD-derived Vis, which results from the spatial variability of instrumentation (radar, visibility sensors, FSSP) and the different sampling volumes. The measurement errors from the instruments could also enlarge the deviations of the estimated Vis from the measured Vis. In order to reduce the deviations, time-averaging method was applied to the original data with 1-min time resolution. The results showed that the goodness of fit was improved.

Finally, it can be observed that the regression parameters in the exponential $Vis - Z - L_a$ model slightly differ from dataset to dataset. There is no generic set of parameters a, b, C. One important reason is due to the limited accuracy of sensors and lack of calibration. Moreover, the parameters may also change for different fog types and stages. Therefore, we must conclude that our exponential $Vis - Z - L_a$ model, although it is superior to other models, it still has to be tuned to the specific conditions.

6

Towards the design of an advanced fog-visibility radar

6.1. Introduction

In the previous chapter we introduced a new Vis estimator model, where Vis can be deduced from radar signals only, i.e. reflectivity Z and attenuation L_a. The robust performance of the model has been validated on simulation data in literature and on measurement data from CESAR. Based on the proposed $Vis - Z - L_a$ model, we are enlightened to develop an advanced fog-visibility radar which can provide Vis estimates from simultaneous Z and L_a measurements. In the previous datasets, we do not have many Z measurements due to the limitation of radar sensitivity. Furthermore, reliable L_a measurements are lacking because it is difficult to measure L_a with a single-wavelength radar due to the heterogeneity of fog. To this end, we have started the investigation on the design of multi-wavelength radar instrument with which a high sensitivity to fog can be reached in a relatively long distance (Jankiraman, 2007; Anderson, 2008). Meanwhile, L_a can be estimated from LWC which is retrieved from the multi-wavelength radar measurements. Many approaches have been proposed to retrieve the LWC by dual-wavelength radar (Martner et al., 1993; Vivekanandan et al., 2001; Gaussiat et al., 2003; Hogan et al., 2005). This type of fog radar can acquire continuous, reliable Z and L_a measurements, which we can use to deduce Vis based on the $Vis-Z-L_a$ model. However, errors in the multi-wavelength Z measurements will lead to errors in the L_a estimates, and both errors in the Z and L_a will lead to errors in the Vis estimates. An Error analysis on Vis estimates is very important for making the choice of radar frequency combinations for fog measurements.

Besides the requirements on Z and L_a measurements, many other meteorological and operational requirements have to be considered for the design of an advanced fog-visibility radar, such as the operational modes, the spatial and temporal resolution, the adverse effects of ground-reflections on the signal quality caused by the antenna sidelobes, and the radar physical dimensions etc.

The performance of the specified fog radar can be testified on the simulated datasets for various fog types and evolutionary stages of fog. This chapter is structured as follows: Section 6.2 puts forward the meteorological and operational requirements for an advanced fog-visibility radar; Section 6.3 describes the dual-wavelength technique for L_a estimates; Section 6.4 analyzes the error estimates in Vis which result from errors in Z measurements and L_a retrieval, and the most optimum radar frequency combination can be determined from the least errors in Vis; Section 6.5 is the conclusion of this chapter.

6.2. Operational requirements for an advanced fog-visibility radar

6.2.1. Radar sensitivity improvement for fog measurements

For pulse radar, the noise equivalent radar reflectivity Z_{ne} versus the maximum detection range R_{max} is expressed as:

$$Z_{ne} = \frac{R_{max}^2 \cdot l_a \cdot k_B T_0 B F}{C \cdot |K|^2 \cdot N_{coh} \cdot N_{non-coh}} \tag{6.1}$$

where $C = \frac{\pi^3 P_t G^2 \theta \phi c \tau}{1024 \ln 2 \lambda^2 l_s}$ is the intrinsic radar constant, P_t is the transmit power, G is the antenna gain, θ and ϕ are the azimuth and elevation beamwidths, τ is the pulse width, λ is the radar wavelength, l_s is the radar system loss; l_a is the atmospheric loss; $P_n = k_B T_0 B F$ is the noise power of radar, $k_B = 1.38 \times 10^{-23}\ W/(Hz \cdot K)$ is Boltzman's constant, T_0 is the system temperature (usually 290 K), B is the receiver noise bandwidth in Hz, F is the noise factor expressed as a dimensionless ratio; N_{coh} and $N_{non-coh}$ are the number of coherent and non-coherent averages respectively.

The receiver filter is assumed matched to the pulse width as $B \approx 1/\tau$, which we can substitute in Eq. (6.1),

$$Z = \frac{R_{max}^2 \cdot l_a \cdot k_B T_0 F}{C' \cdot |K|^2 \cdot \tau^2 \cdot N_{coh} \cdot N_{non-coh}} \tag{6.2}$$

where $C' = \frac{\pi^3 P_t G^2 \theta \phi c}{1024 \ln 2 \lambda^2 l_s}$ is the radar constant excluding τ. It can be seen from Eq. (6.2) that in order to improve the radar sensitivity, we can increase τ and radar constant C'. The radar constant C' can be increased by increasing transmit power P_t, radar frequency f, and the product of antenna gain and beamwidths $G^2 \theta \phi$.

Taking the 35 GHz cloud radar at CESAR for example. Figure 6.1 shows the Vis versus Z measurements at CESAR during the fog event on February 17-18, 2012. The Vis was measured by the 40-m visibility sensor and was also calculated from the DSD. The Z was measured by the 35 GHz cloud radar and was calculated from the DSD. In order to reduce the sampling deviations between the Vis and Z measurements resulting from the spatial variability of the 40-m visibility sensor and the cloud radar, we used Z measurements in the 8$^{\text{th}}$ range gate of radar, which corresponds to 39.5 m level. Considering the height of antenna and the 3-dB beamwidth, the 39.5 m vertical height corresponds to the range $R = (39.9 - 5)/\sin(3.5° - 0.34°/2) \approx 600$ m, where 5 m is the height of antenna, 0.34° is the 3-dB beamwidth. It can be seen from Figure 6.1 that the Z measurements in the 8$^{\text{th}}$ range gate of radar can only get to as low as -48 dBZ which is higher than most DSD-derived Z. That is, the 35 GHz cloud radar at CESAR can only measure the fog with Z as low as -48 dBZ at 600 m distance. However, in the sensitivity calculation in Chapter 3, at 600 m distance the radar can theoretically measure the fog with Z as low as -52.5 dBZ, which is about 5 dB lower than the actual Z measurements could achieve. The reason is that the transmit power cannot always reach up to its maximum value 200 W, and the noise figure was worse due to problems with LNA. In the sensitivity calculation, the radar can theoretically measure the fog with $Z = -38.4$ at 3 km distance.

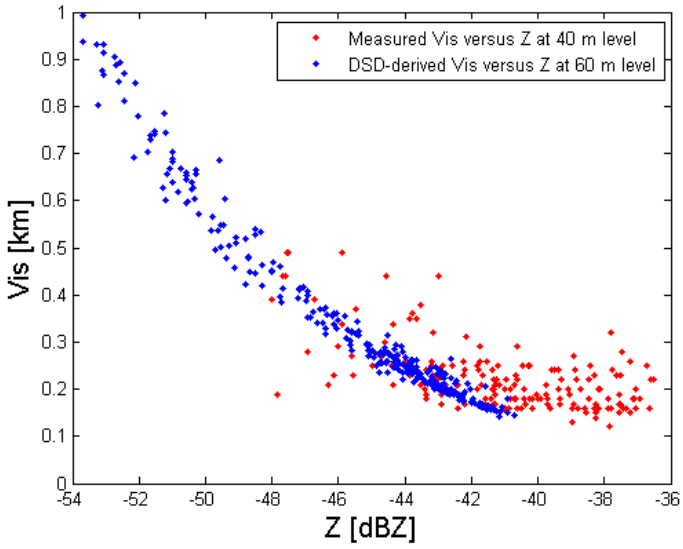

Figure 6.1: Vis versus Z measurements at CESAR during the fog event on February 17-18, 2012. The red dots denote the measured Vis with the 40-m visibility sensor versus the measured Z with the 35 GHz cloud radar, and the blue dots denote Vis versus Z both derived from the measured DSD.

The "fog mode" operational parameters of the 35 GHz cloud radar at CESAR are listed in Table 3.1. First we examine the effect of radar frequency f on the sensitivity. We have increased $f = 35$ GHz to $f = 94$, 140, 220 GHz respectively. Correspondingly, we assume that the noise figure is increased from $NF = 6.3$ dB to $NF = 8$, 10, 12 dB, and the radar system loss is increased from $L_s = 7$ dB to $L_s = 9$, 11, 13 dB. The radar sensitivity with $f = 35$, 94, 140, 220 GHz is shown in Figure 6.2. It can be seen from Figure 6.2 that at the same R_{max}, the radar achieves the lowest Z values at $f = 94$ GHz, and it can measure the fog with $Z = -42$ dBZ at 3 km distance. There is about 4 dB improvement of radar sensitivity while increasing $f = 35$ GHz to $f = 94$ GHz. The sensitivity is also improved at $f = 140$, 220 GHz, but not better than that at $f = 94$ GHz. The reason is that the attenuation induced by fog droplets also increases with increasing f, and it would offset the improvement of radar sensitivity brought by increasing f to some extent. The Z that the radar can measure at 3 km distance with $f = 35$, 94, 140, 220 GHz are listed in Table 6.1.

Next, we examine the effect of transmit power P_t on the sensitivity. Leaving the other parameters in Eq. (6.2) unchanged, we have increased maximum $P_t = 200$ W to $P_t = 400$, 600, 800 W respectively, which is shown in Figure 6.3. It can be seen from Figure 6.3 that at the same R_{max}, the radar achieves the lowest Z values at $P_t = 800$ W, and it can measure the fog with $Z = -44.5$ at 3 km distance. There is about 6 dB improvement of radar sensitivity while only increasing maximum $P_t = 200$ W to $P_t = 800$ W. However, P_t cannot be infinitely large due to the limitation of transmitter design. Table 6.2 lists the Z that the radar can measure at 3 km distance with $P_t = 200$, 400, 600, 800 W.

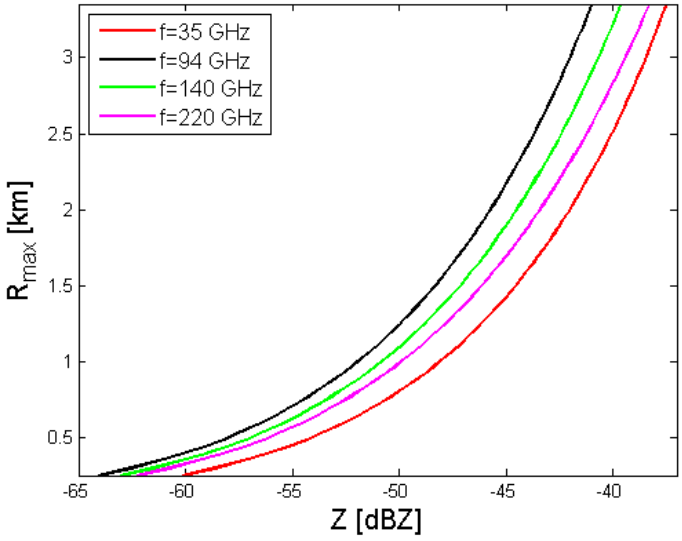

Figure 6.2: The maximum detection range of radar R_{max} versus the corresponding radar reflectivity Z with $f = 35, 94, 140, 220$ GHz.

Table 6.1: The Z that the radar can measure at 3 km distance with $f = 35, 94, 140, 220$ GHz

f(GHz) / R_{max}(km)	35	94	140	220
3 km	-38.4 dBZ	-42.0 dBZ	-40.7 dBZ	-39.4 dBZ

Table 6.2: The Z that the radar can measure at 3 km distance with $f = 35, 94, 140, 220$ GHz

P_t(W) / R_{max}(km)	200	400	600	800
3 km	-38.4 dBZ	-41.5 dBZ	-43.2 dBZ	-44.5 dBZ

Last, we examine the effect of pulse width τ on the sensitivity. Leaving the other parameters in Eq. (6.2) unchanged, we have increased $\tau = 600$ ns to $\tau = 800, 1200, 1500$ ns respectively, which is shown in Figure 6.4. It can be seen from Figure 6.4 that at the same R_{max}, the radar achieves the lowest Z values at $\tau = 1500$ ns, and it can measure the fog with $Z = -46.4\ dBZ$ at 3 km distance. There is about 8 dB improvement of radar sensi-

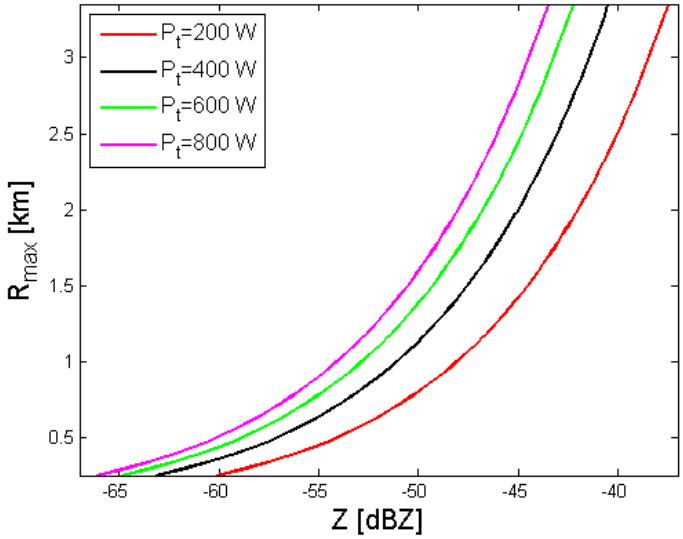

Figure 6.3: The maximum detection range of radar R_{max} versus the corresponding radar reflectivity Z with P_t = 200, 400, 600, 800 W.

Table 6.3: The Z that the radar can measure at 3 km distance with τ = 600, 800, 1200, 1500 ns

τ (ns) / R_{max} (km)	600	800	1200	1500
3 km	-38.4 dBZ	-40.9 dBZ	-44.5 dBZ	-46.4 dBZ

tivity while only increasing τ = 600 ns to τ = 1500 ns. However, large τ would lead to poor range resolution, and τ = 1500 ns results in a range resolution ΔR = 225 m. Considering that fog layers are normally thin and highly variable in space, we have to adjust the range resolution to be less than or equal to 100 m, which corresponds to a maximum τ = 666 ns. Table 6.3 lists the Z that the radar can measure at 3 km distance with τ = 600, 800, 1200, 1500 ns.

Considering all the impacting factors above on the radar sensitivity, we choose f = 94 GHz, NF = 8 dB, L_s = 9 dB, P_t = 800 W, τ = 600 ns as an optimum parameter set, and the other parameters in Eq. (6.2) remain unchanged. In Figure 6.5, the improved sensitivity with the optimum parameter set is compared with the original sensitivity of the 35 GHz cloud radar at CESAR on fog measurements. It can be seen from Figure 6.5 that the radar can measure the fog with Z as low as -48 dBZ at 3 km distance with the improved sensitivity, and the original Z can only get to -38.4 dBZ at 3 km distance.

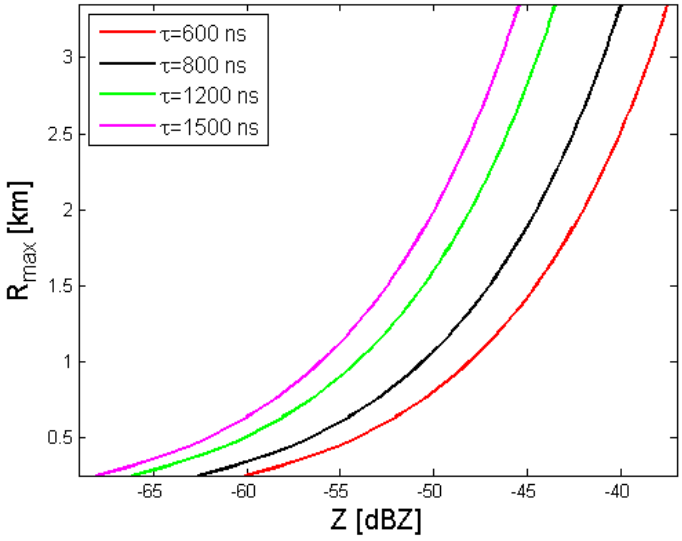

Figure 6.4: The maximum detection range of radar R_{max} versus the corresponding radar reflectivity Z with τ = 600, 800, 1200, 1500 ns.

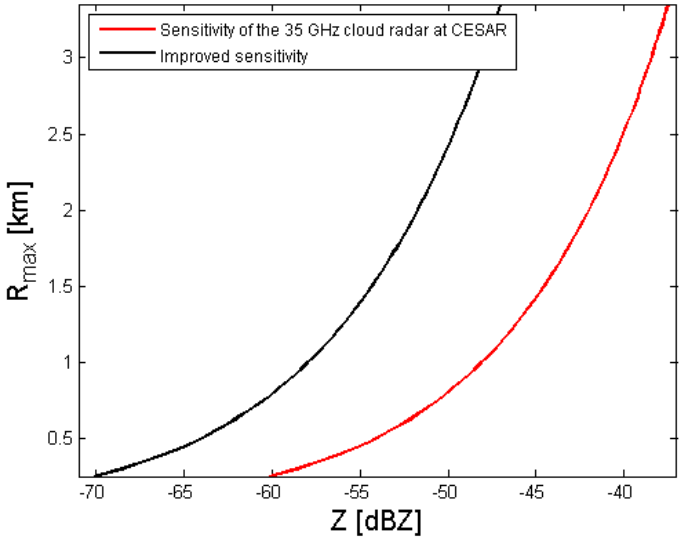

Figure 6.5: Comparison of the improved sensitivity with f = 94 GHz, NF = 6.3 dB, L_s = 7 dB, P_t = 800 W, τ = 600 ns with the original sensitivity of the 35 GHz cloud radar at CESAR with f = 35 GHz, NF = 8 dB, L_s = 9 dB, P_t = 200 W, τ = 600 ns.

6.2.2. Operational parameters of an advanced fog-visibility radar

The optimum operational parameters of fog radar will vary with different fog types and evolutionary stages of fog. Therefore, we would take into account the intensity scales of various fogs towards the design of an advanced fog-visibility radar. In the previous chapter, we have simulated a large group of DSD datasets for various fog types and evolutionary stages of fog on the basis of the parameter sets of modified Gamma size distribution of fog droplets given by (Tomasi and Tampieri, 1976). The DSD datasets are generated for each type of fog and each stage of fog in a scope of visibility levels (0.01, 0.02, 0.05, 0.1, 0.2, 0.5, 1 km). In order to determine the optimum radar frequency for fog measurements, we have calculated the Z and L_a at f = 3, 10, 35, 94, 140, 220 GHz from the simulated DSD. As the assumed size range of fog droplets is between 0.5 - 49.5 μm in radius, we have to examine if the Rayleigh approximation is still applicable in the calculation of Z and L_a at higher radar frequencies such as f = 140, 220 GHz. Figure 6.6(a) and (b) show the calculated Z, L_a in Mie scattering versus the calculated Z, L_a in Rayleigh scattering at f = 220 GHz based on the simulated DSD. Figure 6.7(a) and (b) plot the difference of Z, L_a between Mie and Rayleigh scattering for all the simulated DSD samples. It can be found from Figure 6.7(a) and (b) that the maximum difference values in Z and L_a are 0.004 dB and 3 dB/km, which indicates that Rayleigh scattering can fully replace Mie scattering in the calculation of Z and L_a. So, for all considered frequencies in this study, Rayleigh scattering will be assumed.

In Rayleigh scattering, Z is only dependent on the fog DSD, while L_a is not only dependent on the fog DSD, but is also directly proportional to the radar frequency f. Table 6.4 lists the calculated Z and two-way L_a in dB for each type of fog and each stage of fog at f = 3, 10, 35, 94, 140, 220 GHz in a scope of Vis levels (0.01, 0.02, 0.05, 0.1, 0.2, 0.5, 1 km) based on the simulated DSD. The six L_a values in each column correspond to f = 3, 10, 35, 94, 140, 220 GHz respectively.

It can be seen from Table 6.4 that for each type of fog and each stage of fog, Z decreases with increasing Vis, but is independent of f at each Vis level. L_a also decreases with increasing Vis, but increases with increasing f at each Vis level. Therefore, the choice of operational parameters of an advanced fog-visibility radar largely depends on the Z and L_a values for various fog types and evolutionary stages of fog.

Besides the attenuation induced by fog droplets, the gaseous attenuation from oxygen and water vapor also has to be taken into account. A simplified algorithm is used for approximate estimation of gaseous attenuation in the frequency range 1 - 350 GHz for a limited range of meteorological conditions and a limited variety of geometrical configurations (Geneva, 1995). Table 6.5 lists the approximate attenuation from oxygen and water vapor at f = 3, 10, 35, 94, 140, 220 GHz, where the water vapor density is assumed as 7.5 $g \cdot m^{-5}$.

It can be seen from Table 6.5 that the gaseous attenuation increases with increasing f, and it can arrive at large values at high f, though it is still small compared to the attenuation from fog droplets at the same f. To determine the operational parameters of the fog radar, we have to use the sum of attenuation from fog droplets and gases.

In order to satisfy the requirements on radar sensitivity, the ground fog with the lowest Z values among the various fogs needs to be considered in priority. The lowest Z in the ground fog is -46.3 dBZ at Vis = 1 km, which is shown in Table 6.4. Therefore, only

Table 6.4: The calculated Z and two-way L_a in dB for each type of fog and each stage of fog at f = 3, 10, 35, 94, 140, 220 GHz in a scope of Vis levels (0.01, 0.02, 0.05, 0.1, 0.2, 0.5, 1 km) based on the simulated DSD

Vis(km) / Fog Type	0.01	0.02	0.05	0.1	0.2	0.5	1
Radiation Fog	Z=-14.3 La=0.0278 0.3075 3.5085 17.2574 27.9140 44.8131	Z=-17.3 La=0.0139 0.1537 1.7534 8.6244 13.9501 22.3955	Z=-21.2 La=0.0057 0.0629 0.7175 3.5292 5.7087 9.1650	Z=-24.3 La=0.0028 0.0312 0.3558 1.7503 2.8311 4.5453	Z=-27.3 La=0.0014 0.0154 0.1759 0.8650 1.3991 2.2462	Z=-31.3 La=5.6464e-4 0.0062 0.0712 0.3501 0.5662 0.9091	Z=-34.3 La=2.7768e-4 0.0031 0.0350 0.1721 0.2785 0.4470
Evaporation Fog	Z=-20.4 La=0.0156 0.1723 1.9650 9.6566 15.6000 24.9698	Z=-23.4 La=0.0078 0.0862 0.9825 4.8283 7.8000 12.4849	Z=-27.4 La=0.0031 0.0345 0.3930 1.9313 3.1200 4.9940	Z=-30.5 La=0.0015 0.0168 0.1916 0.9415 1.5210 2.4346	Z=-33.5 La=7.6051e-4 0.0084 0.0958 0.4708 0.7605 1.2173	Z=-37.5 La=3.0421e-4 0.0034 0.0383 0.1883 0.3042 0.4869	Z=-40.5 La=1.5210e-4 0.0017 0.0192 0.0942 0.1521 0.2435
Advection Fog	Z=-12.0 La=0.0336 0.3718 4.2432 20.8924 33.8428 54.5227	Z=-15.1 La=0.0168 0.1859 2.1216 10.4462 16.9214 27.2614	Z=-19.0 La=0.0068 0.0747 0.8530 4.1999 6.8032 10.9600	Z=-22.0 La=0.0034 0.0372 0.4251 2.0928 3.3901 5.4615	Z=-33.5 La=7.6051e-4 0.0084 0.0958 0.4708 0.7605 1.2173	Z=-37.5 La=3.0421e-4 0.0034 0.0383 0.1883 0.3042 0.4869	Z=-40.5 La=1.5210e-4 0.0017 0.0192 0.0942 0.1521 0.2435
Arctic Marine Fog	Z=-6.7 La=0.0388 0.4290 4.8950 24.0916 39.0015 62.7403	Z=-9.7 La=0.0194 0.2145 2.4475 12.0458 19.5008 31.3702	Z=-13.6 La=0.0079 0.0871 0.9940 4.8919 7.9195 12.7395	Z=-16.6 La=0.0039 0.0434 0.4950 2.4361 3.9438 6.3441	Z=-19.6 La=0.0020 0.0219 0.2499 1.2299 1.9910 3.2029	Z=-23.7 La=7.7864e-4 0.0086 0.0982 0.4832 0.7822 1.2583	Z=-26.7 La=3.9023e-4 0.0043 0.0492 0.2422 0.3920 0.6307

Ground Fog	Z=-26.3	Z=-29.3	Z=-33.2	Z=-36.2	Z=-39.2	Z=-43.3	Z=-46.3
	La=0.0117	La=0.0059	La=0.0024	La=0.0012	La=5.9389e-4	La=2.3579e-4	La=1.1730e-4
	0.1293	0.0646	0.0263	0.0131	0.0066	0.0026	0.0013
	1.4742	0.7371	0.2994	0.1497	0.0748	0.0297	0.0148
	7.2432	3.6216	1.4709	0.7355	0.3675	0.1459	0.0726
	11.6983	5.8491	2.3757	1.1878	0.5936	0.2357	0.1172
	18.7137	9.3569	3.8004	1.9002	0.9495	0.3770	0.1875
Formation Fog	Z=-13.1	Z=-16.2	Z=-20.2	Z=-23.2	Z=-26.2	Z=-30.2	Z=-33.2
	La=0.0302	La=0.0149	La=0.0060	La=0.0030	La=0.0015	La=5.8849e-4	La=2.9522e-4
	0.3334	0.1641	0.0658	0.0330	0.0164	0.0065	0.0033
	3.8028	1.8718	0.7507	0.3769	0.1869	0.0742	0.0372
	18.7015	9.2051	3.6917	1.8535	0.9193	0.3647	0.1830
	30.2417	14.8853	5.9698	2.9973	1.4866	0.5898	0.2959
	48.5188	23.8811	9.5776	4.8087	2.3850	0.9462	0.4747
Mature Fog	Z=-10.5	Z=-13.5	Z=-17.4	Z=-20.4	Z=-23.5	Z=-27.4	Z=-30.5
	La=0.0330	La=0.0166	La=0.0068	La=0.0033	La=0.0017	La=6.6844e-4	La=3.2993e-4
	0.3648	0.1836	0.0747	0.0368	0.0184	0.0074	0.0036
	4.1619	2.0945	0.8525	0.4201	0.2097	0.0842	0.0416
	20.4697	10.3014	4.1928	2.0662	1.0312	0.4144	0.2045
	33.1073	16.6613	6.7813	3.3418	1.6679	0.6702	0.3308
	53.1399	26.7426	10.8843	5.3638	2.6770	1.0756	0.5309
Dissipation Fog	Z=-8.4	Z=-11.4	Z=-15.4	Z=-18.4	Z=-21.5	Z=-25.4	Z=-28.4
	La=0.0366	La=0.0183	La=0.0073	La=0.0036	La=0.0018	La=7.2638e-4	La=3.6565e-4
	0.4040	0.2020	0.0803	0.0399	0.0202	0.0080	0.0040
	4.6093	2.3047	0.9157	0.4547	0.2305	0.0916	0.0461
	22.6769	11.3384	4.5048	2.2371	1.1338	0.4505	0.2268
	36.6916	18.3458	7.2889	3.6198	1.8346	0.7289	0.3669
	58.9480	29.4740	11.7103	5.8155	2.9474	1.1710	0.5895

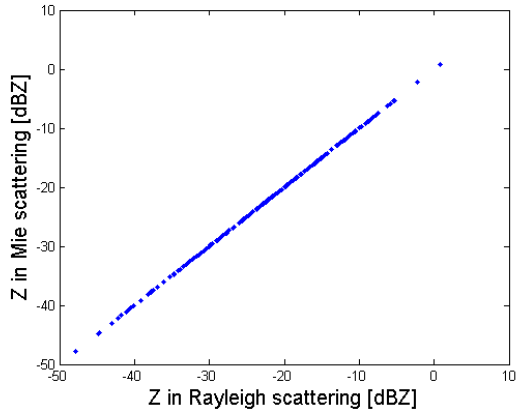

(a)

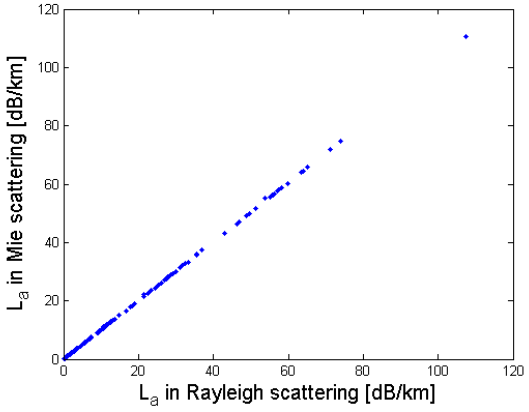

(b)

Figure 6.6: The calculated Z, L_a in Mie scattering versus the calculated Z, L_a in Rayleigh scattering at $f = 220$ GHz based on the simulated DSD.

if the radar sensitivity can reach up to -46.3 dBZ at required distance, the other fogs can also be measured by the radar. It should be noted that the operational parameters of the radar are all to be determined based on the simulated datasets for various fog types and evolutionary stages of fog. In accordance with our requirements, the maximum detection range of the radar is 3 km. That is, the radar is required to be able to measure the ground fog with $Z = -46.3$ dBZ at 3 km distance. Furthermore, as fog layers are normally thin and highly variable in space, the horizontal resolution of the radar shall be less than or equal to 100 m. Hence, we assume 4 range resolution values $\Delta R = 12.5, 25, 50, 100$ m. The frequency is assumed as $f = 3, 10, 35, 94, 140, 220$ GHz respectively. Correspondingly, the noise figure is assumed as $NF = 1, 3, 5, 8, 10, 12$ dB at these frequencies, and

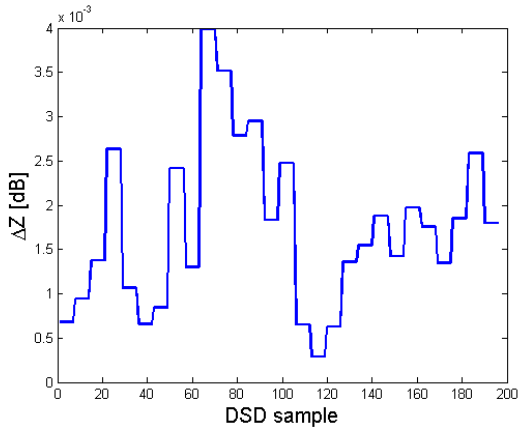

(a)

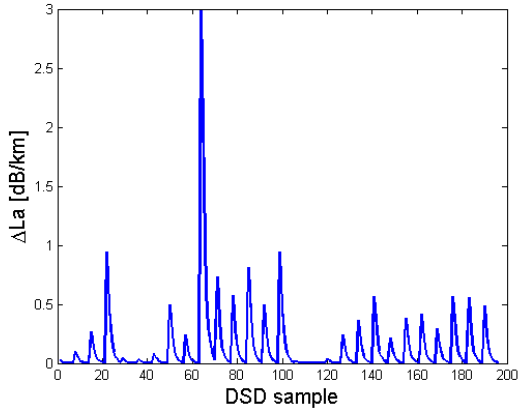

(b)

Figure 6.7: The difference of Z, L_a between Mie and Rayleigh scattering for all the simulated DSD samples.

the radar system loss is assumed as L_s = 5, 5, 7, 9, 11, 13 dB. The operational parameters of a pulse-Doppler radar are listed in Table 6.6. To achieve the minimum detectable reflectivity at 3 km distance, the transmit power P_t is calculated at f = 3, 10, 35, 94, 140, 220 GHz respectively, and minimum P_t will be chosen at an optimum f for each Vis level. Meanwhile, 256 points FFT is used in the coherent spectral analysis which will further improve the radar sensitivity by $10 \cdot \log_{10}(256) = 24$ dB.

Table 6.7 lists the required minimum P_t of the pulse-Doppler radar at an optimum f for each Vis level of the ground fog, in order to achieve the minimum detectable reflectivity at 3 km distance. It can be seen from Table 6.7 that there are two optimum candidate f at various Vis levels for the pulse-Doppler radar. f = 94 GHz is much more suited for higher Vis levels than f = 35 GHz. The reason is that at lower Vis levels the at-

Table 6.5: The approximate attenuation from oxygen and water vapor at f = 3, 10, 35, 94, 140, 220 GHz, where the water vapor density is assumed as 7.5 $g \cdot m^{-3}$

Lg(dB/km) / f(km)	Oxygen	Water vapor	Total loss
3	0.0154	0.0011	0.0165
10	0.0175	0.0144	0.0319
35	0.0691	0.1685	0.2376
94	0.0583	0.9270	0.9853
140	0.0344	2.2405	2.2749
220	0.0277	6.0962	6.1239

Table 6.6: The operational parameters of a pulse-Doppler radar

Radar Frequency	3, 10, 35, 94, 140, 220 GHz
Range Resolution	12.5, 25, 50, 100 m
Noise Figure	1, 3, 5, 8, 10, 12 dB
Radar System Loss	5, 5, 7, 9, 11, 13 dB
Antenna Gain	57 dBi
3-dB Beamwidth	0.4°
Radar Beam Elevation	3.5°

Table 6.7: The minimum $P_t(W)$ of the pulse-Doppler radar at an optimum f for each Vis level of the ground fog

ΔR (m) / Vis (km)	12.5	25	50	100	Optimum f (GHz)
	$P_t(W)$				
0.01	228	57	14	4	35
0.02	274	69	17	4	35
0.05	499	125	31	8	35
0.1	900	225	56	14	35
0.2	1711	428	107	27	35
0.5	4088	1022	256	64	94
1	7812	1953	488	122	94

tenuation of f = 94 GHz is much larger than that of f = 35 GHz. Moreover, the minimum P_t increases with increasing Vis levels at a given range resolution. The reason is that Z decreases with increasing Vis, and much higher P_t is required in order to reach lower Z in Eq. (6.2). Furthermore, the minimum P_t increases with increasing range resolution.

Implementation of FMCW (Frequency Modulated Continuous Wave) technology can

Table 6.8: The operational parameters of a FMCW radar

Radar Frequency	3, 10, 35, 94, 140, 220 GHz
Range Resolution	12.5, 25, 50, 100 m
Noise Figure	1, 3, 5, 8, 10, 12 dB
Radar System Loss	5, 5, 7, 9, 11, 13 dB
Antenna Gain	57 dBi
3-dB Beamwidth	0.4°
Radar Beam Elevation	3.5°
Sweep Time	80 μs

reduce the transmit power P_t. It is an efficient and reliable solution thanks to its high performance and drastic cost reduction. Table 6.8 lists the operational parameters of a FMCW radar, which continuously transmits and receives signals at a sweep time T_s. Unlike the pulse radar, the FMCW radar does not require as high P_t as the pulse radar to reach the same sensitivity because of its long and continuous sweep time. Table 6.9 lists the minimum P_t of the FMCW radar at an optimum f for each Vis level of the ground fog. It can be seen from Table 6.9 that the transmit power P_t is largely reduced by the FMCW technology. However, it has to be guaranteed that the transmitter is well isolated with the receiver for the FMCW radar systems, in order to prevent the transmitting signals entering into the receiver signal processor. In general, there are two separate antennas which are used for transmit and receive for the FMCW radar systems. Alternatively, we could use the pulse compression with a solid-state transmitter, especially at long ranges. For instance, we can use short pulses between ranges 0 - 1 km, and use long pulses between ranges 1 -3 km with the pulse compression technology, which helps to achieve high range resolution at long ranges. However, more transmit power will be required while introducing the pulse compression technology.

It can be seen from Table 6.9 that there are also two optimum candidate f at various Vis levels for the FMCW radar. f = 94 GHz is much more suited for higher Vis levels than f = 35 GHz. Therefore, it is difficult to choose a single optimum f for fog measurements due to the highly variable Vis in time and space. Furthermore, there is large difficulty in measuring L_a with a single frequency radar due to the heterogeneity of fog. To this end, we will investigate the feasibility of multi-wavelength radar technology for fog measurements. On one hand, the multi-wavelength technology can reach high sensitivity to fog in a relatively long distance. On the other hand, L_a can be retrieved from multi-wavelength Z measurements, and the Z, L_a measurements can be used to deduce Vis based on the $Vis-Z-L_a$ model. This part of work will be discussed in the following.

Moreover, many other meteorological and operational requirements have to be considered for the design of fog radar. The radar shall be capable of operating in two modes. One is horizontal mode, where the radar beam is fixed at a low elevation and pointing nearly horizontally in a given direction. In this way, the radar beam can sufficiently penetrate into the fog and probe the fog in detail. The other is scanning mode, where the radar scans the fog layers to obtain a three-dimensional profile.

Table 6.9: The minimum P_t of the FMCW radar at an optimum f for each Vis level of the ground fog

ΔR (m) / Vis (km)	12.5	25	50	100	Optimum f
	$P_t(W)$				(GHz)
0.01	0.24	0.12	0.06	0.03	35
0.02	0.29	0.14	0.07	0.04	35
0.05	0.52	0.26	0.13	0.07	35
0.1	0.94	0.47	0.23	0.12	35
0.2	1.78	0.89	0.45	0.22	35
0.5	4.26	2.13	1.06	0.53	94
1	8.14	4.07	2.03	1.02	94

In horizontal mode, the time resolution shall be 5 sec or less. Again, fog evolution is rapid as it is the result of subtle interplay between meteorology and surface conditions. Also, the time scale of turbulence is $T = L/v$, where L is the length scale of fog which could be less than 10 m, v is the horizontal velocity scale which approximates 1 - 2 m/s. Therefore $T = 5$ sec typically, and the time resolution should be better than that.

In scanning mode, the radar shall be capable of rapid scanning so that a three dimensional volume can be observed in less than 5 minutes. For certain applications it will be necessary to reconstruct a three-dimensional $Vis-Z$ profile. Due to the rapid variations in the fog layers, it is estimated that the validity/credibility of a three-dimensional Vis profile is rapidly reduced after 5 - 10 minutes.

The radar shall be operational in horizontal mode without adverse effect of ground-reflections on the signal quality caused by side lobes. The modified cloud radar data contain a number of serious data problems, such as horizontal striping etc. They are due to the radar configuration which was not originally optimized for horizontal operations. As significant data volumes are to be collected from the horizontal regions, ground contamination should be avoided as much as possible.

The radar shall be operable in the horizontal mode without adverse effects on human health. This requirement means that a normal radar safety calculation is to be performed on the final design parameters so that the implemented radar can satisfy all health requirements.

6.3. Dual-wavelength technique for La estimates

Normally, in Rayleigh scattering regime we can estimate L_a from LWC based on the linear relationship between them as in Eq. (2.27). The LWC can be retrieved from the differential attenuation between dual radar frequencies. In consideration of the attenuation from fog droplets and gases, the reflectivity measured at frequency f and range R can be given as (Hogan et al., 2005):

$$Z_f = Z_0 - 2\int_0^R (\alpha_f + l_{\alpha_f} \cdot LWC)dR - 10\log_{10}\left[\frac{0.93}{|K_f(T)|^2}\right] \tag{6.3}$$

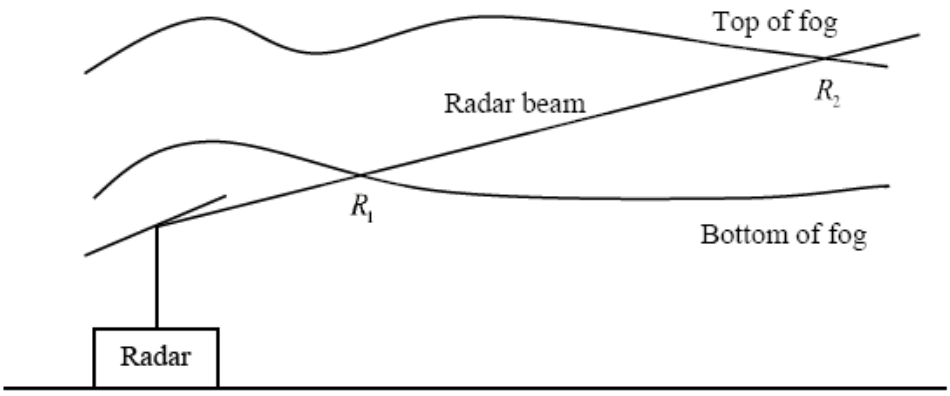

Figure 6.8: The layout of dual-wavelength radar measurements of a fog layer between ranges R_1 and R_2.

where Z_0 is the un-attenuated reflectivity at centimeter wavelengths in dBZ; α_f is the one-way attenuation factor of atmospheric gases (predominantly water vapor) in dB/km; l_{α_f} is the one-way attenuation factor of fog droplets, which is expressed as $l_{\alpha_f} = 0.4343 \cdot 6\pi \cdot \mathrm{Im}(-K)/\lambda$ in $dB/km \cdot (g/m^3)^{-1}$, $K = (m^2-1)/(m^2+2)$, m is the complex refractive index, λ is the radar wavelength in cm. The last term on the right-hand side accounts for the fact that the dielectric factor of liquid water $|K|^2$ decreases with increasing f, and therefore at millimeter wavelengths it is less than its centimeter wavelength value of 0.93. Besides, K is also dependent on temperature T.

Figure 6.8 shows the layout of dual-wavelength radar measurements of a fog layer between ranges R_1 and R_2. R_1 is the range from radar to the bottom of fog layer, R_2 is the range from radar to the top of fog layer. The dual-wavelength ratio (DWR) in logarithmic units is defined as:

$$DWR = Z_{f_1} - Z_{f_2} \tag{6.4}$$

where Z_{f_1}, Z_{f_2} denote the measured reflectivity in dB at frequency f_1, f_2 in the same range. DWR is in dB. Assuming f_2 is higher than f_1, the reflectivity would suffer more attenuation at f_2 than at f_1. Therefore, in practice the measured reflectivity Z_{f_1} is higher than Z_{f_2}, though Z is independent of f by definition.

Given the definition of DWR, DWR_1, DWR_2 denote the dual-wavelength ratio at range R_1, R_2, which are expressed as:

$$DWR_1 = Z_{f_1(R_1)} - Z_{f_2(R_1)} \tag{6.5}$$

$$DWR_2 = Z_{f_1(R_2)} - Z_{f_2(R_2)} \tag{6.6}$$

Substitute Eq. (6.3) into Eq. (6.5), Eq. (6.6) respectively,

$$DWR_1 = 2\int_0^{R_1} \left[(\alpha_{f_2} - \alpha_{f_1}) + (l_{a_{f_2}} - l_{a_{f_1}}) \cdot LWC \right] dR + 10\log_{10}(|K_{f_1}(T_1)|^2 / |K_{f_2}(T_1)|^2) \tag{6.7}$$

$$DWR_2 = 2\int_0^{R_2}\left[(\alpha_{f_2}-\alpha_{f_1})+(l_{a_{f_2}}-l_{a_{f_1}})\cdot LWC\right]dR+10\log_{10}(|K_{f_1}(T_2)|^2/|K_{f_2}(T_2)|^2) \quad (6.8)$$

where T_1, T_2 denote the temperature at range R_1, R_2.

Combine Eq. (6.7) and Eq. (6.8), the differential dual-wavelength ratio ΔDWR can be expressed as:

$$\Delta DWR = 2(R_2-R_1)\cdot\left[(\alpha_{f_2}-\alpha_{f_1})+(l_{a_{f_2}}-l_{a_{f_1}})\cdot LWC\right]+\phi \quad (6.9)$$

where $\Delta DWR = DWR_2 - DWR_1$ is in dB; $\phi = 10\log_{10}\left[|K_{f_1}(T_2)|^2|K_{f_2}(T_1)|^2/|K_{f_1}(T_1)|^2|K_{f_2}(T_2)|^2\right]$ is a small adjustment factor which is dependent of the dual frequencies f_1, f_2 and the two temperature T_1, T_2 at range R_1, R_2.

Therefore, LWC can be deduced from ΔDWR in Eq. (6.9),

$$LWC = \frac{1}{l_{a_{f_2}}-l_{a_{f_1}}}\cdot\left[\frac{\Delta DWR-\phi}{2(R_2-R_1)}-(\alpha_{f_2}-\alpha_{f_1})\right] \quad (6.10)$$

where LWC represents the mean liquid water content in the fog layer between ranges R_1 and R_2. The attenuation factors l_a and α_f are assumed constant over the range of the fog layer. l_a, α_f and the adjustment factor ϕ are all dependent on the frequency f and temperature T.

Based on the linear relationship between L_a and LWC as in Eq. (2.27), the two-way attenuation L_a in dB/km can be deduced from the estimated LWC as:

$$\begin{aligned} L_a &= 2\cdot 0.4343\cdot\frac{6\pi}{\lambda}\mathrm{Im}(-K)\cdot LWC \\ &= 2\cdot 0.4343\cdot\frac{6\pi}{\lambda}\mathrm{Im}(-K)\cdot\frac{1}{l_{a_{f_2}}-l_{a_{f_1}}}\cdot\left[\frac{\Delta DWR-\phi}{2(R_2-R_1)}-(\alpha_{f_2}-\alpha_{f_1})\right] \end{aligned} \quad (6.11)$$

It can be seen from Eq. (6.10) that errors in reflectivity measurements ΔZ_{f_1}, ΔZ_{f_2} may lead to errors in the LWC estimates, which has been discussed in (Hogan et al., 2005). The errors in the LWC would propagate to errors in the L_a, which then propagate to errors in the Vis estimates. An error analysis on Vis estimates is very important for the determination of optimum radar frequency pair for fog measurements. It is also instructive for the design of fog radar with dual-wavelength technique.

6.4. Error analysis on Vis estimates in the Vis-Z-La model

Assuming errors in reflectivity measurements Z_{f_1} and Z_{f_2} to be independent, the error in each dual-wavelength ratio ΔDWR can be estimated by the law of error propagation,

$$\Delta DWR = (\Delta Z_{f_1}^2+\Delta Z_{f_2}^2)^{1/2} \quad (6.12)$$

where ΔZ_{f_1}, ΔZ_{f_2} are the errors in reflectivity measurements at frequency f_1, f_2.

The attenuation factors $l_{a_{f_1}}$, $l_{a_{f_2}}$, α_{f_1}, α_{f_2} and the adjustment factor ϕ in Eq. (6.10) are constant under given dual frequencies f_1, f_2 and given temperatures T_1, T_2. Hence, using Eq. (6.10), errors in LWC estimates resulting from the ΔZ_{f_1} and ΔZ_{f_2} can be retrieved as:

$$\Delta LWC = \frac{(\Delta Z_{f_1}^2+\Delta Z_{f_2}^2)^{1/2}}{\sqrt{2}(l_{a_{f_2}}-l_{a_{f_1}})(R_2-R_1)} \quad (6.13)$$

Table 6.10: The one-way differential attenuation factor Δl_{a_f} for each frequency pair

f(GHz)	35+3	35+10	35+94	35+140	35+220
Δl_{a_f} $(dB/km\cdot(g/m^3)^{-1})$	0.8940	0.8221	3.5258	6.2468	10.5264

Table 6.11: ΔL_{a_f} at the basic frequency f = 35 GHz

f (GHz)	35+3	35+10	35+94	35+140	35+220
ΔL_{a_f} (dB/km)	0.0336	0.0365	0.0085	0.0048	0.0029

Because of the linear relationship between L_a and LWC in Rayleigh scattering regime, errors in L_a at frequency f_1, f_2 are respectively estimated as:

$$\Delta L_{a_{f_1}} = 2\cdot 0.4343\cdot\frac{6\pi}{\lambda_{f_1}}\cdot \mathrm{Im}(-K_{f_1})\cdot\frac{(\Delta Z_{f_1}^2+\Delta Z_{f_2}^2)^{1/2}}{\sqrt{2}(l_{a_{f_2}}-l_{a_{f_1}})(R_2-R_1)} \tag{6.14}$$

$$\Delta L_{a_{f_2}} = 2\cdot 0.4343\cdot\frac{6\pi}{\lambda_{f_2}}\cdot \mathrm{Im}(-K_{f_2})\cdot\frac{(\Delta Z_{f_1}^2+\Delta Z_{f_2}^2)^{1/2}}{\sqrt{2}(l_{a_{f_2}}-l_{a_{f_1}})(R_2-R_1)} \tag{6.15}$$

It can be seen from Eq. (6.14), Eq. (6.15) that the errors ΔL_a depend on the errors in reflectivity measurements ΔZ_{f_1}, ΔZ_{f_2}, the dual frequencies f_1, f_2, and the one-way differential attenuation factor of fog droplets between the dual frequencies.

Considering our Vis estimate model $Vis = C\cdot L_a^a\cdot Z^b$, errors in Vis estimates would come from the errors in Z measurements and L_a retrievals. As Z and L_a have the same variation trend in the fog evolution, the errors in Vis estimates are given by:

$$\begin{aligned}\Delta Vis = {} & C\cdot(L_a-\Delta L_a)^a\cdot(Z-\Delta Z)^b, C\cdot(L_a+\Delta L_a)^a\cdot(Z+\Delta Z)^b{}_{max} \\ & - C\cdot(L_a-\Delta L_a)^a\cdot(Z-\Delta Z)^b, C\cdot(L_a+\Delta L_a)^a\cdot(Z+\Delta Z)^b{}_{min}\end{aligned} \tag{6.16}$$

where ΔZ, ΔL_a are the errors in Z measurements and L_a retrievals.

The errors in Vis estimates will be investigated on the simulated datasets for various fog types and evolutionary stages of fog at f = 3, 10, 35, 94, 140, 220 GHz in a scope of Vis levels (0.01, 0.02, 0.05, 0.1, 0.2, 0.5, 1 km). ΔVis calculated from each frequency pair are compared, and the least ΔVis values correspond to the optimum frequency pair for various fogs.

First we take f = 35 GHz as the basic frequency, and test which of the possible frequency pairs 35 + 3 GHz, 35 + 10 GHz, 35 + 94 GHz, 35 + 140 GHz, 35 +220 GHz can

Table 6.12: The ΔVis of radiation fog for each frequency pair at each Vis level

Vis (km) / f (GHz)	0.01	0.02	0.05	0.1	0.2	0.5	1
35 + 3	0.0002	0.0008	0.0051	0.0218	0.0941	0.7684	70.8258
35 + 10	0.0002	0.0009	0.0056	0.0238	0.1034	0.8981	-
35 + 94	0	0.0001	0.0010	0.0049	0.0217	0.1393	0.6208
35 + 140	0	0	0.0004	0.0025	0.0116	0.0760	0.3281
35 + 220	0.0001	0.0001	0.0001	0.0012	0.0063	0.0434	0.1885

achieve the least ΔVis values for various fogs. Since the one-way attenuation factor l_{a_f} is only dependent on the frequency f, the one-way differential attenuation factor l_{a_f} for each frequency pair can be calculated. The results are listed in Table 6.10.

Assuming $\Delta Z_{f_1} = \Delta Z_{f_2} = 0.05$ dB, $R_2 - R_1 = 3$ km, ΔL_{a_f} at the basic frequency $f = 35$ GHz can be calculated by use of Eq. (6.14) or Eq. (6.15). The results are listed in Table 6.11.

In our Vis estimate model $Vis = C \cdot L_a^a \cdot Z^b$, Vis, Z, L_a can be calculated from the simulated DSD, and a, b, C are estimated based on the least squares method as $a = -1.366$, $b = 0.3695$, $C = 0.1826$. Since ΔZ and ΔL_a are also known, ΔVis can be calculated by use of Eq. (6.16). In this way, ΔVis are calculated on each frequency pair for various fogs in a scope of Vis levels. Taking the radiation fog in our simulated datasets for an example, the Z of radiation fog decreases with increasing Vis, but is independent of f by definition at each Vis level. The L_a of radiation fog also decreases with increasing Vis, but increases with increasing f at each Vis level. The ΔVis of radiation fog for each frequency pair at each Vis level can be calculated. The results are listed in Table 6.12. Moreover, the error bars of each Vis level are plotted for each frequency pair. They are shown in Figure 6.9(a) - (e).

It can be seen from Table 6.12 that for each frequency pair the ΔVis increases with increasing Vis, and the least ΔVis values are achieved by different frequency pairs at various Vis levels. The ΔVis for the frequency pair 35 + 10 GHz at $Vis = 1$ km cannot be estimated because the ΔL_a is beyond the attenuation L_a at the basic frequency $f = 35$ GHz. For the radar design, we have to determine an optimum frequency pair which can achieve relatively small ΔVis values at all the Vis levels. To this end, we have defined a weight function describing the degree of importance of the various Vis levels at highways or airports. The weight function is defined as:

$$W_i(Vis_i) = \exp(-Vis_i) \tag{6.17}$$

where Vis_i denotes the various levels 0.01, 0.02, 0.05, 0.1, 0.2, 0.5, 1 km. It can be seen from Eq. (6.17) that the degree of importance of the various Vis levels decreases with increasing Vis levels. That is, lower Vis levels are given much more concern than higher Vis levels in air and land transportation.

By choosing the least values of the sum of $\Delta Vis \cdot W(Vis)$ over various Vis levels for the 5 frequency pairs, the optimum frequency pair can then be determined. If we take

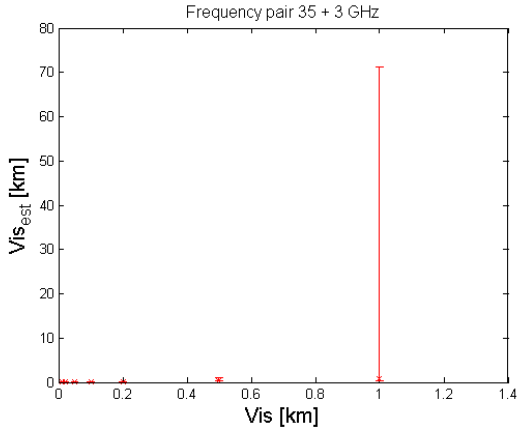
Frequency pair 35 + 3 GHz
Vis_est [km]
Vis [km]
0
10
20
30
40
50
60
70
80
0.2
0.4
0.6
0.8
1
1.2
1.4

(a)

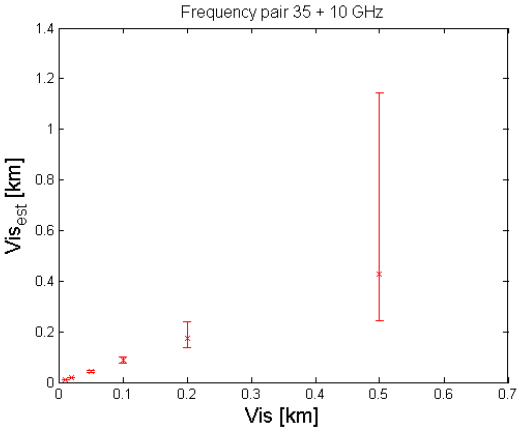
Frequency pair 35 + 10 GHz
Vis_est [km]
Vis [km]
0
0.2
0.4
0.6
0.8
1
1.2
1.4
0.1
0.3
0.5
0.7

(b)

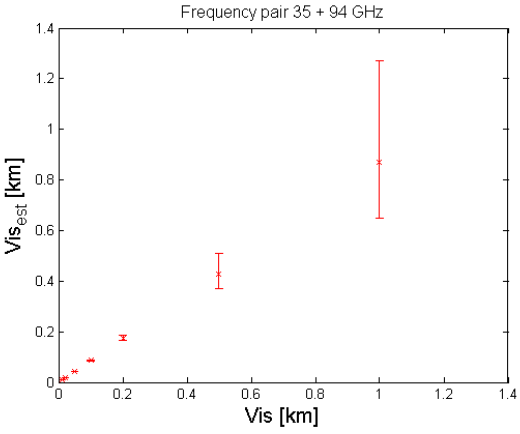
Frequency pair 35 + 94 GHz
Vis_est [km]
Vis [km]
0
0.2
0.4
0.6
0.8
1
1.2
1.4

(c)

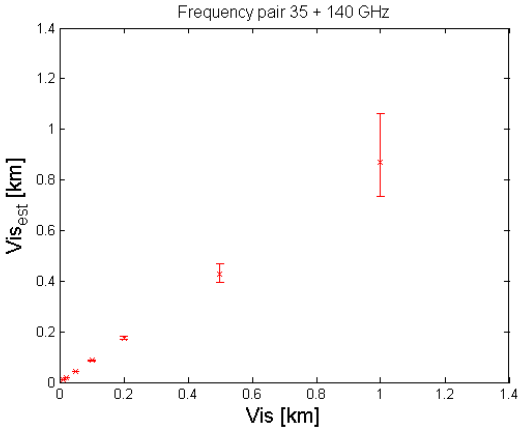

(d)

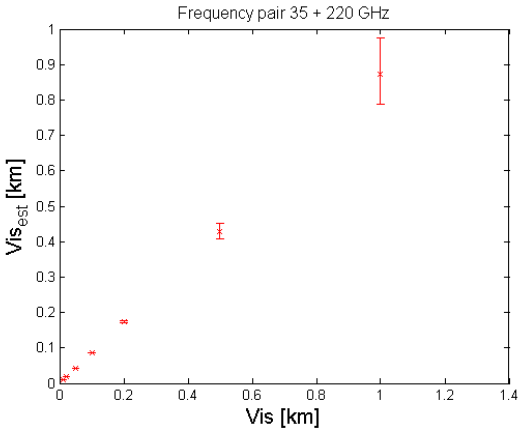

(e)

Figure 6.9: The error bars of each Vis level for each frequency pair 35 + 3 GHz (a), 35 + 10 GHz (b), 35 + 94 GHz (c), 35 + 140 GHz (d), 35 + 220 GHz (e).

into account all the Vis levels, the sum of $\Delta Vis \cdot W(Vis)$ over the Vis levels from 0.01 - 1 km for each frequency pair is calculated, which are listed in Table 6.13.

It can be seen from Table 6.13 that considering all the Vis levels from 0.01 - 1 km, the priority of frequency pairs is 35 + 220 GHz, 35 + 140 GHz, 35 + 94 GHz, 35 + 3 GHz, 35 + 10 GHz. The frequency pair 35 + 220 GHz achieves the least $\Delta Vis \cdot W(Vis)$ value, though it is very close to the second least value achieved by the frequency pair 35 + 140 GHz.

Furthermore, if we only take into account the Vis levels below 0.05 km, the sum of $\Delta Vis \cdot W(Vis)$ over Vis = 0.01 km and Vis = 0.02 km for each frequency pair are listed in Table 6.14.

It can be seen from Table 6.14 that only considering the Vis levels Vis = 0.01 km and

Table 6.13: The sum of $\Delta Vis \cdot W(Vis)$ over the Vis levels from 0.01 - 1 km for each frequency pair

f (GHz)	35+3	35+10	35+94	35+140	35+220
$\Delta Vis \cdot W(Vis)$	0.5686	0.6573	0.1077	0.0582	0.0327

Table 6.14: The sum of $\Delta Vis \cdot W(Vis)$ over Vis = 0.01 km and Vis = 0.02 km for each frequency pair

f (GHz)	35+3	35+10	35+94	35+140	35+220
$\Delta Vis \cdot W(Vis)$	0.0009	0.001	0.0001	0.00006	0.00013

Vis = 0.02 km, the priority of frequency pairs is 35 + 140 GHz, 35 + 94 GHz, 35 + 220 GHz, 35 + 3 GHz, 35 + 10 GHz. The frequency pair 35 + 140 GHz achieves the least $\Delta Vis \cdot W(Vis)$ value, and it is nearly half of the second least value achieved by the frequency pair 35 + 94 GHz.

All above are the error analysis on Vis estimates for the radiation fog in our simulated datasets. So far, we have done similar analysis on the other fog types and evolutionary stages of fog in Table 6.4, and have arrived the same conclusion. Taking into account all the Vis levels from 0.01 - 1 km, the frequency pairs 35 + 220 GHz and 35 + 140 GHz achieve the first and second least $\Delta Vis \cdot W(Vis)$ values, which are very close to each other. If only taking into account the Vis levels below 0.05 km, the frequency pair 35 + 140 GHz achieves the least $\Delta Vis \cdot W(Vis)$ value. Furthermore, it would be more costly and technically more complicated to realize a 220 GHz radar than a 140 GHz radar. Moreover, the antenna beamwidths have to match between the dual frequency radars to minimize errors, which means that a 35 GHz antenna would be about 6 times larger than a 220 GHz antenna. Considering all the items, the frequency pair 35 + 140 GHz is the optimum frequency pair for fog measurements while taking 35 GHz as the basic frequency.

Given the operational parameters of a pulse-Doppler radar and a FMCW radar as listed in Table 6.6 and 6.8, the required minimum transmit power P_t for the optimum frequency pair 35 + 140 GHz can be calculated in order to reach the sensitivity of $Z = -46.3$ dBZ at 3 km distance. As the required minimum P_t increases with increasing Vis levels at a given range resolution, P_t should be determined at the highest Vis level Vis = 1 km for all the 4 range resolution values. Table 6.15 lists the required minimum P_t (W) of the pulse-Doppler radar at Vis = 1 km for the optimum frequency pair 35 + 140 GHz.

It can be seen from Table 6.15 that the required minimum P_t at f = 140 GHz is about three times higher than at f = 35 GHz for each range resolution. For each frequency, the required minimum P_t increases with increasing range resolution.

Similarly, the required minimum P_t (W) of the FMCW radar at Vis = 1 km for the optimum frequency pair 35 + 140 GHz are listed in Table 6.16. We can see that the required

Table 6.15: The required minimum P_t (W) of the pulse-Doppler radar at $Vis = 1$ km for the optimum frequency pair 35 + 140 GHz

ΔR (m) / f (GHz)	12.5	25	50	100
35	8311	2078	520	130
140	24761	6190	1548	387

Table 6.16: The required minimum P_t (W) of the FMCW radar at $Vis = 1$ km for the optimum frequency pair 35 + 140 GHz

ΔR (m) / f (GHz)	12.5	25	50	100
35	8.66	4.33	2.16	1.08
140	25.8	12.9	6.45	3.22

Table 6.17: The one-way differential attenuation factor Δl_{a_f} for each frequency pair

f (GHz)	94+3	94+10	94+35	94+140	94+220
Δl_{a_f} $(dB/km \cdot (g/m^3)^{-1})$	4.4198	4.3479	3.5258	2.7210	7.0006

minimum P_t of the FMCW radar is largely reduced. Therefore, we would use the FMCW radar for fog measurements because of its high performance and drastic cost reduction.

Next we take $f = 94$ GHz as the basic frequency, and test the frequency pairs 94 + 3 GHz, 94 + 10 GHz, 94 + 35 GHz, 94 + 140 GHz, 94 + 220 GHz. The one-way differential attenuation factor Δl_{a_f} for each frequency pair is listed in Table 6.17.

Assuming $\Delta Z_{f_1} = \Delta Z_{f_2} = 0.05$ dB, $R_2 - R_1 = 3$ km, Δl_{a_f} at the basic frequency $f = 94$ GHz can be calculated by use of Eq. (6.14) or Eq. (6.15). The results are listed in Table 6.18.

In our Vis estimate model $Vis = C \cdot L_a^a \cdot Z^b$, the L_a values at the basic frequency $f = 94$ GHz is different from the L_a value at the basic frequency $f = 35$ GHz. Therefore, a, b, C are re-estimated based on the least squares method as $a = -1.366$, $b = 0.3695$, $C = 1.4622$. ΔVis are calculated by use of Eq. (6.16) on each frequency pair for various

Table 6.18: ΔL_{a_f} at the basic frequency f = 94 GHz

f (GHz)	94+3	94+10	94+35	94+140	94+220
ΔL_{a_f} (dB/km)	0.0334	0.0339	0.0419	0.0542	0.0211

Table 6.19: The ΔVis of radiation fog for each frequency pair at each Vis level

Vis (km) / f (GHz)	0.01	0.02	0.05	0.1	0.2	0.5	1
94 + 3	0	0	0.0007	0.0038	0.0170	0.1096	0.4792
94 + 10	0	0	0.0008	0.0038	0.0173	0.1115	0.4881
94 + 35	0	0.0001	0.0010	0.0049	0.0217	0.1393	0.6210
94 + 140	0	0.0002	0.0014	0.0066	0.0286	0.1840	0.8553
94 + 220	0	0	0.0003	0.0021	0.0102	0.0673	0.2905

Table 6.20: The sum of $\Delta Vis \cdot W(Vis)$ over the Vis levels from 0.01 - 1 km for each frequency pair

f (GHz)	94+3	94+10	94+35	94+140	94+220
$\Delta Vis \cdot W(Vis)$	0.2608	0.2656	0.3362	0.4572	0.1583

Table 6.21: The sum of $\Delta Vis \cdot W(Vis)$ over Vis = 0.01 km and Vis = 0.02 km for each frequency pair

f (GHz)	94+3	94+10	94+35	94+140	94+220
$\Delta Vis \cdot W(Vis)$	0.0008	0.0008	0.0011	0.0015	0.0004

fogs in a scope of Vis levels. Again, taking the radiation fog in our simulated datasets for example, the ΔVis for each frequency pair at each Vis level are calculated. The results are listed in Table 6.19. The error bars of each Vis level are plotted for each frequency pair. They are shown in Figure 6.10(a) - (e).

If we take into account all the Vis levels, the sum of $\Delta Vis \cdot W(Vis)$ over the Vis levels from 0.01 - 1 km for each frequency pair is calculated. The results are listed in Table 6.20.

It can be seen from Table 6.20 that considering all the Vis levels from 0.01 - 1 km, the

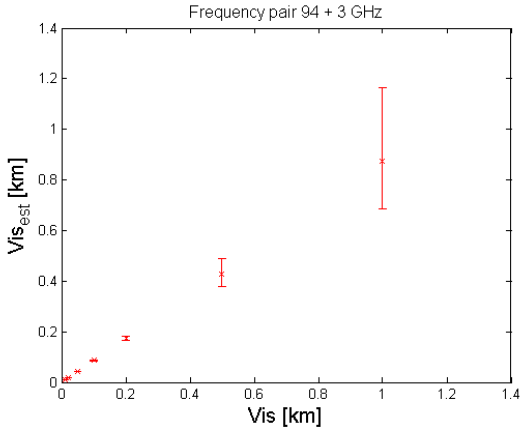
Frequency pair 94 + 3 GHz
Vis$_{est}$ [km]
Vis [km]
0
0.2
0.4
0.6
0.8
1
1.2
1.4

(a)

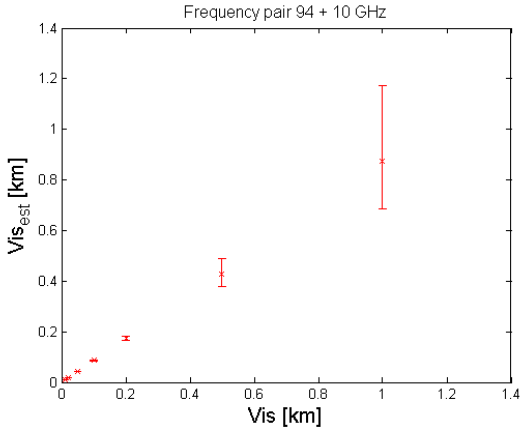
Frequency pair 94 + 10 GHz
Vis$_{est}$ [km]
Vis [km]
0
0.2
0.4
0.6
0.8
1
1.2
1.4

(b)

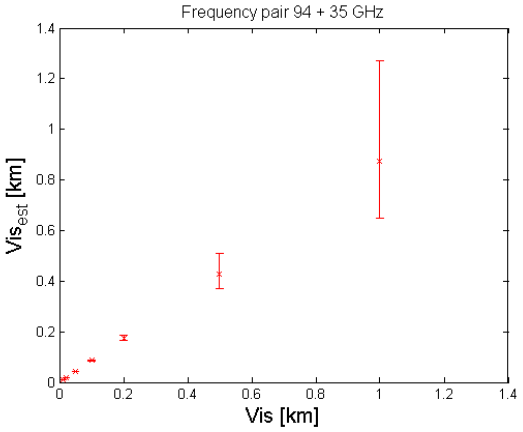
Frequency pair 94 + 35 GHz
Vis$_{est}$ [km]
Vis [km]
0
0.2
0.4
0.6
0.8
1
1.2
1.4

(c)

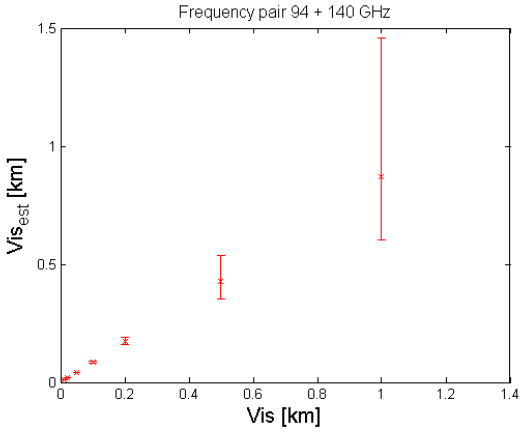

(d)

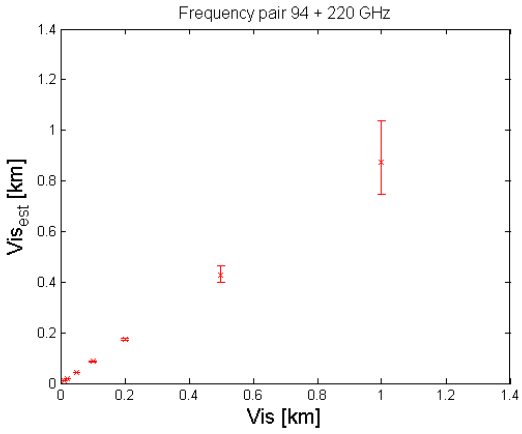

(e)

Figure 6.10: The error bars of each Vis level for each frequency pair 94 + 3 GHz (a), 94 + 10 GHz (b), 94 + 35 GHz (c), 94 + 140 GHz (d), 94 + 220 GHz (e).

priority of frequency pairs is 94 + 220 GHz, 93 + 3 GHz, 94 + 10 GHz, 94 + 35 GHz, 94 + 140 GHz. The frequency pair 94 + 220 GHz achieves the least $\Delta Vis \cdot W(Vis)$ value. Besides, the frequency pairs 93 + 3 GHz and 94 + 10 GHz achieve very close $\Delta Vis \cdot W(Vis)$ value.

Furthermore, if we only take into account the Vis levels below 0.05 km, the sum of $\Delta Vis \cdot W(Vis)$ over $Vis = 0.01$ km and $Vis = 0.02$ km for each frequency pair are listed in Table 6.21.

The priority of frequency pairs stays the same while considering only the Vis levels below 0.05 km. Moreover, we have done similar analysis on the other fog types and evolutionary stages of fog, and have arrived the same conclusion. Therefore, we can conclude that the optimum frequency pair is 94 + 220 GHz for fog measurements while

Table 6.22: The required minimum P_t (W) of the pulse-Doppler radar at Vis = 1 km for the optimum frequency pair 94 + 220 GHz

ΔR (m) / f (GHz)	12.5	25	50	100
94	7812	1953	488	122
220	440995	110249	27562	6891

Table 6.23: The required minimum P_t (W) of the FMCW radar at Vis = 1 km for the optimum frequency pair 94 + 220 GHz

ΔR (m) / f (GHz)	12.5	25	50	100
94	8.14	4.07	2.03	1.02
220	459.37	229.69	114.84	57.42

taking 94 GHz as the basic frequency.

The required minimum transmit power P_t for the frequency pair 94 + 220 GHz can also be calculated in order to reach the sensitivity of $Z = -46.3$ dBZ at 3 km distance. Table 6.22 and 6.23 lists the required minimum P_t (W) of the pulse-Doppler radar and the FMCW radar at Vis = 1 km for the optimum frequency pair 94 + 220 GHz.

It can be seen from Table 6.22 and 6.23 that the required minimum P_t at $f = 94$ GHz is very close to the P_t at $f = 35$ GHz, but the required minimum P_t at $f = 220$ GHz is much larger than the P_t at $f = 140$ GHz. From this point of view, the frequency pair 35 + 140 GHz is much better than 94 + 220 GHz for the use of fog measurements. Furthermore, it would be less costly and less technically complicated to realize low frequency radars than high frequency radars.

6.5. Conclusion

This chapter has investigated the feasibility of designing an advanced fog-visibility radar. On one hand, the fog radar is required to be able to reach a high sensitivity to fog in a relatively long distance. On the other hand, dual-wavelength technique was introduced into the radar system to retrieve L_a from dual-wavelength Z measurements. In this way, Vis can be deduced from the simultaneous Z and L_a measurements based on our Vis estimate model $Vis = C \cdot L_a^a \cdot Z^b$.

The sensitivity of the 35 GHz cloud radar at CESAR was evaluated in fog conditions.

In the sensitivity calculation, the radar can only measure the fog with $Z = -38.4$ dBZ at 3 km distance. The radar sensitivity can be improved by increasing the frequency f, transmit power P_t, and pulse width τ. Using an optimum parameter set with $f = 94$ GHz, $NF = 8$ dB, $L_s = 9$ dB, $P_t = 800$ W, $\tau = 600$ ns, the radar can measure the fog with Z as low as -48 dBZ at 3 km distance with the improved sensitivity.

Based on the simulated DSD datasets for various fog types and evolutionary stages of fog, we calculated Z and L_a at $f = 3$, 10, 35, 94, 140, 220 GHz in a scope of Vis levels (0.01, 0.02, 0.05, 0.1, 0.2, 0.5, 1 km). Among the various fogs, ground fog has the lowest Z values. Therefore, the ground fog has to be considered in priority in order to satisfy the requirements on radar sensitivity. The lowest Z in the ground fog is -46.3 dBZ at $Vis = 1$ km, so the radar is required to be able to measure the ground fog with $Z = -46.3$ dBZ at 3 km distance, which is the assumed maximum detection range of the radar. Besides, the gaseous attenuation from oxygen and water vapor has to be taken into account while determining the operational parameters of the radar. As fog layers are normally thin and highly variable in space, the horizontal resolution of the radar shall be less than or equal to 100 m. Hence, we set 4 range resolution values $\Delta R = 12.5$, 25, 50, 100 m. The operational parameters of a pulse-Doppler radar and a FMCW radar were respectively defined, and the transmit power P_t were calculated at $f = 3$, 10, 35, 94, 140, 220 GHz. The minimum P_t was chosen at an optimum f for each Vis level. However, the optimum frequency f is not unique at various Vis levels. It is difficult to choose a single optimum f for fog measurements due to the highly variable Vis in time and space. Furthermore, there is large difficulty in measuring L_a with a single frequency radar due to the heterogeneity of fog. Therefore, we investigated the feasibility of dual-wavelength radar technology for fog measurements.

Many other meteorological and operational requirements have to be considered for the design of fog radar, such as the operational modes, the spatial and temporal resolution, the adverse effects of ground-reflections on the signal quality caused by the antenna side-lobes, and the radar physical dimensions etc.

Dual-wavelength technique was introduced to provide L_a estimates, where LWC was retrieved from the differential attenuation between the dual frequencies, and L_a can be estimated from LWC based on the linear relationship between them in Rayleigh scattering regime. However, errors in reflectivity measurements may lead to errors in LWC estimates. The errors in LWC propagate to errors in L_a, and then propagate to errors in Vis estimates. Therefore, an error analysis on Vis estimates is very important for the determination of optimum radar frequency pair for fog measurements.

The errors ΔVis in Vis estimates were investigated on the simulated datasets for various fog types and evolutionary stages of fog at $f = 3$, 10, 35, 94, 140, 220 GHz in a scope of Vis levels (0.01, 0.02, 0.05, 0.1, 0.2, 0.5, 1 km). calculated from each frequency pair were compared, and the least ΔVis values correspond to the optimum frequency pair for various fogs. Besides, we defined a weight function $W(Vis) = \exp(-Vis)$ describing the degree of the importance of the various Vis levels in public transportation. First taking $f = 35$ GHz as the basic frequency, frequency pair 35 + 140 GHz achieved almost the least $\Delta Vis \cdot W(Vis)$ value while considering all the Vis levels or only the Vis levels below 0.05 km. Taking $f = 94$ GHz as the basic frequency, frequency pair 94 + 220 GHz achieved the least $\Delta Vis \cdot W(Vis)$ value while considering all the Vis levels or only the Vis levels

below 0.05 km. In general, the frequency pair 35 + 140 GHz is less costly and technically less complicated than 94 + 220 GHz in the radar design. Furthermore, the frequency pair 94 + 220 GHz suffers more attenuation in fog, and it would require more transmit power in order to reach the same sensitivity as 35 + 140 GHz. Based on the error analysis on Vis estimates in the model $Vis = C \cdot L_a^a \cdot Z^b$, we would suggest the frequency pair 35 + 140 GHz as the optimum frequency pair for fog measurements.

7
Conclusions and future work

7.1. Conclusions

In this thesis a series of fog-related issues have been discussed. In general, fog can be regarded as an assemble of small liquid water droplets which are much smaller than those in clouds and rains. This results in very small backscatter and extinction cross sections of fog droplets, increasing the difficulty of fog detection with measuring instruments. The comprehensive elaboration on backscattering and extinction properties of fog formed the basis for looking into the feasibility of detecting fog with radars and optical sensors. The fog measuring instruments were deployed at CESAR in the season November 2011 - March 2012 to observe and record complete fog cycles (formation and dissipation) in the Netherlands. The measurement data, in joint with simulation data in literature, were used to testify our proposed estimate model. In comparison with the Gamma-based $Vis-Z$ model and exponential $Vis-Z$ model, the exponential $Vis-Z-L_a$ model improved the estimated accuracy of Vis. Furthermore, the exponential $Vis-Z-L_a$ model used radar measurements only, i.e. reflectivity (Z) and attenuation (L_a) to deduce visibility (Vis).

Due to the heterogeneity of fog, it is difficult to measure L_a with a single-frequency radar. Therefore, we put forward the use of dual-wavelength technique to retrieve L_a from radar measurements. The dual-wavelength technique was investigated on the simulated datasets for various fog types and evolutionary stages of fog. The error analysis on Vis estimate in the $Vis-Z-L_a$ model was discussed in order to determine the optimum frequency pair for fog measurements. It is instructive for the design of an advanced fog-visibility radar.

We now go through the thesis in detail and highlight the main useful results in each chapter.

- In Chapter 2 we mainly introduced the fog and its characteristics. Fog was divided into different types according to the various weather conditions during the onset of fog. It was noted that stratus-lowering fog is the most frequently occurring type in the Netherlands, which has been observed and documented at CESAR.

  The backscattering and absorption characteristics of fog were investigated over a large range of frequency, temperature and droplet sizes. The simulation results showed that the backscattering is positively correlated with the frequency, temperature and droplet sizes, while the absorption is positively correlated with the frequency and droplet sizes, but is negatively correlated with the temperature. Meanwhile, the frequency and temperature also influence the increase rates of σ_b,

σ_a with increasing frequency. The increase rates of σ_b, σ_a increase with increasing frequency in the lower frequency range $f < 100$ GHz, while in the higher frequency range 100 GHz $< f <$ 1 THz, the increase rate of σ_b still increases with increasing frequency but the increase rate of σ_a turns to decrease with increasing frequency. The increase rate of σ_a is also affected by the temperature. When the temperature is below −20°C, the increase rate of σ_a will decrease with increasing frequency in both frequency ranges.

Radar reflectivity Z, visibility Vis, and attenuation L_a are the key parameters to describe the fog intensity. They were defined and formulated in Rayleigh approximation. Furthermore, the Gamma distribution is often used to represent the fog DSD. Once the DSD is given, Z, Vis and L_a can be calculated from the DSD.

- In chapter 3 we introduced the fog measurement site - CESAR, which is located in the western part of the Netherlands. A comprehensive fog observation campaign was carried out in the season November 2011 - 2012, and a number of in situ and remote sensing instruments were operated for fog measurements. A 35 GHz cloud radar has been used in the so-called "fog mode" for the first time during the campaign. A light-weight aluminum reflector was place above the antenna of the radar, by which the radar beam is mirrored from vertical direction to 3.5° elevation. In this way, the radar beam can sufficiently propagate in the fog and probe the fog in detail.

  The sensitivity of the 35 GHz cloud radar was evaluated in fog conditions. The maximum detection range of the radar was calculated against the corresponding radar reflectivity. The results of sensitivity calculation showed that the radar in the "fog mode" can measure the fog at maximum range R_{max} = 3.353 km with the corresponding reflectivity -37 dBZ. However, the radar sensitivity still needs to be further improved, considering the fact that the fog may have even lower reflectivity.

- In chapter 4 various empirical Vis and Z parameterizations in terms of N, r_m, r_e, LWC or their combinations were summed up. The parameterized Vis, Z were compared with the measured Vis, Z and the DSD-derived Vis, Z based on the dataset of a stratus-lowering fog event at CESAR. It is the only fog case that all the previously described instruments were simultaneously operated for fog measurements. The fairly good agreement between the measured Vis, Z and the DSD-derived Vis, Z indicates that the visibility sensor and the radar were calibrated properly and that the fog droplets are small enough to be considered in Rayleigh scattering region.

  Various $Vis - Z$ and $Vis - Z - N$ relations were derived by combining the various Vis and Z parameterizations. Furthermore, a Gamma-based $Vis - Z$ model was derived based on an assumed Gamma-shaped DSD. An exponential $Vis - Z$ model was deduced by using the regression analysis to the Vis, Z measurement data. All the $Vis - Z$ models were applied to the same previously described dataset. The results showed that the exponential $Vis - Z$ model fits better to the measurement data than the other models for the fog event on February 17-18, 2012.

In the end, we pointed out that the estimated accuracy of Vis can be improved with more microphysical parameters such as N or LWC adding into the exponential $Vis-Z$ model.

- In chapter 5 we put forward a new Vis estimator model $Vis = f(Z, L_a)$ where Vis can be deduced from radar signals only, i.e. reflectivity Z and attenuation L_a. An exponential $Vis-Z-L_a$ model was derived by adding L_a into the exponential $Vis-Z$ model, considering that both Vis and Z can be parameterized in terms of LWC, and LWC is proportional to L_a at a given radar frequency.

  The exponential $Vis-Z-L_a$ model resulted in a higher estimated accuracy of Vis than the Gamma-based $Vis-Z$ model and the exponential $Vis-Z$ model, when tested on a large group of simulated DSD datasets, which were generated from the parameter sets of modified Gamma size distribution of fog droplets for various fog types and evolutionary stages of fog given by Tomasi and Tampieri. The exponential $Vis-Z$ model was also validated with the DSD datasets that were collected by the FSSP at CESAR.

  Furthermore, the exponential $Vis-Z-L_a$ model was validated with the measurement data from the in situ visibility sensors and the cloud radar at CESAR. The DSD-derived Vis was substituted by actual measured Vis, and then the DSD-derived Vis, Z were simultaneously substituted by the measured Vis, Z. As L_a cannot be accurately retrieved from single radar measurements, we can only use DSD-derived L_a in the exponential $Vis-Z-L_a$ model. The results showed that the deviations of the estimated Vis from the measured Vis are much larger than those of the estimated Vis from the DSD-derived Vis. The reason is the spatial variability of the described instruments and the different sampling volumes. In order to reduce the deviations, time-averaging was applied to the original data, and the results showed that the goodness of fit was improved.

- In chapter 6 we investigated the feasibility of designing an advanced fog-visibility radar based on our Vis estimator model. The radar is required to be able to reach a high sensitivity to fog in a relatively long distance. Meanwhile, dual-wavelength technique was introduced to retrieve L_a from dual-wavelength Z measurements.

  The sensitivity of the 35 GHz cloud radar was tried to be improved by increasing frequency f, transmit power P_t, and pulse width τ. On the basis of the simulated DSD datasets for various fog types and evolutionary stages of fog, we calculated Z and L_a at f = 3, 10, 35, 94, 140, 220 GHz in a scope of Vis levels (0.01, 0.02, 0.05, 0.1, 0.2, 0.5, 1 km). Among the various fogs, ground fog has the lowest Z values. Therefore, a series of operational parameters were determined with the ground fog for a pulse-Doppler radar and a FMCW radar. The results showed that implementation of FMCW technology can reduce the transmit power P_t, though the lower P_t of FMCW radar systems may lead to reduced range compared to pulsed radars.

  Dual-wavelength technique was introduced to provide L_a estimates. LWC was first retrieved from the differential attenuation between the dual frequency radars, and then L_a was estimated from LWC based on the linear relationship between them in Rayleigh scattering regime. However, errors in reflectivity measurements

may lead to errors in LWC retrieval, which would propagate to errors in L_a, and then propagate to errors in Vis estimates. An error analysis on Vis estimates is very important for the determination of optimum radar frequency pair for fog measurements.

The errors in Vis estimates were investigated on the simulated datasets for various fog types and evolutionary stages of fog at f = 3, 10, 35, 94, 140, 220 GHz in a scope of Vis levels (0.01, 0.02, 0.05, 0.1, 0.2, 0.5, 1 km). The optimum radar frequency pair would achieve the least ΔVis values. We used 35 GHz, 94 GHz as the basic frequency respectively, and found that the frequency pair 35 + 140 GHz, 94 + 220 GHz achieved the least ΔVis values while considering all the Vis values or only the Vis levels below 0.05 km. Furthermore, the frequency pair 35 + 140 GHz is preferably adopted in the radar design and would suffer less attenuation in fog.

Moreover, other meteorological and operational requirements were put forward, such as the operational modes, the spatial and temporal resolution, the adverse effects of ground-reflections on the signal quality caused by the antenna side-lobes, and the radar physical dimensions etc.

7.2. Recommendations and future work

A more realistic approach is to validate our Vis estimator model $Vis = f(Z, L_a)$ with the measurement data from the in situ visibility sensors and the cloud radar at CESAR. Unfortunately the radar was operated in the "fog mode" for only a couple of days, we do not have as many radar measurements (which were invoked manually) as we have Vis and DSD measurements, which are continuous, automatic measurements. In the future work, we need to acquire more Z measurements to validate our model.

One of the prevailing peculiarities of fog is patchiness, so it is always difficult to estimate L_a from the single-frequency Z measurements. We currently lack reliable L_a measurements in our datasets, which we can only substitute by DSD-derived values. In this thesis we proposed using dual-wavelength technique to estimate L_a. Based on the simulated datasets for various fog types and evolutionary stages of fog, we suggested an optimum radar frequency pair for general fog measurements. This technique should be verified by actual measurements from such a dual-wavelength radar in the future work.

In our Vis estimator model $Vis = f(Z, L_a)$, L_a was indicated as the attenuation from fog droplets, which we calculated from the DSD in this work. Besides, the gaseous attenuation from oxygen and water vapor L_g also exerts influence on Vis and Z, though it is very small compared to L_a. We should consider the impact of L_g on the sensitivity of the model.

Dry and wet aerosols in the air may also contribute to the decrease of Vis and the increase of Z. A SMPS (Scanning Mobility Particle Sizer) instrument was deployed at CESAR to measure dry and wet aerosol spectra in a range of 0.0025 - 1 μm diameter. We can look into the role of aerosols in affecting Vis and Z based on the measurement data.

As mentioned above, the specific fog radar should be capable of operating in horizontal mode and in scanning mode simultaneously that the radar can not only sufficiently penetrate into the fog, but also scan the fog layers in volume.

Throughout our work, our longer term goal is to develop a radar-based fog sensor for

highway and airport applications. This sensor, should be able to provide remote visibility information from radar signals. Remote visibility means the visibility at locations away from our position. This is a huge advantage over current optical visibility sensors, which by definition can only measure visibility on their own location. To measure remote visibility by optical sensors, would be hampered a lot by attenuation of the measurement signals. By contrast, the radar signals can propagate in the fog with less attenuation. Although we did not have the opportunity to build such a radar system, our simulated datasets predict good performance.

Appendix A: Generation of simulated DSD

In section 5.3.2, our Vis estimator model $Vis = f(Z, L_a)$ is validated with a large group of simulated DSD datasets which has covered various fog types and evolutionary stages of fog. The simulated DSD are generated from a series of parameter sets of modified Gamma size distribution of fog droplets for various fogs. In this appendix, we describe the concrete procedures of generating the simulated DSD.

The modified Gamma size distribution has the general form

$$n(r) = ar^{\alpha} \exp\left[-\frac{\alpha}{\gamma}\left(\frac{r}{r_c}\right)^{\gamma}\right], 0 \le r < \infty \tag{A.1}$$

where $n(r)$ is the number concentration of droplets per unit volume per unit radius in μm; a is the number concentration of droplets per unit volume; r_c is the mode radius which indicates the radius of maximum frequency; α, γ and r_c fully determine the shape of the distribution.

Tomasi and Tampieri (1976) has listed the a, α, γ and r_c values for 4 main fog types (radiation fog, evaporation fog, advection fog, and arctic marine advection fog) and 4 evolutionary stages of fog (ground fog, formation stage, mature fog, and dissipation fog). Various fog drop size distributions can produce the same Vis values, hence Vis needs to be divided into a couple of levels. We set 7 Vis levels in previously defined fog conditions, 10, 20, 50, 100, 200, 500, and 1000 m.

Next, we simultaneously use the following three conditions to calculate the profile of the modified Gamma-based DSD for each fog type at the 7 Vis levels.

- The size range of fog droplets is assumed from 0.5 - 49.5 μm in radius with each size bin 1 μm.
- Assuming N is the total number concentration in the whole size range, the real profile of the modified Gamma-shaped DSD is obtained by multiplying $n(r)$ in Eq. (A.1) by N.
- Each Vis is calculated with the use of Vis calculation formulas as in Eq. (2.19) - (2.20).

7 drop size distributions in the assumed range can be obtained for each fog type which correspond to the 7 Vis levels.

Appendix B: Goodness-of-fit statistics

In chapter 5, we compare our Vis estimator model with the other two models in terms of the goodness-of-fit statistics. The goodness-of-fit indicators for parametric modes are:

- The Sum of Squares due to Error (SSE)
- R-Square
- Adjusted R-Square
- Root Mean Squared Error (RMSE)

In this appendix, we give the definitions of these goodness-of-fit statistics.

Sum of Square due to Error

This statistics denotes the total deviation of the estimated values from the measured values.

$$\text{SSE} = \sum_{i=1}^{n} w_i (x_i - \hat{x}_i)^2 \tag{B.1}$$

where w_i is the weight coefficient; x_i denotes the measured values; $\hat{x}_i$ denotes the estimated values.

The closer to 0 the SSE value is, the smaller random error component that the model has, and the better the model will be for estimation.

R-Square

This statistic denotes the degree of the fit in explaining the variation of the data. It is defined as the ratio of the sum of squares of the regression (SSR) and the total sum of squares (SST).

SSR and SST are respectively defined as:

$$\text{SSR} = \sum_{i=1}^{n} w_i (\hat{x}_i - \overline{x})^2 \tag{B.2}$$

$$\text{SST} = \sum_{i=1}^{n} w_i (x_i - \overline{x})^2 \tag{B.3}$$

where $\overline{x}_u$ denotes the mean values. SST is the sum of SSR and SSE.

R-Square is expressed as:

$$\text{R} - \text{Square} = \frac{\text{SSR}}{\text{SST}} = 1 - \frac{\text{SSE}}{\text{SST}} \tag{B.4}$$

The closer to 1 the R-Square value is, the greater proportion of variance is accounted for by the model.

Adjusted R-Square

This statistic is the R-Square adjusted based on the residual degrees of freedom. The residual degrees of freedom is defined as the difference value between the number of measured values m and the number of fitted coefficients n estimated from the measured values.

$$v = m - n \tag{B.5}$$

where v is the residual degrees of freedom.

The adjusted R-Square statistic is expressed as:

$$\text{adjustedR} - \text{Square} = 1 - \frac{\text{SSE(n} - 1)}{\text{SST(v)}} \tag{B.6}$$

The close to 1 the adjusted R-Square value is, the better fit the model takes on. Negative values can occur when the model contains terms that do not contribute to the estimates.

Root Mean Squared Error (RMSE)

This statistic denotes the standard error of the regression. It is an estimate of the standard deviation of the random component in the data.

RMSE is expressed as:

$$\text{RMSE} = \sqrt{\text{MSE}} \tag{B.7}$$

MSE is the mean square error,

$$\text{MSE} = \frac{\text{SSE}}{v} \tag{B.8}$$

Just as with SSE, the closer to 1 the RMSE value is, the better the model will be for estimation.

Appendix C: Commonly used fog drop size distributions

Fog drop size distribution (DSD) is often represented with Gamma or Log-normal distribution. Once the fog DSD is given, the characteristic parameters related to fog can be determined.

Gamma distribution

The general formula for the probability density function of the Gamma distribution is

$$n(r) = \frac{N}{R_n^{\upsilon} \cdot \Gamma(\upsilon)} \cdot r^{\upsilon-1} \cdot e^{-\frac{r}{R_n}}, r \geq 0 \tag{C.1}$$

where n is the number concentration of droplets per unit volume per unit radius in mum; N is the total number concentration per unit volume in cm^{-3}; υ and R_n are the shape and scale parameters of the Gamma distribution; $\Gamma(\upsilon)$ is the Gamma function which has the formula

$$\Gamma(\upsilon) = \int_0^{\infty} t^{\upsilon-1} e^{-t} dt \tag{C.2}$$

The characteristic parameters of fog can be expressed in the forms of R_n and υ,

$$r_m = R_n \cdot \upsilon \tag{C.3}$$

$$r_e = R_n \cdot (\upsilon + 2) \tag{C.4}$$

$$\sigma = (\upsilon \cdot R_n^2)^{1/2} \tag{C.5}$$

$$LWC = \frac{4\pi}{3} \rho_w \cdot N \cdot R_n^3 \cdot (\upsilon + 2)(\upsilon + 1)\upsilon \tag{C.6}$$

$$Vis = \frac{-\ln\epsilon}{2\pi N \cdot R_n^2 \cdot (\upsilon + 1)\upsilon} \tag{C.7}$$

$$Z = 64 \cdot N \cdot R_n^6 \cdot \frac{\Gamma(\upsilon + 6)}{\Gamma(\upsilon)} \tag{C.8}$$

$$Vis \cdot Z = \frac{-64\ln\epsilon}{2\pi} \cdot R_n^4 \cdot \frac{\Gamma(\upsilon + 6)}{\Gamma(\upsilon + 2)} \tag{C.9}$$

Log-normal distribution

The general formula for the probability density function of the Log-normal distribution is

$$n(r) = \frac{N}{\sqrt{2\pi}\sigma_{log} r} \exp\left(\frac{-\ln(r/R_{n,\log})^2}{2\sigma_{log}^2}\right), r \geq 0 \tag{C.10}$$

where $\sigma_{\log}$ is the logarithmic width of the distribution; $R_{n,\log}$ is the median radius.

Just as with the Gamma distribution, the characteristic parameters of fog can be expressed as

$$r_m = R_n \cdot \exp\left(\frac{1}{2}\sigma_{\log}^2\right) \tag{C.11}$$

$$r_e = R_n \cdot \exp\left(\frac{5}{2}\sigma_{\log}^2\right) \tag{C.12}$$

$$\sigma = \left[R_{n,\log}^2 e^{\sigma_{\log}^2}\left(\exp(\sigma_{\log}^2) - 1\right)\right]^{1/2} \tag{C.13}$$

$$LWC = \frac{4\pi}{3}\rho_w \cdot N \cdot R_n^3 \cdot \exp\left(\frac{9}{2}\sigma_{\log}^2\right) \tag{C.14}$$

$$Vis = \frac{-\ln\epsilon}{2\pi N \cdot R_{n,\log}^2 \cdot \exp\left(2\sigma_{\log}^2\right)} \tag{C.15}$$

$$Z = 64 \cdot N \cdot R_{n,\log}^6 \cdot \exp\left(18\sigma_{\log}^2\right) \tag{C.16}$$

$$Vis \cdot Z = \frac{-64\ln\epsilon}{2\pi} \cdot R_n^4 \cdot \exp\left(16\sigma_{\log}^2\right) \tag{C.17}$$

Bibliography

Altshuler, E. E. (1984). A simple expression for estimating attenuation by fog at millimeter wavelengths. *Antennas and Propagation, IEEE Transactions on*, 32(7):757–758.

Amelin, A. G. (1967). *Theory of fog condensation*. Coronet Books Inc.

Anderson, M. G. (2008). *Design of multiple frequency continuous wave radar hardware and micro-Doppler based detection and classification algorithms*. ProQuest.

Atlas, D. (1954). The estimation of cloud parameters by radar. *Journal of Meteorology*, 11(4):309–317.

Atlas, D. and Bartnoff, S. (1953). Cloud visibility, radar reflectivity, and drop-size distribution. *Journal of Meteorology*, 10(2):143–148.

Atlas, D. and Ulbrich, C. W. (1974). The physical basis for attenuation-rainfall relationships and the measurement of rainfall parameters by combined attenuation and radar methods. *J. Rech. Atmos*, 8(1-2):275–298.

Atlas, D. and Ulbrich, C. W. (1977). Path-and area-integrated rainfall measurement by microwave attenuation in the 1-3 cm band. *Journal of Applied Meteorology*, 16(12):1322–1331.

Austin, P. M. (1987). Relation between measured radar reflectivity and surface rainfall. *Monthly Weather Review*, 115(5):1053–1070.

Awan, M. S., Horwath, L. C., Muhammad, S. S., Leitgeb, E., Nadeem, F., and Khan, M. S. (2009). Characterization of fog and snow attenuations for free-space optical propagation. *Journal of communications*, 4(8):533–545.

Babb, D. M., Verlinde, J., and Albrecht, B. A. (1999). Retrieval of cloud microphysical parameters from 94-ghz radar doppler power spectra. *Journal of Atmospheric and Oceanic Technology*, 16(5):489–503.

Baronti, P. and Elzweig, S. (1973). A study of droplet spectra in fogs. *Journal of the Atmospheric Sciences*, 30(5):903–908.

Battan, L. J. (1973). Radar observation of the atmosphere.

Bauer-Pfunstein, M., Peters, G., and Fischer, B. (2013). Empirical z-visibility relation found by fog measurements at an airport by cloud radar and optical fog sensors. In *Proc. 36th AMS Conference on Radar Meteorology*.

Bendix, J. (1995). Ground fog or low level stratus: Decision-making using avhrr data. In *Proc. 1995 Meteorol. Satellite Data Users' Conf*, pages 385–392.

Bendix, J., Thies, B., Cermak, J., and Nauß, T. (2005). Ground fog detection from space based on modis daytime data-a feasibility study. *Weather and Forecasting*, 20(6):989–1005.

Bergot, T. and Guedalia, D. (1994). Numerical forecasting of radiation fog. part i: Numerical model and sensitivity tests. *Monthly Weather Review*, 122(6):1218–1230.

Best, A. (1951). Drop-size distribution in cloud and fog. *Quarterly Journal of the Royal Meteorological Society*, 77(333):418–426.

Bissonnette, L. R. (1992). Imaging through fog and rain. *Optical Engineering*, 31(5):1045–1052.

Boers, R., Baltink, H. K., Hemink, H., Bosveld, F., and Moerman, M. (2013). Ground-based observations and modeling of the visibility and radar reflectivity in a radiation fog layer. *Journal of Atmospheric and Oceanic Technology*, 30(2):288–300.

Bohren, C. F. and Huffman, D. R. (2008). *Absorption and scattering of light by small particles*. John Wiley & Sons.

Bott, A. (1991). On the influence of the physico-chemical properties of aerosols on the life cycle of radiation fogs. *Boundary-Layer Meteorology*, 56(1-2):1–31.

Bott, A., Sievers, U., and Zdunkowski, W. (1990). A radiation fog model with a detailed treatment of the interaction between radiative transfer and fog microphysics. *Journal of the atmospheric sciences*, 47(18):2153–2166.

Bott, A. and Trautmann, T. (2002). Pafog—a new efficient forecast model of radiation fog and low-level stratiform clouds. *Atmospheric Research*, 64(1):191–203.

Brandes, E. A., Zhang, G., and Vivekanandan, J. (2004a). Comparison of polarimetric radar drop size distribution retrieval algorithms. *Journal of Atmospheric and Oceanic Technology*, 21(4):584–598.

Brandes, E. A., Zhang, G., and Vivekanandan, J. (2004b). Drop size distribution retrieval with polarimetric radar: Model and application. *Journal of Applied Meteorology*, 43(3):461–475.

Brenguier, J.-L., Bourrianne, T., Coelho, A. A., Isbert, J., Peytavi, R., Trevarin, D., and Weschler, P. (1998). Improvements of droplet size distribution measurements with the fast-fssp (forward scattering spectrometer probe). *Journal of Atmospheric and Oceanic Technology*, 15(5):1077–1090.

Brown, R. (1980). A numerical study of radiation fog with an explicit formulation of the microphysics. *Quarterly Journal of the Royal Meteorological Society*, 106(450):781–802.

Brown, R. and Roach, W. (1976). The physics of radiation fog: Ii–a numerical study. *Quarterly Journal of the Royal Meteorological Society*, 102(432):335–354.

Burnet, F., Gomes, L., Haeffelin, M., Dupont, J., and Elias, T. (2012). Analysis of the microphysical structures of fog during the parisfog project. In *Proceedings of the 16th international conference of clouds and precipitation (ICCP), Leipzig, Germany*, volume 30, page 582.

Byers, H. R. (1959). General meteorology. In *General meteorology*. McGraw-Hill.

Cermak, J. (2006). *SOFOS-a new satellite-based operational fog observation scheme*. PhD thesis, Universitätsbibliothek Marburg.

Cermak, J. and Bendix, J. (2011). Detecting ground fog from space–a microphysics-based approach. *International Journal of Remote Sensing*, 32(12):3345–3371.

Cermak, J., Schneebeli, M., Nowak, D., Vuilleumier, L., and Bendix, J. (2006). Characterization of low clouds with satellite and ground-based remote sensing systems. *Meteorologische Zeitschrift*, 15(1):65–72.

Cerni, T. A. (1983). Determination of the size and concentration of cloud drops with an fssp. *Journal of climate and applied meteorology*, 22(8):1346–1355.

Chandrasekar, V. and Bringi, V. (1987). Simulation of radar reflectivity and surface measurements of rainfall. *Journal of Atmospheric and Oceanic Technology*, 4(3):464–478.

Chen, C. C. (1975). Attenuation of electromagnetic radiation by haze, fog, clouds, and rain. Technical report, DTIC Document.

Cheng, M. T. and Tsai, Y. I. (2000). Characterization of visibility and atmospheric aerosols in urban, suburban, and remote areas. *Science of the Total Environment*, 263(1):101–114.

Chmielecki, R. M. and Raftery, A. E. (2011). Probabilistic visibility forecasting using bayesian model averaging. *Monthly Weather Review*, 139(5):1626–1636.

Chylek, P. (1978). Extinction and liquid water content of fogs and clouds. *Journal of the Atmospheric Sciences*, 35(2):296–300.

Clark, P. A., Harcourt, S., Macpherson, B., Mathison, C., Cusack, S., and Naylor, M. (2008). Prediction of visibility and aerosol within the operational met office unified model. i: Model formulation and variational assimilation. *Quarterly Journal of the Royal Meteorological Society*, 134(636):1801–1816.

Clark, T. L. (1974). A study in cloud phase parameterization using the gamma distribution. *Journal of the Atmospheric Sciences*, 31(1):142–155.

Clothiaux, E., Miller, M., Albrecht, B., Ackerman, T., Verlinde, J., Babb, D., Peters, R., and Syrett, W. (1995). An evaluation of a 94-ghz radar for remote sensing of cloud properties. *Journal of Atmospheric and Oceanic Technology*, 12(2):201–229.

Collis, R. (1966). Lidar: a new atmospheric probe. *Quarterly Journal of the Royal Meteorological Society*, 92(392):220–230.

Croft, P. J., Pfost, R. L., Medlin, J. M., and Johnson, G. A. (1997). Fog forecasting for the southern region: A conceptual model approach. *Weather and Forecasting*, 12(3):545–556.

Diederen, H., Guicherit, R., and HolLonder, J. (1985). Visibility reduction by air pollution in the netherlands. *Atmospheric Environment (1967)*, 19(2):377–383.

Doviak, R. J. and Zrnic, D. S. (2014). *Doppler Radar & Weather Observations*. Academic press.

Driedonks, A., Van Dop, H., and Kohsiek, W. (1978). Meteorological observations on the 213 m mast at cabauw, in the netherlands. In *4th Symposium on Meteorological Observations and Instrumentation*, volume 1, pages 41–46.

Dupont, J.-C., Haeffelin, M., Protat, A., Bouniol, D., Boyouk, N., and Morille, Y. (2012). Stratus–fog formation and dissipation: a 6-day case study. *Boundary-layer meteorology*, 143(1):207–225.

Duynkerke, P. G. (1991). Radiation fog: A comparison of model simulation with detailed observations. *Monthly Weather Review*, 119(2):324–341.

Duynkerke, P. G. (1999). Turbulence, radiation and fog in dutch stable boundary layers. *Boundary-Layer Meteorology*, 90(3):447–477.

Duynkerke, P. G. and Hignett, P. (1993). Simulation of diurnal variation in a stratocumulus-capped marine boundary layer during fire. *Monthly weather review*, 121(12):3291–3300.

Dye, J. E. and Baumgardner, D. (1984). Evaluation of the forward scattering spectrometer probe. part i: Electronic and optical studies. *Journal of Atmospheric and Oceanic Technology*, 1(4):329–344.

Eccles, P. J. and Mueller, E. A. (1971). X-band attenuation and liquid water content estimation by a dual-wavelength radar. *Journal of Applied Meteorology*, 10(6):1252–1259.

Eisenberg, D. S., Kauzmann, W., et al. (1969). *The structure and properties of water*, volume 123. Clarendon Press Oxford.

Eldridge, R. G. (1957). Measurements of cloud drop-size distributions. *Journal of Meteorology*, 14(1):55–59.

Eldridge, R. G. (1961). A few fog drop-size distributions. *Journal of Meteorology*, 18(5):671–676.

Eldridge, R. G. (1966). Haze and fog aerosol distributions. *Journal of the Atmospheric Sciences*, 23(5):605–613.

Eldridge, R. G. (1971). The relationship between visibility and liquid water content in fog. *Journal of the atmospheric Sciences*, 28(7):1183–1186.

Elias, T., Haeffelin, M., Drobinski, P., Dupont, J.-C., Fesquet, C., Holin, H., Dupont, E., Musson-Genon, L., Bergot, T., and Gomes, L. (2008). The fog life cycle described by the parisfog field experiment. In *Geophysical Research Abstracts*, volume 10.

Elias, T., Haeffelin, M., Drobinski, P., Gomes, L., Rangognio, J., Bergot, T., Chazette, P., Raut, J.-C., and Colomb, M. (2009). Particulate contribution to extinction of visible radiation: pollution, haze, and fog. *Atmospheric Research*, 92(4):443–454.

Ellis, S. M. and Vivekanandan, J. (2010). Water vapor estimates using simultaneous dual-wavelength radar observations. *Radio Science*, 45(5).

Ellis, S. M. and Vivekanandan, J. (2011). Liquid water content estimates using simultaneous s and ka band radar measurements. *Radio Science*, 46(2).

Ellrod, G. P. (2002). Estimation of low cloud base heights at night from satellite infrared and surface temperature data. *National Weather Digest*, 26(1/2):39–44.

Ellrod, G. P. and Gultepe, I. (2007). Inferring low cloud base heights at night for aviation using satellite infrared and surface temperature data. In *Fog and Boundary Layer Clouds: Fog Visibility and Forecasting*, pages 1193–1205. Springer.

Falcone Jr, V. J., Abreu, L. W., and Shettle, E. P. (1979). Atmospheric attenuation of millimeter and submillimeter waves: Models and computer code. Technical report, DTIC Document.

Farina, A. (1992). Antenna-based signal processing techniques for radar systems(book). *Norwood, MA: Artech House, 1992.*

Farnett, E. C. and Stevens, G. H. (1990). Pulse compression radar. *Radar handbook*, 2:10–1.

Findlater, J. (1985). Field investigations of radiation fog formation at outstations. *Meteorological Magazine*, 114(1356):187–201.

Fitzjarrald, D. R. and Lala, G. G. (1989). Hudson valley fog environments. *Journal of Applied Meteorology*, 28(12):1303–1328.

Fox, N. I. and Illingworth, A. J. (1997). The retrieval of stratocumulus cloud properties by ground-based cloud radar. *Journal of Applied Meteorology*, 36(5):485–492.

Frisch, A., Fairall, C., and Snider, J. (1995). Measurement of stratus cloud and drizzle parameters in astex with a kα-band doppler radar and a microwave radiometer. *Journal of the Atmospheric Sciences*, 52(16):2788–2799.

Frisch, A. and Feingold, G. (1998). On cloud radar and microwave radiometer measurements of stratus cloud liquid water profiles. *Journal of Geophysical Research*, 103(D18):23–195.

Frisch, A. S., Martner, B. E., Djalalova, I., and Poellot, M. R. (2000). Comparison of radar/radiometer retrievals of stratus cloud liquid-water content profiles with in situ measurements by aircraft. *Journal of geophysical research*, 105:15.

Garland, J. (1971). Some fog droplet size distributions obtained by an impaction method. *Quarterly Journal of the Royal Meteorological Society*, 97(414):483–494.

Gaussiat, N., Sauvageot, H., and Illingworth, A. J. (2003). Cloud liquid water and ice content retrieval by multiwavelength radar. *Journal of Atmospheric and Oceanic Technology*, 20(9):1264–1275.

Gazzi, M., Georgiadis, T., and Vicentini, V. (2001). Distant contrast measurements through fog and thick haze. *Atmospheric Environment*, 35(30):5143–5149.

Geneva, I. (1995). Attenuation by atmospheric gases in the frequency range 1-350 ghz.

Gerber, H. (1981). Microstructure of a radiation fog. *Journal of the Atmospheric Sciences*, 38(2):454–458.

Gerber, H. (1984). Liquid water content of fogs and hazes from visible light scattering. *Journal of climate and applied meteorology*, 23(8):1247–1252.

Gibbins, C. (1986). Improved algorithms for the determination of specific attenuation at sea level by dry air and water vapor, in the frequency range 1–350 ghz. *Radio science*, 21(6):949–954.

Gosset, M. and Sauvageot, H. (1992). A dual-wavelength radar method for ice-water characterization in mixed-phase clouds. *Journal of Atmospheric and Oceanic Technology*, 9(5):538–547.

Guedalia, D. and Bergot, T. (1994). Numerical forecasting of radiation fog. part ii: A comparison of model simulation with several observed fog events. *Monthly Weather Review*, 122(6):1231–1246.

Gultepe, I. (2008). *Fog and boundary layer clouds: fog visibility and forecasting*. Springer Science & Business Media.

Gultepe, I. and Isaac, G. (2004). Microphysical parameterization for mixed phase clouds using in-situ observations. In *14th International Conference on Clouds and Precipitation (ICCP)*, pages 1326–1329.

Gultepe, I., Isaac, G., Leaitch, W., and Banic, C. (1996). Parameterizations of marine stratus microphysics based on in situ observations: Implications for gcms. *Journal of climate*, 9(2):345–357.

Gultepe, I., Isaac, G., MacPherson, I., Marcotte, D., and Strawbridge, K. (2003). Characteristics of moisture and heat fluxes over leads and polynyas, and their effect on arctic clouds during fire. ace. *Atmos. and Ocean*, 41:15–34.

Gultepe, I., Kuhn, T., Pavolonis, M., Calvert, C., Gurka, J., Heymsfield, A., Liu, P., Zhou, B., Ware, R., Ferrier, B., et al. (2014). Ice fog in arctic during fram-ice fog project: aviation and nowcasting applications, b. am. meteorol. soc., 95, 211–226, doi: 10.1175. Technical report, BAMS-D-11-00071.1.

Gultepe, I. and Milbrandt, J. (2007). Microphysical observations and mesoscale model simulation of a warm fog case during fram project. In *Fog and Boundary Layer Clouds: Fog Visibility and Forecasting*, pages 1161–1178. Springer.

Gultepe, I., Milbrandt, J., and Belair, S. (2006a). Visibility parameterization from microphysical observations for warm fog conditions and its application to canadian mc2 mode. In *AMS meeting, Atlanta, USA, American Meteorological Society*.

Gultepe, I., Müller, M., and Boybeyi, Z. (2006b). A new visibility parameterization for warm-fog applications in numerical weather prediction models. *Journal of applied meteorology and climatology*, 45(11):1469–1480.

Gultepe, I., Pearson, G., Milbrandt, J., Hansen, B., Platnick, S., Taylor, P., Gordon, M., Oakley, J., and Cober, S. (2009). The fog remote sensing and modeling field project. *Bulletin of the American Meteorological Society*, 90(3):341.

Gultepe, I., Tardif, R., Michaelides, S., Cermak, J., Bott, A., Bendix, J., Müller, M., Pagowski, M., Hansen, B., Ellrod, G., et al. (2007). Fog research: A review of past achievements and future perspectives. *Pure and Applied Geophysics*, 164(6-7):1121–1159.

Haeffelin, M., Bergot, T., Elias, T., Tardif, R., Carrer, D., Chazette, P., Colomb, M., Drobinski, P., Dupont, E., Dupont, J., et al. (2010). Parisfog: shedding new light on fog physical processes. *Bulletin of the American Meteorological Society*, 91(6):767–783.

Hamazu, K., Hashiguchi, H., Wakayama, T., Matsuda, T., Doviak, R. J., and Fukao, S. (2003). A 35-ghz scanning doppler radar for fog observations. *Journal of Atmospheric and Oceanic Technology*, 20(7):972–986.

Hammer, E., Gysel, M., Roberts, G., Elias, T., Hofer, J., Hoyle, C., Bukowiecki, N., Dupont, J.-C., Burnet, F., Baltensperger, U., et al. (2014). Size-dependent particle activation properties in fog during the parisfog 2012/13 field campaign. *Atmospheric Chemistry and Physics*, 14(19):10517–10533.

Hansen, B. (2007). A fuzzy logic-based analog forecasting system for ceiling and visibility. *Weather and Forecasting*, 22(6):1319–1330.

Hasted, J. B. (1973). Aqueous dielectrics.

Haywood, J., Bush, M., Abel, S., Claxton, B., Coe, H., Crosier, J., Harrison, M., Macpherson, B., Naylor, M., and Osborne, S. (2008). Prediction of visibility and aerosol within the operational met office unified model. ii: Validation of model performance using observational data. *Quarterly Journal of the Royal Meteorological Society*, 134(636):1817–1832.

Hazen, D. A., Seliga, T., Jacobs, L., and Narvett, P. (2002). Visibility variability at the chicago o'hare airport: Insights into the impacts of runway visual range (rvr) measurements on aviation operations. In *18th Int. Conf. on Interactive Information and Processing Systems (IIPS) for Meteorology, Oceanography, and Hydrology*, pages 13–17.

Heiss, W. H., McGrew, D. L., and Sirmans, D. (1990). Nexrad: next generation weather radar (wsr-88d). *Microwave Journal*, 33(1):79–89.

Hobbs, P. V., Funk, N. T., Weiss Sr, R. R., Locatelli, J. D., and Biswas, K. R. (1985). Evaluation of a 35 ghz radar for cloud physics research. *Journal of Atmospheric and Oceanic Technology*, 2(1):35–48.

Hogan, R. J., Gaussiat, N., and Illingworth, A. J. (2005). Stratocumulus liquid water content from dual-wavelength radar. *Journal of Atmospheric and Oceanic Technology*, 22(8):1207–1218.

Houghton, H. G. and Radford, W. (1938). On the measurement of drop size and liquid water content in fogs and clouds.

Hudson, J. G. (1980). Relationship between fog condensation nuclei and fog microstructure. *Journal of the Atmospheric Sciences*, 37(8):1854–1867.

Hulst, H. C. and Van De Hulst, H. (1957). *Light scattering by small particles*. Courier Corporation.

Hutchison, K. D., Pekker, T., and Smith, S. (2006). Improved retrievals of cloud boundaries from modis for use in air quality modeling. *Atmospheric Environment*, 40(30):5798–5806.

Ingmann, P., Wehr, T., GROUP, E., et al. (2006). Earthcare—a new mission providing global cloud and aerosol profiles. In *Proc. 2005 EUMETSAT Meteorological Satellite Conference. EUMETSAT Publication*, page 46. Citeseer.

Jankiraman, M. (2007). *Design of multi-frequency CW radars*. SciTech Publishing.

Khain, A., Pinsky, M., Magaritz, L., Krasnov, O., and Russchenberg, H. (2008). Combined observational and model investigations of the z-lwc relationship in stratocumulus clouds. *Journal of Applied Meteorology and Climatology*, 47(2):591–606.

Kollias, P., Clothiaux, E., Miller, M., Albrecht, B., Stephens, G., and Ackerman, T. (2007). Millimeter-wavelength radars: new frontier in atmospheric cloud and precipitation research, b. am. meteorol. soc., 88, 1608–1624, doi: 10.1175. Technical report, BAMS-88-10-1608.

Koračin, D., Lewis, J., Thompson, W. T., Dorman, C. E., and Businger, J. A. (2001). Transition of stratus into fog along the california coast: Observations and modeling. *Journal of the atmospheric sciences*, 58(13):1714–1731.

Koschmieder, H. (1925). *Theorie der horizontalen sichtweite: kontrast und sichtweite*. Keim & Nemnich.

Krasnov, O. and Russchenberg, H. (2002). The relation between the radar to lidar ratio and the effective radius of droplets in water clouds: An analysis of statistical models and observed drop size distributions. In *Preprints, 11th Conf. on Cloud Physics, Ogden, Utah, Amer. Meteor. Soc. P*, volume 1.

Kropfli, R., Matrosov, S., Uttal, T., Orr, B., Frisch, A., Clark, K., Bartram, B., Reinking, R., Snider, J., and Martner, B. (1995). Cloud physics studies with 8 mm wavelength radar. *Atmospheric Research*, 35(2):299–313.

Kunkel, B. A. (1971). Fog drop-size distributions measured with a laser hologram camera. *Journal of Applied Meteorology*, 10(3):482–486.

Kunkel, B. A. (1984). Parameterization of droplet terminal velocity and extinction coefficient in fog models. *Journal of Climate and applied meteorology*, 23(1):34–41.

Lala, G. G., Mandel, E., and Jiusto, J. E. (1975). A numerical evaluation of radiation fog variables. *Journal of the Atmospheric Sciences*, 32(4):720–728.

Leipper, D. F. (1995). Fog forecasting objectively in the california coastal area using libs. *Weather and forecasting*, 10(4):741–762.

Lewis, J., Koracin, D., Rabin, R., and Businger, J. (2003). Sea fog off the california coast: Viewed in the context of transient weather systems. *Journal of Geophysical Research: Atmospheres*, 108(D15).

Lewis, J., Koracin, D., and Redmond, K. (2004). Sea fog research in the united kingdom and united states a historical essay including outlook. *Bulletin of the American Meteorological Society*, 85(3):395.

Lhermitte, R. (1987). A 94-ghz doppler radar for cloud observations. *Journal of Atmospheric and Oceanic Technology*, 4(1):36–48.

Li, Y., Hoogeboom, P., and Russchenberg, H. (2014a). Observations and modeling of fog by cloud radar and optical sensors. In *Microwave Conference (EuMC), 2014 44th European*, pages 1824–1827. IEEE.

Li, Y., Hoogeboom, P., and Russchenberg, H. (2014b). Radar observations and modeling of fog at 35 ghz. In *Antennas and Propagation (EuCAP), 2014 8th European Conference on*, pages 1053–1057. IEEE.

Li, Y., Hoogeboom, P., Russchenberg, H. W., and Baltink, H. K. (2015). Retrieval of fog microphysical properties from cloud radar and optical sensors. In *Geoscience and Remote Sensing Symposium (IGARSS), 2015 IEEE International*, pages 4860–4863. IEEE.

Liebe, H. and Hufford, G. (1989). Modeling millimeter wave propagation effects in the atmosphere. *AGARD Report*, 454.

Liebe, H. J. (1985). An updated model for millimeter wave propagation in moist air. *Radio Science*, 20(5):1069–1089.

Liebe, H. J. (1989). Mpm—an atmospheric millimeter-wave propagation model. *International Journal of Infrared and Millimeter Waves*, 10(6):631–650.

Liebe, H. J., Hufford, G. A., and Manabe, T. (1991). A model for the complex permittivity of water at frequencies below 1 thz. *International Journal of Infrared and Millimeter Waves*, 12(7):659–675.

Liebe, H. J., Manabe, T., and Hufford, G. A. (1989). Millimeter-wave attenuation and delay rates due to fog/cloud conditions. *Antennas and Propagation, IEEE Transactions on*, 37(12):1617–1612.

Löhnert, U., Crewell, S., Simmer, C., and Macke, A. (2001). Profiling cloud liquid water by combining active and passive microwave measurements with cloud model statistics. *Journal of Atmospheric and Oceanic Technology*, 18(8):1354–1366.

Maier, F., Bendix, J., and Thies, B. (2012). Simulating z–lwc relations in natural fogs with radiative transfer calculations for future application to a cloud radar profiler. *Pure and applied geophysics*, 169(5-6):793–807.

Maier, F., Bendix, J., and Thies, B. (2013). Development and application of a method for the objective differentiation of fog life cycle phases. *Tellus B*, 65.

Mallow, J. (1975). Empirical fog droplet size distribution functions with finite limits. *Journal of the Atmospheric Sciences*, 32(2):440–442.

Mao, T.-P., Zhou, D.-F., and Niu, Z.-X. (2004). The calculation model of the attenuation due to clouds or fog and the analysis of its characteristic. In *Radio Science Conference, 2004. Proceedings. 2004 Asia-Pacific*, pages 332–334. IEEE.

Martner, B., Kropfli, R., Ash, L., and Snider, J. (1993). Dual-wavelength differential attenuation radar measurements of cloud liquid water content. In *Proc. 26th AMS Conference on Radar Meteorology*.

Mätzler, C. (2002). Matlab functions for mie scattering and absorption, version 2. *IAP Res. Rep*, 8.

Mead, J. B., Mcintosh, R. E., Vandemark, D., and Swift, C. T. (1989). Remote sensing of clouds and fog with a 1.4-mm radar. *Journal of Atmospheric and Oceanic Technology*, 6(6):1090–1097.

Meneghini, R., Kumagai, H., Wang, J. R., Iguchi, T., and Kozu, T. (1997). Microphysical retrievals over stratiform rain using measurements from an airborne dual-wavelength radar-radiometer. *Geoscience and Remote Sensing, IEEE Transactions on*, 35(3):487–506.

Meyer, M. B., Jiusto, J. E., and Lala, G. G. (1980). Measurements of visual range and radiation-fog (haze) microphysics. *Journal of the Atmospheric Sciences*, 37(3):622–629.

Meyer, M. B., Lala, G. G., and Jiusto, J. E. (1986). Fog-82: A cooperative field study of radiation fog. *Bulletin of the American Meteorological Society*, 67(7):825–832.

Meywerk, J., Sievers, O., Quante, M., Venema, V., and Crewell, S. (2002). Deriving water cloud properties from vertical pointing 95 ghz doppler radar. In *Proceedings of ERAD*, volume 161.

Miles, N. L., Verlinde, J., and Clothiaux, E. E. (2000). Cloud droplet size distributions in low-level stratiform clouds. *Journal of the atmospheric sciences*, 57(2):295–311.

Mishchenko, M. I., Travis, L. D., and Lacis, A. A. (2002). *Scattering, absorption, and emission of light by small particles*. Cambridge university press.

Monna, W. and Van der Vliet, J. (1987). *Facilities for research and weather observations on the 213 m tower at Cabauw and at remote locations*. KNMI De Bilt, The Netherlands.

Musson-Genon, L. (1987). Numerical simulation of a fog event with a one-dimensional boundary layer model. *Monthly Weather Review*, 115(2):592–607.

NAKAMURA, K. and INOMATA, H. (1992). Dual-polarization rain observation by x- and ka-band dual-wavelength radar. *Journal of the Meteorological Society of Japan*, 70(6):1085–1096.

Nash, J., Lyth, D., and Oldfield, M. (2005). Observing fog and low clouds with a combination of 78ghz cloud radar and laser ceilometer. In *Proceedings of WMO Instruments and Methods Observation Programme, Technical Conference of Meteorological and Environmental Instruments and Methods of Observation Bucharest, Romania*, pages 4–7.

Nebuloni, R. (2005). Empirical relationships between extinction coefficient and visibility in fog. *Applied optics*, 44(18):3795–3804.

Neiburger, M. and Wurtele, M. (1949). On the nature and size of particles in haze, fog, and stratus of the los angeles region. *Chemical reviews*, 44(2):321–335.

Niu, S., Lu, C., Yu, H., Zhao, L., and Lü, J. (2010). Fog research in china: An overview. *Advances in Atmospheric Sciences*, 27:639–662.

Noone, K. J., Ogren, J. A., Hallberg, A., Heintzenberg, J., STRÖM, J., HANSSON, H.-C., SVENNINGSSON, B., Wiedensohler, A., Fuzzi, S., FACCHINI, M. C., et al. (1992). Changes in aerosol size-and phase distributions due to physical and chemical processes in fog. *Tellus B*, 44(5):489–504.

Nowak, D., Ruffieux, D., Agnew, J. L., and Vuilleumier, L. (2008). Detection of fog and low cloud boundaries with ground-based remote sensing systems. *Journal of Atmospheric and Oceanic Technology*, 25(8):1357–1368.

O'Connor, E. J., Hogan, R. J., and Illingworth, A. J. (2005). Retrieving stratocumulus drizzle parameters using doppler radar and lidar. *Journal of Applied Meteorology*, 44(1):14–27.

Økland, H. and Gotaas, Y. (1995). Modelling and prediction of steam fog. *Contributions to atmospheric physics*, 68(2):121–131.

Oliver, D., Lewellen, W., and Williamson, G. (1978). The interaction between turbulent and radiative transport in the development of fog and low-level stratus. *Journal of the Atmospheric Sciences*, 35(2):301–316.

Pandis, S. N., Seinfeld, J. H., and Pilinis, C. (1990). The smog-fog-smog cycle and acid deposition. *Journal of Geophysical Research: Atmospheres*, 95(D11):18489–18500.

Pasini, A., Pelino, V., and Potestà, S. (2001). A neural network model for visibility nowcasting from surface observations: Results and sensitivity to physical input variables. *Journal of Geophysical Research: Atmospheres*, 106(D14):14951–14959.

Pasini, A. and Potestà, S. (1995). Short-range visibility forecast by means of neural-network modelling: a case-study. *Il Nuovo Cimento C*, 18(5):505–516.

Pasqualucci, F. (1984). Drop size distribution measurements in convective storms with a vertically pointing 35-ghz doppler radar. *Radio Science*, 19(1):177–183.

Pasqualucci, F., Bartram, B., Kropfli, R., and Moninger, W. (1983). A millimeter-wavelength dual-polarization doppler radar for cloud and precipitation studies. *Journal of Climate and Applied Meteorology*, 22(5):758–765.

Paul Herzegh, N. (2006). Development of faa national ceiling and visibility products: Challenges, strategies and progress. In *12th Conference on Aviation Range and Aerospace Meteorology*.

Pazmany, A. L., McIntosh, R. E., Kelly, R. D., and Vali, G. (1994). An airborne 95 ghz dual-polarized radar for cloud studies. *Geoscience and Remote Sensing, IEEE Transactions on*, 32(4):731–739.

Peak, J. E. and Tag, P. M. (1989). An expert system approach for prediction of maritime visibility obscuration. *Monthly Weather Review*, 117(12):2641–2653.

Perez, M. and Zawadski, I. (2003). S-and x-band dual wavelength radars revisited. In *Preprints, 31st Int. Conf. on Radar Meteorology, Seattle, WA, Amer. Meteor. Soc*, pages 51–54.

Petterssen, S. and Petterssen, S. (1956). Weather analysis and forecasting.

Pilié, R., Mack, E., Kocmond, W., Rogers, C., and Eadie, W. (1975). The life cycle of valley fog. part i: Micrometeorological characteristics. *Journal of Applied Meteorology*, 14(3):347–363.

Pilié, R., Mack, E., Rogers, C., Katz, U., and Kocmond, W. (1979). The formation of marine fog and the development of fog-stratus systems along the california coast. *Journal of Applied Meteorology*, 18(10):1275–1286.

Pinnick, R., Jennings, S., Chỳlek, P., and Auvermann, H. (1979). Verification of a linear relation between ir extinction, absorption and liquid water content of fogs. *Journal of the Atmospheric Sciences*, 36(8):1577–1586.

Pinnick, R. G., Hoihjelle, D., Fernandez, G., Stenmark, E., Lindberg, J., Hoidale, G., and Jennings, S. (1978). Vertical structure in atmospheric fog and haze and its effects on visible and infrared extinction. *Journal of the Atmospheric Sciences*, 35(10):2020–2032.

Platt, C. M. R. (1970). Transmission of submillimeter waves through water clouds and fogs. *Journal of the Atmospheric Sciences*, 27(3):421–425.

Probert-Jones, J. (1962). The radar equation in meteorology. *Quarterly Journal of the Royal Meteorological Society*, 88(378):485–495.

Pruppacher, H. R., Klett, J. D., and Wang, P. K. (1998). Microphysics of clouds and precipitation.

Ray, P. S. (1972). Broadband complex refractive indices of ice and water. *Applied Optics*, 11(8):1836–1844.

Recommendation, I. (2009). Attenuation due to clouds and fog. *ITU-R P. 840*, 4.

Reddy, P., Barbarick, D., and Osterburg, R. (1995). Development of a statistical model for forecasting episodes of visibility degradation in the denver metropolitan area. *Journal of Applied Meteorology*, 34(3):616–625.

Richards, M. A. (2005). *Fundamentals of radar signal processing*. Tata McGraw-Hill Education.

Roach, W. (1976). On the effect of radiative exchange on the growth by condensation of a cloud or fog droplet. *Quarterly Journal of the Royal Meteorological Society*, 102(432):361–372.

Roach, W. (1995). Back to basics: Fog: Part 2—the formation and dissipation of land fog*. *Weather*, 50(1):7–11.

Roach, W., Brown, R., Caughey, S., Garland, J., and Readings, C. (1976). The physics of radiation fog: I–a field study. *Quarterly Journal of the Royal Meteorological Society*, 102(432):313–333.

Rohn, M., Vogel, G., Beckmann, B., Röhner, P., Thoma, C., Schneider, W., and Bott, A. (2010). iport-vis: Site specific fog forecasting for munich airport. In *Proceedings of the 5th International Conference on Fog, Fog Collection and Dew, Münster, Germany*, pages 25–30.

Rosenfeld, D., Wolff, D. B., and Atlas, D. (1993). General probability-matched relations between radar reflectivity and rain rate. *Journal of applied meteorology*, 32(1):50–72.

Ruangjun, S. and Exell, R. (2008). Regression models for forecasting fog and poor visibility at donmuang airport in winter. *Asian Journal of Energy and Environment*, 9(3-4):215–230.

Russchenberg, H., Bosveld, F., Swart, D., Ten Brink, H., de Leeuw, G., Brussaard, G., Stricker, H., and Arbesser-Rastburg, B. (2002). Cesar: Cabauw experimental site for atmospheric remote sensing. *Proceedings of the XXVIIth General Assembly of the International Union of Radio Science*, pages 17–24.

Russchenberg, H., Bosveld, F., Swart, D., ten BRINK, H., de LEEUW, G., Uijlenhoet, R., Arbesser-Rastburg, B., van der MAREL, H., LIGTHART, L., Boers, R., et al. (2005). Ground-based atmospheric remote sensing in the netherlands: European outlook. *IEICE Transactions on Communications*, 88(6):2252–2258.

Saunders, P. M. (1964). Sea smoke and steam fog. *Quarterly Journal of the Royal Meteorological Society*, 90(384):156–165.

Sauvageot, H. (1992). *Radar meteorology*. Artech House Publishers.

Sauvageot, H. and Omar, J. (1987). Radar reflectivity of cumulus clouds. *Journal of Atmospheric and Oceanic Technology*, 4(2):264–272.

Schreiner, A. J., Strabala, K. I., Unger, D. A., Menzel, W. P., Ellrod, G. P., and Pellet, J. L. (1993). A comparison of ground and satellite observations of cloud cover. *Bulletin of the American Meteorological Society*, 74(10):1851–1861.

Seinfeld, J. H. and Pandis, S. N. (2012). *Atmospheric chemistry and physics: from air pollution to climate change*. John Wiley & Sons.

Sekelsky, S. M. and McIntosh, R. E. (1996). Cloud observations with a polarimetric 33 ghz and 95 ghz radar. *Meteorology and Atmospheric Physics*, 59(1-2):123–140.

Silverman, B. A., Thompson, B. J., and Ward, J. H. (1964). A laser-fog disdrometer. *Journal of Applied Meteorology*, 3(6):792–801.

Skolnik, M. I. (1962). Introduction to radar. *Radar Handbook*, 2.

Skolnik, M. I. (1970). Radar handbook.

Smith, P. L. (1986). On the sensitivity of weather radars. *Journal of Atmospheric and Oceanic Technology*, 3(4):704–713.

Stephens, G. L., Vane, D. G., Boain, R. J., Mace, G. G., Sassen, K., Wang, Z., Illingworth, A. J., O'Connor, E. J., Rossow, W. B., Durden, S. L., et al. (2002). The cloudsat mission and the a-train: A new dimension of space-based observations of clouds and precipitation. *Bulletin of the American Meteorological Society*, 83(12):1771–1790.

Stewart, D. A. and Essenwanger, O. M. (1982). A survey of fog and related optical propagation characteristics. *Reviews of Geophysics*, 20(3):481–495.

Stolaki, S., Haeffelin, M., Lac, C., Dupont, J.-C., Elias, T., and Masson, V. (2015). Influence of aerosols on the life cycle of a radiation fog event. a numerical and observational study. *Atmospheric Research*, 151:146–161.

Sun, Y., Zhuang, G., Tang, A., Wang, Y., and An, Z. (2006). Chemical characteristics of pm2. 5 and pm10 in haze-fog episodes in beijing. *Environmental science & technology*, 40(10):3148–3155.

Tag, P. M. and Peak, J. E. (1996). Machine learning of maritime fog forecast rules. *Journal of Applied Meteorology*, 35(5):714–724.

Takano, T., Yamaguchi, J., Abe, H., Futaba, K.-I., Yokote, S.-I., Kawamura, Y., Takamura, T., Kumagai, H., Ohno, Y., Nakanishi, Y., et al. (2008). Development and performance of the millimeter-wave cloud profiling radar at 95 ghz. *IEEJ Transactions on Fundamentals and Materials*, 128:257–262.

Tamatsu, Y. and Kumon, H. (2005). Fmcw radar system. US Patent 6,888,494.

Tampieri, F. and Tomasi, C. (1976). Size distribution models of fog and cloud droplets in terms of the modified gamma function. *Tellus*, 28(4):333–347.

Taylor, G. (1917). The formation of fog and mist. *Quarterly Journal of the Royal Meteorological Society*, 43(183):241–268.

Telford, J. W. and Chai, S. K. (1993). Marine fog and its dissipation over warm water. *Journal of the atmospheric sciences*, 50(19):3336–3349.

Telford, J. W., Keck, T. S., and Chai, S. K. (1984). Entrainment at cloud tops and the droplet spectra. *Journal of the Atmospheric Sciences*, 41(21):3170–3179.

Tomasi, C. and Tampieri, F. (1976). Features of the proportionality coefficient in the relationship between visibility and liquid water content in haze and fog. *Atmosphere*, 14(2):61–76.

Toshiaki, T., Yuji, N., and Tamio, T. (2012). High resolution fmcw doppler radar falcon-i for w-band meteorological observations. In *Antenna Technology and Applied Electromagnetics (ANTEM), 2012 15th International Symposium on*, pages 1–4. IEEE.

Turton, J. and Brown, R. (1987). A comparison of a numerical model of radiation fog with detailed observations. *Quarterly Journal of the Royal Meteorological Society*, 113(475):37–54.

Van Ulden, A. and Wieringa, J. (1996). Atmospheric boundary layer research at cabauw. In *Boundary-Layer Meteorology 25th Anniversary Volume, 1970–1995*, pages 39–69. Springer.

Vasseur, H. and Gibbins, C. (1996). Inference of fog characteristics from attenuation measurements at millimeter and optical wavelengths. *Radio Science*, 31(5):1089–1097.

Ventura, J. F. I. (2009). Design of a high resolution x-band doppler polarimetric weather radar. *Universitat Politecnica de Catalunya*.

Vieux, B. E. and Bedient, P. B. (1998). Estimation of rainfall for flood prediction from wsr-88d reflectivity: A case study, 17-18 october 1994*. *Weather and Forecasting*, 13(2):407–415.

Vivekanandan, J., Ellis, S., Oye, R., Zrnic, D., Ryzhkov, A., and Straka, J. (1999a). Cloud microphysics retrieval using s-band dual-polarization radar measurements. *Bulletin of the american meteorological society*, 80(3):381–388.

Vivekanandan, J., Martner, B. E., Politovich, M. K., and Zhang, G. (1999b). Retrieval of atmospheric liquid and ice characteristics using dual-wavelength radar observations. *Geoscience and Remote Sensing, IEEE Transactions on*, 37(5):2325–2334.

Vivekanandan, J., Zhang, G., and Politovich, M. (2001). An assessment of droplet size and liquid water content derived from dual-wavelength radar measurements to the application of aircraft icing detection. *Journal of Atmospheric and Oceanic Technology*, 18(11):1787–1798.

Waldteufel, P. (1973). Attenuation des ondes hyperfrequences par la pluie: une mise au point. In *Annales des Télécommunications*, volume 28, pages 255–272. Springer.

Wantuch, F. (2001). Visibility and fog forecasting based on decision tree method. *Idojárás*, 105:29–38.

Went, F. (1955). Fog, mist, dew, and other sources of water. *USDA yearbook of Agriculture, Washington, DC*, pages 103–109.

Werner, C., Streicher, J., Leike, I., and Münkel, C. (2005). *Visibility and cloud lidar*. Springer.

White, W. and Roberts, P. (1977). On the nature and origins of visibility-reducing aerosols in the los angeles air basin. *Atmospheric Environment (1967)*, 11(9):803–812.

Wilkins, E. et al. (1954). Air pollution and the london fog of december, 1952. *Journal of the Royal Sanitary Institute*, 74(1):1–15.

Willett, H. C. (1928). Fog and haze, their causes, distribution, and forecasting. *Monthly Weather Review*.

Williams, R. C. (2000). Fmcw radar system. US Patent 6,094,158.

Wright, B. and Thomas, N. (1998). An objective visibility analysis and very-short-range forecasting system. *Meteorological Applications*, 5(02):157–181.

Yuskiewicz, B., Orsini, D., Stratmann, F., Wendisch, M., Wiedensohler, A., Heintzenberg, J., Martinsson, B., Frank, G., Wobrock, W., and Schell, D. (1998). Changes in submicrometer particle distributions and light scattering during haze and fog events in a highly polluted environment. *Contributions to atmospheric physics*, 71(1):33–45.

Zdunkowski, W. G. and Barr, A. E. (1972). A radiative-conductive model for the prediction of radiation fog. *Boundary-Layer Meteorology*, 3(2):152–177.

Zdunkowski, W. G. and Nielsen, B. C. (1969). A preliminary prediction analysis of radiation fog. *pure and applied geophysics*, 75(1):278–299.

Zhang, J., Xue, H., Deng, Z., Ma, N., Zhao, C., and Zhang, Q. (2014). A comparison of the parameterization schemes of fog visibility using the in-situ measurements in the north china plain. *Atmospheric Environment*, 92:44–50.

Zhao, Z. and Wu, Z. (2000). Millimeter-wave attenuation due to fog and clouds. *International Journal of Infrared and Millimeter Waves*, 21(10):1607–1615.

Zhou, B. and Du, J. (2010). Fog prediction from a multimodel mesoscale ensemble prediction system. *Weather and Forecasting*, 25(1):303–322.

Zhou, B. and Ferrier, B. S. (2008). Asymptotic analysis of equilibrium in radiation fog. *Journal of Applied Meteorology and Climatology*, 47(6):1704–1722.

List of Publications

Journal Papers

Li, Y., Hoogeboom, P., and Russchenberg, H.W.J.. A novel radar-based visibility estimator. Minor revision by *IEEE Transactions on Geoscience and Remote Sensing*.

Conference Papers

Li, Y., Hoogeboom, P., and Russchenberg, H.W.J.. Radar observations and modeling of fog at 35 GHz. *Proceedings of 8th European Conference on Antennas and Propagation*, The Hague, The Netherlands, April 2014, pp. 1053-1057.

Li, Y., Hoogeboom, P., Russchenberg, H.W.J., and Klein Baltink, H.. Analysis of microphysical processes in fog. *Proceedings of SPIE Remote Sensing*, Amsterdam, The Netherlands, Sept. 2014, 9242.

Li, Y., Hoogeboom, P., and Russchenberg, H.W.J.. Observations and modeling of fog by cloud radar and optical sensors. *Proceedings of 11th European Radar Conference*, Rome, Italy, Oct. 2014, pp. 521-524.

Li, Y., Hoogeboom, P., Russchenberg, H.W.J., and Klein Baltink, H.. Retrieval of fog microphysical properties from cloud radar and optical sensors. *Proceedings of IEEE International Geoscience and Remote Sensing Sumposium (IGARSS)*, Milan, Italy, July. 2015, pp. 4860-4863.

Li, Y., Hoogeboom, P., and Russchenberg, H.W.J.. A novel radar-based visibility estimator. *37th Conference on Radar Meteorology*, Norman, OK, US, Sept. 2015.

Posters

Li, Y., Hoogeboom, P., and Russchenberg, H.W.J.. Modeling of visibility and radar reflectivity in a radiation fog layer in the Netherlands. *URSI Benelux Forum*, Eindhoven, The Netherlands, April 2013.

Li, Y., Hoogeboom, P., and Russchenberg, H.W.J.. Combined modeling and observations of visibility and radar reflectivity in radiation fog. *Cabauw Experimental Site for Atmospheric Research (CESAR) Science Day*, De Bilt, The Netherlands, June 2013.

Li, Y., Hoogeboom, P., and Russchenberg, H.W.J.. Analysis of microphysical processes in fog at Cabauw. *Cabauw Experimental Site for Atmospheric Research (CESAR) Science Day*, De Bilt, The Netherlands, June 2014.

About the Author

Yunlong Li was born in Xingtai, Hebei, China, on 16 September, 1987. He was a bachelor student at the School of Electronic Information and Engineering, Xi'an Jiaotong University between September 2005 and June 2009. From September 2009 to December 2011, he did his Master of Engineering in Information and Communication Engineering at National University of Defense Technology, Changsha. In May 2011, he won a four-year scholarship from the China Scholarship Council and was admitted to Delft University of Technology, The Netherlands, for persuing his PhD degree in the Group of Atmospheric Remote Sensing, Department of Geoscience and Remote Sensing. In April 2012, he started to work as a PhD researcher focusing on the detection, imaging and characterisation of fog fields with radar technology. His interests also include atmospheric remote sensing, remote sensing data processing and analysis, and radar system design and calibration.